NASA/CR—1998-206611

High Temperature Mechanical Characterization of Ceramic Matrix Composites

John Z. Gyekenyesi
Cleveland State University, Cleveland, Ohio

Prepared under Cooperative Agreement NCC3–367

National Aeronautics and
Space Administration

Lewis Research Center

April 1998

Acknowledgments

I would like to thank the NASA Lewis Research Center for use of their facilities and the support provided under the cooperative agreement, NCC3–367, as part of the Advanced High Temperature Engine Materials Technology (HiTemp) Program; Dr. Stanley R. Levine and Dr. Ramakrishna T. Bhatt for their assistance and input in all aspects of the research; and Mr. Gregory Selover, Mr. Stephen Roush, Mr. John Setlock, and Mr. Johnnie Poole for their extra effort in providing promptly needed support. I would like to also express thanks to my committee chairman, Dr. John H. Hemann. His guidance throughout this effort made its completion possible. In addition, thanks to Dr. Stephen Duffy, Dr. Frances Hurwitz, Dr. Paul Bellini, and Dr. Surendra Tewari for their interest in this work and participation on the committee.

Available from

NASA Center for Aerospace Information
7121 Standard Drive
Hanover, MD 21076
Price Code: A13

National Technical Information Service
5287 Port Royal Road
Springfield, VA 22100
Price Code: A13

HIGH TEMPERATURE MECHANICAL CHARACTERIZATION OF CERAMIC MATRIX COMPOSITES

JOHN Z. GYEKENYESI

ABSTRACT

A high temperature mechanical characterization laboratory has been assembled at NASA Lewis Research Center. One contribution of this work is to test ceramic matrix composite specimens in tension in environmental extremes. Two high temperature tensile testing systems were assembled. The systems were assembled based on the performance and experience of other laboratories and meeting projected service conditions for the materials in question. The systems use frames with an electric actuator and a center screw. A PC based data acquisition and analysis system is used to collect and analyze the data. Mechanical extensometers are used to measure specimen strain. Thermocouples, placed near the specimen, are used to measure the specimen gage section temperature. The system for testing in air has a resistance element furnace with molybdenum disilicide elements and pneumatic grips with water cooling attached to hydraulic alignment devices. The system for testing in an inert gas has a graphite resistance element furnace in a chamber with rigidly mounted, water cooled, hydraulically actuated grips.

Unidirectional SiC fiber reinforced reaction bonded Si_3N_4 and triaxially woven, two dimensional, SiC fiber reinforced enhanced SiC composites were

tested in unidirectional tension. Theories for predicting the Young's modulus, modulus near the ultimate strength, first matrix cracking stress, and ultimate strength were applied and evaluated for suitability in predicting the mechanical behavior of SiC/RBSN and enhanced SiC/SiC composites.

The SiC/RBSN composite exhibited pseudo tough behavior (increased area under the stress/strain curve) from 22° to 1550°C. The rule of mixtures provides a good estimate of the Young's modulus of the SiC/RBSN composite using the constituent properties from room temperature to 1400°C for short term static tensile tests in air or nitrogen. The rule of mixtures significantly overestimates the secondary modulus near the ultimate strength. The ACK theory provides the best approximation of the first matrix cracking stress when residual stresses are ignored. The theory of Cao and Thouless, based on Weibull statistics, gave the best prediction for the composite ultimate strength.

The enhanced SiC/SiC composite exhibited nonlinear stress/strain behavior from 24° to 1370°C in air with increased ultimate strain when compared to monolithic SiC. The theory of Yang and Chou with the assumption of a frictional fiber/matrix interface provided the best estimate of the Young's modulus. The theory of Cao and Thouless gave the best estimate for the ultimate strength.

TABLE OF CONTENTS

LIST OF FIGURES

LIST OF TABLES

CHAPTER I

INTRODUCTION

Ceramics in general are extremely brittle, have low strain tolerance, and exhibit a wide variation in ultimate strength. The observed scatter in strength is caused by an abundance of imperfections, i.e., flaws, that are a result of material processing. Over the years the strength and reliability of monolithic ceramics have improved as better processing techniques have evolved. However, as Dev (1992), Taylor (1991), and Moschler (1988) indicate, the brittle failure characteristics of these materials make them acceptable in only a limited range of applications. Even in the limited structural application of monolithic ceramics to turbines in automotive turbochargers, turbo efficiency is sacrificed for structural reliability as noted by Yoshida and Kokji (1989). In an effort to increase ceramic toughness and strength, ceramic matrix

composites with various reinforcements are being developed. These developments are covered briefly by King (1989) and Levine (1992). These composites may include multiple phases or matrices with particulates, whiskers, or continuous fibers.

In the gas turbine industry, ceramic matrix composites (CMCs) are particularly attractive since they have the potential to replace nickel based superalloys in various hot section subcomponents of gas turbines (Dix and Petty (1990) and Constance (1990)). The primary attribute of CMCs relative to nickel based superalloys is the ability of CMCs to be used well beyond current turbine service temperatures, as well as to withstand more severe operating environments. This would enable engines to be operated at higher temperatures with near-stoichiometric combustion without cooling air requirement penalties as noted by Drascovich (1993). Increasing firing temperature is a classic approach for improving turbine efficiency. This subsequently raises turbine inlet temperatures which presents a challenge to design engineers. First stage turbine blades see severe thermal loads. In addition, higher firing temperatures along with conventional air cooling promotes the formation of various nitrogen oxides (NO_x) during combustion. When released at either low altitudes in aeropropulsion applications or in land based power generation applications this pollutant contributes to the formation of smog. When nitrogen oxides are released in the upper atmosphere they deteriorate the earth's protective ozone layer. Maximizing efficiency while

decreasing NO_x emissions requires new combustion chamber designs. These are examples of the complexities involved with improving the thermal efficiency of internal combustion engines.

Another attraction of ceramic composites is their relative low density, which is, as Holmes and Wu (1995) point out, typically 65% to 75% lower than conventional superalloys. One can not overemphasize the fact that weight is a critical design facet for gas turbines utilized in aeropropulsion. Lastly, CMCs offer the potential of increased durability, relative to superalloys, at the high operating temperatures. This would result in increased time between engine overhauls reducing operating costs.

In virtually all ceramic matrix composite systems the goal of the materials scientist is to apply a closing pressure on existing matrix crack surfaces and to impart a tortuous path by crack deflection. This results in an increase in the apparent toughness of the material as noted by Warren (1992). Unlike polymer and metal matrix composites, the fiber/matrix interface in a fiber reinforced ceramic composite must be relatively weak. Optimization of the interface prevents matrix cracks from propagating through the fibers while still providing load transfer. As a result, unbroken fibers bridge a propagating matrix crack and deflect it, which increases the composite work of fracture. In essence, the fiber/matrix interface has to be strong enough to allow load transfer and retain acceptable strength in the transverse direction, but the interface must also allow debonding as a crack passes around the fiber.

There are many ceramic matrix composite systems being investigated and developed, as indicated by Sheppard (1992) and Studt (1991). One of these systems consists of continuous silicon carbide fibers and a reaction bonded silicon nitride matrix (SiC/RBSN). This ceramic matrix composite was developed at the National Aeronautics and Space Administration's (NASA) Lewis Research Center (LeRC) as noted by DiCarlo (1989). There are other ceramic matrix composite systems that are or were being studied and systematically improved at Lewis Research Center. The list includes: polymer derived SiC/SiC systems pioneered by Hurwitz (1990); chemical vapor infiltrated SiC/SiC systems developed by Singh and Levine (1994); sapphire/Al_2O_3 composites developed by Jaskowiak and Setlock (1994); and ceramic composite systems with SiC and Si_3N_4 fibers embedded in either a strontium-aluminosilicate (SAS) matrix or barium-aluminosilicate (BAS) pioneered by Bansal (1992). The work presented in this dissertation is primarily focused on the SiC/RBSN composite system. The SiC/RBSN composite offers properties in the primary direction that are comparable to steel. These include stiffness, first matrix cracking stress as compared to the steel's yield point, and ultimate strength. These properties are retained to a certain degree at high temperatures that go beyond the limits of steel. In addition, an enhanced SiC/SiC composite, produced by chemical vapor infiltration, with a woven fiber architecture will be studied. The enhanced SiC/SiC composite was produced by DuPont Lanxide Composites, Incorporated

for AlliedSignal, Incorporated. AlliedSignal supplied the final specimens to NASA LeRC for testing. The composite has additional proprietary materials added to the SiC matrix as a potential enhancement to its performance at high temperatures in an oxidizing environment.

The path to successful commercialization of the CMC systems mentioned above must include the characterization and evaluation of engineering design properties. As Duffy and Gyekenyesi (1995) point out this requires characterization of mechanical and thermal properties. It is essential to characterize the creep behavior of these materials as well as ascertain how temperature affects their fast fracture. As Sims (1991), Hirano(1992), and Daniel (1989) point out, innovative materials must be tested under conditions that nearly match those expected in service. Motivated by the general lack of high quality test data required by the design engineer, this dissertation presents high-temperature, fast fracture data of the aforementioned SiC/RBSN and enhanced SiC/SiC composites. This data was acquired using a high temperature tensile testing facility assembled by the author at NASA LeRC. The properties of these material systems were obtained in the primary fiber direction, and established for both oxidizing and inert environments.

Flexure testing was the primary testing mode for early composite material development due to the simple requirements of this type of test. Unfortunately, flexure testing has many limitations in generating composite mechanical property data for design purposes. For example, as Wang (1990)

points out, some composites have different strength and stiffness properties in tension than in compression. In addition, the neutral axis shifts towards the compressive side when first matrix cracking is initiated along the tensile surface of the specimen. This limits the usefulness of flexure data in ascertaining the first matrix cracking stress in a brittle matrix composite. Also, flexure tests tend to generate higher strength values than tensile tests. This is due to the fact that only a small portion of the specimen (usually near the tensile surface) is loaded to the maximum stress, making the strength measurements primarily dependent upon defects near the surface. In comparison, tensile testing loads the entire gage volume, making the strength primarily dependent upon the entire volume. The large volume of fully loaded material in a tensile specimen, relative to a flexure specimen, increases the probability of finding a large flaw. Since CMC defects typically include fiber bunching, fiber misalignment, fiber breaks, matrix porosity, matrix cracks and variable interfacial strength, tensile testing is a more appropriate method to characterize a material with these types of volume distributed defects. The uniform stress state through the volume of the tensile specimen evaluates more effectively any nonlinear stress/strain behavior which may develop as the result of cumulative damage processes.

Tensile testing of composites in general can present problems as discussed by Tarnopol'skii and Kincis (1987). The requirement for high temperature, that is over 1000°C (1800°F), tensile testing of ceramic

composites presents a formidable task to today's experimentalist. The challenges include problems in: gripping the specimen; obtaining specimens with consistently uniform geometries; obtaining uniform temperature fields in the gage section; acquiring accurate temperature and strain measurements in a gage section at elevated temperatures as noted by Bashford and Raynal (1990) and Starrett (1990).

The objective of this dissertation is to establish the ability to test ceramic matrix composite coupons at temperatures approaching 1550°C (2800°F) in air and in inert environments. As a contribution to the field of research, this presents new environmental extremes for materials testing relative to current limits with the testing of superalloys. In addition, selected CMC mechanical properties are to be measured for composite systems of interest in aerospace propulsion and power applications. This gave rise to the assembly of a mechanical characterization laboratory at LeRC consisting of two high temperature tensile testing systems. One system was focused on testing in air, and the other system was focused on testing in an inert gas environment. Both systems are capable of reaching temperatures up to 1550°C (2800°C) in the gage section of the tensile specimen. Flat SiC/RBSN and enhanced SiC/SiC composite specimens were tested. The SiC/RBSN composites used in these tests have unidirectional continuous monofilament fiber reinforcement making it difficult to grip the specimen in such a way as to promote failure within the gage section. The fibers in the SiC/RBSN composite

were oriented in the primary direction, which presents an upper bound for strength, stiffness, and work of fracture properties for this composite system. The enhanced SiC/SiC composite has a two dimensional woven fiber tow architecture which does not present as much of a challenge in gripping as does a unidirectionally reinforced composite. Specimen geometry is a major concern due to the low composite in-plane and interlaminar shear strength relative to the tensile strength in the fiber direction as noted by Worthem (1990). In addition, the furnace must provide a uniform temperature within the specimen gage section, while allowing access for strain and temperature measurements. The strain measuring instrument must not influence matrix failure, but has to monitor strain in the composite as the specimen is loaded to its ultimate strength. Also, the temperature measuring device has to measure the specimen gage section temperature with high accuracy without being exceedingly intrusive. Descriptions of the various components of the testing systems are given in the following section. This includes descriptions of various techniques or equipment available that have potential use for high temperature tensile testing of ceramic matrix composites.

The experimental data generated were compared to theoretical predictions for stiffness, proportional limit or first matrix cracking stress, and ultimate strength. King (1989) showed the need to define failure in composites. The data generated here is investigated in light of existing failure theories in Chapter VII. Applicability of these theories for the tested composites are

discussed later in this dissertation. Tripp, et al. (1989) and Pagano and Dharani (1987) provided brief summaries of various failure theories for fast fracture analysis of continuous unidirectional fiber reinforced CMCs under monotonic loads. The devolopment of additional analytical failure theories is taking place in conjunction with the development of the new composites.

For this study unidirectional SiC/RBSN composites were tested from room temperature to 1550°C (2800°F) in air and 1400°C (2550°F) in an inert gas consisting of nitrogen. This work expands the work done previously on the SiC/RBSN composite by Chulya, et al. (1991) at room temperature by testing at temperatures and environments expected in service. The enhanced SiC/SiC composites were tested from room temperature to 1370°C (2500°F) in air. The experimental data were compared with theoretical predictions for stiffness, proportional limit or first matrix cracking stress, and ultimate strength. As a contribution to the field of research, the work here gives a thorough analysis of the mechanical properties at high temperatures of the SiC/RBSN composite system. Also, stiffness and ultimate strength properties for the triaxially woven fiber reinforced SiC/SiC composite is given a thorough analysis.

CHAPTER II

EQUIPMENT

2.1 Tensile Testing Components and Performance Criteria

Challenges associated with elevated temperature tensile testing of ceramic matrix composites are noted in the introduction. To address some of these challenges, Gyekenyesi and Hemann (1987, 1988), and later Gyekenyesi and Bartolotta (1992), evaluated various systems with potential applications as components of an elevated temperature tensile testing system. These efforts included literature searches, personal communications with other researchers, and follow-up evaluations of sub-components that are available commercially. To reiterate, one of the objectives, as a contribution to the field of research, of

this research is to expand materials testing to greater environmental extremes. As a result of the literature search, the following researchers were identified (along with their affiliation) as being very active in the development of high temperature (+1000°C) tensile testing: (This list is not intended to be all-inclusive.)

- Starrett (1990) - Southern Research Institute,
- Wiederhorn, et al. (1988) - National Institute of Standards and Technology,
- Mandell and Grande (1991), Grande (1987) - MIT,
- Lewis III (1992) - Naval Research Laboratory,
- Hartman, Zawada, and Russ (1988) - Wright/Patterson Air Force Base,
- Holmes (1992) - The University of Michigan,
- Lui and Brinkman (1985), Jenkins (1995), Caputo, et al. (1987), Huddleston (1986) - Oak Ridge National Laboratories
- and Worthem (1994) - NASA Lewis Research Center.

In addition, as Quinn (1992) points out, the American Society for Testing and Materials (ASTM) technical committee C-28 (Advanced Ceramics) is playing an active role in developing standard test methods for ceramic composites. The data presented in this dissertation was acquired in a manner conforming to ASTM protocols set forth in published standards or proposed standards where applicable.

Based on the literature search, discussions with other researchers, and discussions with vendors, an exhaustive evaluation of methods and equipment preceded the assembly of several high-temperature testing rigs at LeRC. Methodologies and sub-components that were evaluated included:

- grip fixtures,
- specimen geometries,
- high temperature furnaces and cooling systems,
- strain measuring techniques (extensometry),
- temperature acquisition methods.

The sections that follow describe how the above mentioned sub-components are utilized in a high-temperature testing system. In addition, their respective advantages and disadvantages are presented. Finally, sections 2.2 to 2.4 describe the two testing systems that were assembled from the acquired sub-components. The first system was assembled in order to test ceramic matrix composite specimens at high temperatures in air. A second system was assembled at the same location in order to test the ceramic matrix composite coupons at high temperatures in an inert environment. Another system was assembled to test ceramic fibers at high temperatures in air. The fiber testing system is covered briefly in the last section of this chapter.

2.1.1 Gripping Fixtures

Different types of gripping techniques were evaluated including pin grips, face loading grips, and shoulder support grips. Gripping unidirectional fiber reinforced ceramic composite specimens in a high-temperature environment presents many challenges. In general, these specimens are weak in shear relative to their longitudinal strength. This tends to limit the type of grip utilized. In addition, it is desirable to have the grips at the same temperature as the specimen gage section in order to prevent stresses due to thermal gradients. Unfortunately, at temperatures over 1000°C (1800°F), hot grips suffer from chemical reactions between the specimen material and the grip face material, as well as oxidation of the grips when an inert environment is not utilized. In addition, hot grips are usually fabricated from materials that are costly and difficult to machine, such as silicon carbide, making the initial acquisition of the grips expensive and replacement parts difficult to obtain. Based on these observations it was concluded that the most practical fixture would be cooled grips located outside of the furnace hot zone. Cooling the grips allows the use of conventional metal grips fabricated from steel or stainless steel components. As Jenkins (1995) points out, isolating the grips from the harsh environment surrounding the specimen gage section permits the experimentalist to perform many tests with a single set of grips. Grip alignment is also more consistent from test to test with cooled grips, since the

grip temperature is maintained at a constant level at or near the ambient temperature.

a. Pin Grips

Pin type grips hold the specimen using one or more shear pins placed through holes machined in the specimen. As noted earlier the unidirectional fiber reinforced SiC/RBSN composite is weak in shear relative to its longitudinal tensile strength. This increases the probability of the pins shearing out of the specimen during load application. Therefore, it was concluded during the evaluation phase that this type of grip fixture is better suited for ceramic composites with cross-ply or woven fiber architectures. In order to maintain specimen alignment the holes in the specimen require very precise machining. Unlike metals, ceramics are unforgiving when it comes to any misalignment in the load train of the tensile testing system. If the drilled hole is not perpendicular to the specimen surface, or the inner diameter does not match the pin diameter, then a significant stress concentration is produced that leads to localized failure of the specimen in the grip area. Furthermore, the experimentalist must take extreme care in precisely positioning the holes in the specimen. The applied load, which is transmitted through the pin to the specimen, must be distributed as evenly as possible around the pins in order to avoid producing high contact stress regions. This requires accuracy in aligning

the holes, and maintaining concentricity of the holes, both of which are difficult to achieve in ceramic matrix composite specimens. This is a direct result of the relative hardness of the ceramic matrix material and the variation in hardness encountered in ceramic composites, since different constituents (i.e., matrix and fibers) are present in the machined specimen.

b. Face Loading Grips

Serrated grips have been utilized in high temperature tensile testing of silicon carbide fiber reinforced lithium aluminosilicate (SiC/LAS) by Grande (1987) with mixed results. In Grande's work the serrated grips were applied directly to the surface of the specimen, and the specimens tended to fail under the grips by shredding. This led to the use of serrated grips with tabs on the specimen. The tabs would be adhesively bonded to the specimen, which is common practice in testing polymer matrix composites at room temperature. However, a high temperature adhesive and tab would have to be used for elevated temperature tests anticipated in this study, and cooling of the grip area would still be required.

A serrated grip and tab system transfers the load to the specimen over a large surface area relative to either pin type grips or the shoulder support technique discussed in the next section. This reduces the chance of failure within the grip section. An optimized normal force is required to prevent the

tabs (usually some type of laminated material) from shearing off the specimen without crushing the coupon. Commercially available fixtures of this type will apply the normal force by pneumatic, hydraulic, or mechanical means. The mechanical application uses wedge grips, and this type of grip runs the risk of crushing the specimen.

Friction grips with smooth or slightly rough surfaces are also utilized. A SiC or alumina insert is employed here. The grips apply a high normal force relying on the frictional force to transmit load to the specimen. This gripping technique has been used for high temperature tensile testing by Mah, et al. (1985). As with the serrated grips, the force can be applied by pneumatic, hydraulic, or mechanical means. It is important to have the specimen faces flat and parallel, with tight tolerances, so that the applied load from the grip faces is distributed evenly over the gripped area of the specimen.

In tests conducted at the Massachusetts Institute of Technology by Grande (1987), a single pin was used in conjunction with the friction grips (i.e., a hybrid grip fixture). The pin was used for initially aligning the specimen. During tests the pin would carry a small portion of the total load.

c. Shoulder Support Grips

Shoulder support grips transmit load at the radius of an hourglass shaped specimen. This type of grip has been used successfully with high

temperature tensile creep testing and static tensile tests by Holmes and Cho (1992). The specimen requires very high precision machining. Unfortunately, this type of specimen geometry adds significant cost and "turn-around" time to each specimen. In addition, specimen design is critical, since this type of grip can easily generate shear failures.

2.1.2. Heating Techniques

Many techniques are available for heating the gage section of a tensile specimen up to at least 1500°C (2700°F). An important consideration is the need for access to the specimen gage section for strain and temperature measuring instrumentation. Also, it is important to minimize the overall length of the specimen to reduce the cost of each specimen. Specimen cost can be significant for ceramic matrix composites. A gage section of at least 25 mm (1 in.) long, with a homogeneous temperature distribution, is needed for adequate representation of material properties (e.g., strength, stiffness, etc.). The furnace must operate without interruption for reasonable durations in an inert or oxidizing atmosphere. Available heating techniques include resistance element furnaces, radiant furnaces, electrical heating, radio frequency induction heating, and laser heating.

a. Resistance Element Furnace

Resistance element furnaces are highly reliable. They consist of electrical resistance elements supported by refractory molding. The heating elements can be located next to the specimen, in the same atmosphere as the specimen gage section, or a susceptor may be used in an induction type system where the heating elements are isolated from the specimen environment. In the induction system the elements heat a susceptor, which in turn heats the specimen. This type of furnace can be configured with one or more heating zones, depending on available space. Multiple heating zones allow for better control of the temperature distribution within the specimen gage section. Different materials are used for elements depending on the required operating temperatures and environments. Huddleston (1986) correctly points out that platinum alloys are used for temperatures up to 1800°C (3300°F), for either an inert or oxidizing atmosphere. Some ceramic materials such as silicon carbide are used for heating elements to reach temperatures over 2000°C (3600°F). But Sumner (1985) indicated that ceramic heating elements can only be used in an oxidizing atmosphere. The oxygen is needed to form a protective coating of silica on the surface of the elements. Otherwise, the silicon carbide will break down by dissociation. Huddleston (1986) also indicated that molybdenum disilicide can be used to reach temperatures of 1750°C (3180°F) in air, and this material can also attain temperatures up to 1550°C (2730°F) in argon.

Tungsten elements are used to attain a temperature of 2550°C (4620°F) in a vacuum or an inert gas. Graphite can also be used at temperatures over 2500°C (4500°F), but only in an inert atmosphere.

Relatively quick changes in gage section temperatures can be obtained with molybdenum disilicide elements and platinum alloy elements. As noted above, these elements can operate to at least 1550°C (2730°F) in an oxidizing atmosphere. The same can be said for tungsten and graphite elements, but only in an inert gas environment. The silicon carbide elements do not offer the ability to quickly change gage section temperatures in comparison to the molybdenum disilicide, platinum, tungsten, and graphite heating elements.

b. Direct Electrical Heating

Direct electrical heating would have large amounts of electrical current passing through the specimen. Obviously, the specimen has to be electrically conductive for this type of heating to be viable. One advantage to direct electrical heating is that the specimen is completely unobstructed. Unfortunately, this type of heating produces significant axial thermal gradients, which are very difficult to control. Usually, the constituents in a composite material have different electrical properties. Also, many ceramics are not highly conductive. Therefore, direct electrical heating can not be

recommended for heating composite specimens since nonuniform heating of the specimen may occur as explained by Jenkins (1995).

c. Radiant Furnaces

Radiant furnaces use high intensity lamps placed around the specimen gage section. Lamps are usually mounted with cooled reflectors to focus the energy on the specimen. As a result, individual heating zones are created which allow greater control of the thermal distribution along the length of a specimen. Heating efficiency is dependent on the emissivity of the specimen surface. Higher temperatures can be attained with specimens that have surface emissivities approaching that of a black body. Oxide ceramics have good absorptivity making radiant heating a viable technique. On the other hand, silicon carbide and silicon nitride are more reflective making it more difficult to achieve the desired test temperature. Radiant furnaces also offer relatively quick response in comparison to resistance element furnaces. This is a distinct advantage when thermal cycling the test specimen.

d. Laser Heating

For this type of heating technique a powerful carbon dioxide laser is typically used to heat the specimen gage section. The CO_2 laser operates in the

infrared region of the electromagnetic wave spectrum with a wavelength of 10.6 microns. Efficiency of the laser heating technique is highly dependent upon the infrared absorption properties of the specimen. Highly reflective or transparent surfaces lower the efficiency of this heating technique considerably. The laser can be configured to heat opposite sides of a specimen using a beam splitter and mirrors. Unfortunately, this heating technique produces a significant thermal gradient within the specimen gage section. Oxide ceramics such as alumina have the surface properties needed for heating by a CO_2 laser. For example, Sayir (1991) has used a CO_2 laser to melt approximately 0.51 mm (0.020 in.) diameter polycrystalline oxide ceramic rods to produce $Al_2O_3/Y_3Al_5O_{12}$ eutectic fibers. A limited number of high temperature tensile tests were performed on fibers at Lewis Research Center using a CO_2 laser. Tensile tests with sapphire fibers have been used with limited success. In contrast, large diameter (140 μm) carbon coated CVD type silicon carbide fibers were found to be too reflective for efficient heating for over 1000°C (1800°F).

e. Radio Frequency Induction Heating

Radio frequency induction heating is a simple technique that heats an object with electromagnetic radiation. An electrically conductive specimen is heated directly or a susceptor may be used with an electrically nonconductive

specimen. The indirect heating system uses liquid cooled induction coils with relatively few turns wrapped around the specimen or susceptor. This technique allows a relatively unobstructed view of a specimen that is conductive, but thermal gradients are difficult to control within the specimen. Worthem (1994) used this heating technique with a silicon carbide susceptor. This approach yields a quick response which makes it practical for thermal cycling. However, accurate control is difficult and power supply is somewhat bulky.

2.1.3. Strain Measuring Techniques

Various techniques are available for measuring strain in a tensile specimen. These include contact gages, non-contact optical strain measuring devices, and indirect techniques. The need to record strain in test specimens that are exposed to 1550°C (2800°F) in inert and oxidizing gases limits the choice of strain measuring devices. Reactions between materials, oxidation, turbulence in the surrounding gas, and changing specimen surface conditions are typical of the potential problems which have to be addressed if a strain measuring device will provide reliable data at high temperature. In addition, ceramic matrix composites release a significant amount of energy when matrix cracking occurs. This makes it difficult for a gage to continue measuring strain from the first matrix cracking stress to the ultimate strength of the material. The fracture strain of ceramic based materials is considerably less than the

fracture strain of metals. Therefore, an instrument with high resolution is necesary.

a. Crosshead Displacement

The simplest form of strain measurement entails recording the crosshead displacement of the tensile testing machine. This is an indirect technique for determining the strain in a specimen. Accuracy is extremely limited since included with the crosshead displacement is the compliance of everything in the load train. The load train typically consists of grips, alignment devices, load cell, and possibly tabs on the specimen. Because of the interactions of the load train components, this technique cannot account for non-homogeneous strain in a specimen. Consequently, strain calculated from the crosshead displacement is not recommended for applications where high precision is required. For this reason this technique of acquiring strain data was not used.

b. Bonded Resistance Strain Gage

Bonded resistance type strain gages are widely used and offer low cost. This type of gage works well at room temperature. However difficulties arise at the testing temperatures, i.e., 1550°C (2800°F), required for this project.

Elevated temperatures degrade the bond between the gage and the specimen as well as causing problems with the attachment of electrical leads. In addition, thermal compensation is a problem. There are efforts by Gregory, et al. (1997), Castelli and Lei (1994), and many others to develop resistance strain gages for temperatures over 800°C (1470°F), but this maximum use temperature is still well below the operating temperatures proposed for this project.

c. Clip-On Extensometers

Clip-on extensometers are limited to near ambient temperature testing. The limit is approximately 200°C (390°F). The gages are held to the specimen using rubber bands for room temperature tests or springs for ambient or higher temperatures. Gyekenyesi and Bartolotta (1992) evaluated a number of strain measuring devices, including clip-on gages, for testing of ceramic matrix composites. Results from the clip-on gages were comparable to the results from the bonded resistance strain gages. A significant advantage of clip-on gages over bonded resistance gages is the ability to be quickly mounted to the specimen. A disadvantage is the high initial cost relative to the cost of bonded resistance strain gages.

d. Optical Strain Gages

Different types of optical strain measuring devices are available commercially. Most use flags mounted to the specimen. A laser or high intensity light is used to illuminate the flags. The shadow from the flags is used to measure the strain in the specimen. Starrett's (1986) optical strain analyzer at Southern Research Institute is an example of a system using high intensity lights. The system used by Gyekenyesi and Bartolotta (1992) utilizes a laser to illuminate the flags. Difficulties include mounting the flags to the specimen, and keeping the flags attached to the specimen after matrix cracking has occurred. At high temperatures the material of the flags may react with the specimen which could induce significant stress concentration at the point of attachment. In addition, gas turbulence around the specimen causes changes in the atmospheric density which varies the index of refraction. Gyekenyesi and Bartolotta (1992) demonstrated that this phenomena introduces noise during the acquisition of strain data, making it difficult to observe the first matrix cracking strain. Sealing all openings in the furnace with woven insulation tends to reduce the turbulence, but does not eliminate it altogether.

Other types of optical strain measuring devices track the speckle patterns produced at the surface of the specimen under laser light illumination. The speckles are produced by the constructive and destructive

interference of the reflected laser light off the microscopically rough surface of the specimen. One technique presented by Hercher, et al. (1987) tracks groups of speckles at two points. The strain is determined by the change in distance between the two points using real time output. Other speckle techniques use a single laser illuminated point. The strain is determined from the change in the speckle pattern at the single point. A system using this technique was described by Sayir, et al. (1994). Unfortunately, this technique does not produce real time output, and the range of gage lengths from approximately 0.1 mm (4 mils) as described by Sayir, et al. (1994) to 1 mm (40 mils) as covered by Gyekenyesi and Hemann (1987) is significantly less than the desired 25 mm (1 inch). Both types of speckle techniques are sensitive to out of plane motions and changing specimen surface conditions, which lead to loss of tracking. It should be noted, Tuma, et al. (1997) presented a system, based on the technique described by Sayir, et al. (1994), that can measure strain in real time. It is being developed for future high temperature applications.

There are other optical strain measuring methods available such as Moire fringe techniques and holography. Neither of these systems measure strain in a real time mode. Moire techniques require grating on the specimen surface, the attachment of which is difficult to maintain at high temperatures. Holographic methods are well suited for out of plane motions. However, holographic techniques are extremely sensitive to external vibrations, making

the isolation of this type of system paramount. This is not practical for an entire tensile testing system.

Finally, the laser interferometric strain gage (also referred to as the Sharpe method) has been used for measuring crack mouth opening displacements by Jenkins (1987), and measuring localized strain by Martin and Schultz (1983). The gage length for this type of system is limited to a range of 100 to 800 μm (4 to 32 mils), which is well below the targeted gage length of 25 mm (1 inch). The system uses a single laser to illuminate two fiducial marks placed either directly on the specimen surface, or onto platinum tabs mounted to the specimen. These fiducial marks reflect the laser at an angle in two directions. The reflected laser from each indentation interferes at fixed increments. The fixed increments are dependent upon the laser light frequency, angle of the reflected beams, and the distance between the fiducial marks. Interference fringes are produced from the reflected laser light. These interference fringes move as the distance between the fiducial marks changes. Counting fringes as they move across a fixed sensor allows the experimentalist to establish a relationship between the strain in the specimen and the fiducial marks.

e. Mechanical Extensometers

High temperature mechanical extensometers usually consist of a pair of quartz or silicon carbide rods that contact a specimen with a transducer mounted at the other end of the rods. The transducer is either a variable capacitor, or bonded resistance strain gages. The body of the extensometer can be gas or liquid cooled. Early attempts by researchers such as Grande (1987) tried to utilize mechanical extensometers that contacted the specimen at small divots machined into the surface of the specimen. This prevented the extensometer rods from slipping. However, these extensometers tend to exert a significant transverse load on the specimen. Unless this transverse load is counteracted by another extensometer, or by other means, significant bending moment is introduced into the specimen. More recently, mechanical extensometers have been developed that minimize the contact force, and reduce the bending induced into tensile specimens. These devices have rods with knife edges that minimize slipping at the surface of the specimen. In addition, oxidation products tend to fuse the rods to the surface of the specimen, which is beneficial since it reduces slipping of the rods.

2.1.4. Temperature Measuring Methods

In order to obtain accurate material behavior data, temperature measurements must be precise and rigidly controlled. Usually, a digital temperature control unit is used to manage the temperatures during a test. Temperature measurements are typically made with thermocouples or optical pyrometers.

Optical pyrometers use the energy radiated from a specimen surface to determine the surface temperature. The energy output at a fixed wavelength is dependent on the emissivity, wavelength, and temperature. Unfortunately, the emissivity changes as the specimen surface conditions change, sometimes making it difficult to acquire accurate temperature readings. Ng, et al. (1997), have presented the development of a multiwavelength pyrometer which shows promise as a viable temperature measuring device for ceramics at high temperatures.

Currently thermocouples are the preferred instrument for measuring the specimen gage section temperature. As noted by Jenkins (1995) this is especially true for long duration testing such as creep tests. Platinum-rhodium thermocouples are available to measure temperatures that are well beyond 1550°C (2820°F). This type of thermocouple should be located near the specimen surface, without coming in direct contact with the specimen.

Typically, platinum based thermocouples are not chemically compatible with the silicon based ceramic materials.

2.2 Common Equipment For the Inert Gas and Air Testing Systems

Various techniques for gripping and heating the specimen and measuring the strain and temperature of the specimen gage section were presented in the preceding sections. Optimum systems were chosen based on the need to generate reliable high temperature tensile data from flat ceramic matrix composite coupons, economically, and in a timely manner. This resulted in two separate tensile testing systems that were assembled for this work. The systems are described in this section, section 2.3 and in section 2.4. One system allowed testing specimens in air up to a temperature of 1550°C (2820°F). The other system allowed testing specimens up to 1700°C (3100°F) in an inert environment. Room temperature tests were conducted in the frame with the air furnace. Both systems used the same type of universal tensile testing frames, extensometers, and specimen geometries. A single desktop personal computer (PC) was employed for data acquisition/analysis for both systems. In addition, a single chiller system was used to supply the cooling water for both systems. This section describes the equipment that was either common to both systems or shared by both systems. Subsequent sections describe the components which are unique to each system.

2.2.1 Frame

All tests were conducted on universal tensile testing machines. Both machines have 100 kN (22 kip) electric actuators with center screws that have a displacement range of 100 mm (4 in.). Both are digitally controlled, allowing closed-loop control with load, strain, or crosshead displacement. Displacement resolution is 0.05 μm (2 μin.) for both frames.

A 50 kN (11 kip) load cell was used with each frame. The linearity of this load cell is within ±0.25% of the actual load from 0.4% of full capacity to full capacity. The load cell's full scale analog signal output was set at 10 volts. This output was used as input for the computerized data acquisition system.

2.2.2 Mechanical Extensometer, Capacitive

A comparison of various commercially available strain measuring devices with real-time output was made by Gyekenyesi and Bartolotta (1992). This study included two types of low contact force mechanical extensometers, and an optical strain measuring device with a scanning laser using flags mounted to the specimen surface. Based on this study a decision was made to utilize a low contact force mechanical extensometer, which offered the

optimum performance for the current application. This device is a capacitive mechanical extensometer which employs a variable capacitor to convert displacements into electrical signals. Low contact forces minimize the bending in test specimens. Each extensometer is configured for high temperature applications. The silicon carbide rods with knife edges are gas cooled along with the bodies of the extensometers. The devices are mounted on rails so that the extensometers can be easily removed from the working area while the specimen is being mounted in the grips. Horizontal micrometers, attached to the bodies of the extensometers, are used to bring the extensometer rods into contact with the specimen surface. The micrometer allows the user to apply a minimal contact load to the test specimen. A removable stop and micrometer are located at the end of each extensometer. These components are used to establish the original gage length of the test specimen, and maintain this length until the extensometer is brought into contact with the specimen surface. All the extensometers have mechanical calibrators which were positioned in front of each extensometer during the calibration process. Figures 1 and 2 depict the extensometers mounted in a typical testing system. The manufacturer's specifications are presented in Table I.

Table I: Capacitive Mechanical Extensometer Specifications.

Gage Length: 25 mm (0.98 in.)
Gage Length Accuracy: ±0.05 mm (±0.002 in.)
Gage Length Repeatability: ±0.01 mm (±0.0004 in.)
Strain Range: 0.04 mm/mm (0.04 in./in.)
Displacement Range: ±1.0 mm (±0.04 in.)
Output Sensitivity: 40 V/mm (1000 V/in.)
Temperature Range, Specimen: Ambient to 1600°C
(Ambient to 2900°F)
Contact Force: 0 to 0.98 N (0 to 3.5 ounces)
Rods: Silicon carbide, knife edge

2.2.3 Recorders and Computerized Data Acquisition and Analysis

During the early phases of the testing program load and strain outputs were recorded with an analog two-pen X-Y recorder. Load signals from the frame were processed through an optical isolator during high temperature tests in order to minimize signal noise.

A computerized data acquisition/analysis system was later obtained for improved consistency and accuracy. This system was used for the majority of the tests. The software was custom written to specifications established by the requirements.

At the time the high temperature tensile testing laboratory was being assembled there were no commercially available software packages for data acquisition and analysis of tensile data that presented adequate flexibility for research. There were many systems available for basic data acquisition but not

for in-depth materials tensile test data analysis with significant user input. Existing systems offered few if any advantages over the manual analyses of analog outputs.

The computerized data acquisition and analysis system acquired for the laboratory monitors the analog signals from a load cell, up to two longitudinally mounted strain gages, a transversely mounted strain gage, and a laser extensometer. The laser extensometer is monitored through the serial port of the computer and the rest of the signals are collected through a plug-in card with analog to digital signal converters.

The software allows user interaction to identify different points on a stress/strain curve. The deviation from linearity or some other event along the stress/strain curve was manually identified by the operator. This is an important feature due to the fact that many materials, composites in particular, behave differently enough to make the initiation of the deviation from linearity difficult to identify in a consistent manner. In addition, the system has the capability to determine a "yield point" according to user defined conditions. The ultimate strength of the material is identified automatically. Young's modulus was determined by manually identifying the two end points of the linear regime of the stress/strain curve with the computer doing linear interpolation between these points. Information on the secant and tangent modulus using operator defined points are available also. The work of fracture, defined as the area under the stress/strain curve, is

determined by numerical integration between two user defined points. All the points are selected directly on the stress/strain curve using a cursor that scrolls along the plotted curve. The stress and strain values corresponding to the cursor position are displayed concurrently. The point identification takes place with the computer being in a graphics mode as opposed to being in a text mode.

The analysis system is capable of determining average and bending strains at any stress level when two longitudinally mounted strain gages placed on opposite sides of the specimen are utilized. The material Poisson's ratio can be determined when a transversely mounted strain gage is used in conjunction with one of the longitudinally mounted strain gages. At the present time all the above features are incorporated into a readily available commercial software package.

2.2.4 Laboratory Chiller System

Jenkins (1995) found that minor temperature fluctuations in the cooling water that circulates to the grips can have a significant effect on the temperature distribution in a tensile specimen. Consequently, a closed loop laboratory chiller system with a water cooled condenser was used to supply the cooling water for the grips in both high temperature tensile testing systems. In addition, the system was used to cool the furnace jacket in the inert gas tensile

testing system. The chiller is capable of supplying cooling water that is within ±1°C (±2°F) of the set point. The unit has a 56.8 liter (15 gal.) reservoir. The domestic water supply was used to cool the condenser.

2.2.5 Laboratory Environment

The building in which the laboratory is located has a computer controlled heating, ventilation, and air conditioning (HVAC) system. The air flow and temperature are controlled in the individual laboratories. The humidity is not controlled. Exhaust ducts are set near the equipment and in a hood on a bench. A centralized duct supplied the air in the room. The laboratory doors were kept closed and there are no windows.

2.3 System For Testing In Air

The components mentioned in the preceding sections were common to both test rigs. However, there are components unique to each system which allow for testing specimens in different environments. The following subsections provide a description of the system used for testing in air:

2.3.1 Grips

Compact water cooled stainless steel pneumatically actuated wedge grips are utilized for both ambient and high temperature testing. Each grip is attached to a hydraulic alignment device. The hydraulic alignment device is identical to the unit used by Caputo, et al. (1987), as well as Jablonski and Bhatt (1990). The pneumatic grips with the attached alignment device are depicted in Figure 1. The grips have serrated grip faces with a 1.6 mm tooth spacing (16 teeth/in.) embedded in a diamond pattern. The actuator piston is directly linked to the wedges which results in small longitudinal displacement of the grip faces upon clamping of the grips. This produces a light uniaxial compressive preload on the specimen during initial clamping. The maximum

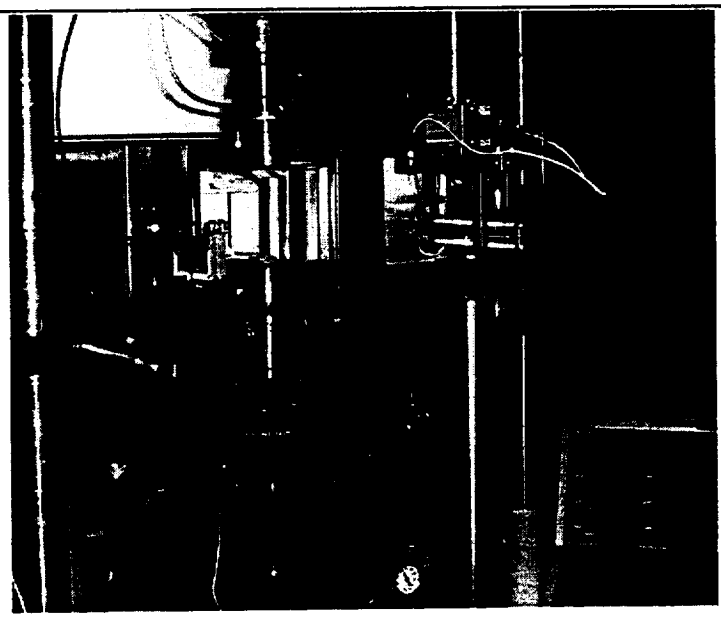

Figure 1. High temperature tensile testing system for testing specimens up to 1550°C in air.

longitudinal displacement is restrained by the limited range of specimen thicknesses that the grips can accommodate. As a result, the compressive preload has not caused compressive failures in any of the specimens tested. A pressure regulator is mounted in the pneumatic supply line to regulate the force with which the grips clamp down on the specimen. The loading technique is described in the section on the testing procedures. The grip housing contains water passages in order to cool the grips. Thermocouples are located at the bases of the grip faces within each grip in order to monitor the temperatures at the ends of the specimen.

2.3.2 Furnace

The furnace used for the high temperature tests in air has a slotted configuration. This design allows the furnace to remain hot throughout the testing procedure, including the time during which the specimens are replaced in the fixtures. The furnace is mounted on rails so that it can be drawn around the test coupon once the specimen has been mounted in the grips. Figure 1 depicts the furnace in a mounted position. An insulating plug is inserted in the slot of the furnace prior to testing the specimen. The insulating plug has two holes which provide access for the extensometers. The hot section of the furnace is relatively short, i.e., 100 mm (4 in.) long. In addition, the hot section has two heating zones with molybdenum disilicide elements. There are six

U-shaped elements per heating zone mounted around the specimen axis. Each zone has the elements wired in series and controlled by a digital controller. The controllers are configured so that one controller governs the temperature in the entire furnace. According to the manufacturer's specification the maximum temperature attainable with this system is approximately 1550°C (2800°F), which can be held at ±2°C within a 25 mm (1 in.) gage section. Thermocouples are used to monitor element and specimen temperatures.

2.3.3 Bonded Resistance Strain Gages

Commercial resistance strain gages were employed for all room temperature tensile tests of the SiC/RBSN composites. These were general purpose strain gages with a constantan resistance grid backed by a 0.03 mm (0.001 in.) thick, tough, flexible polyimide film. The constantan is a metal alloy consisting of 45% nickel and 55% copper. All the gages had 120 ohm resistance. The gage sections were 6.4 mm (0.25 in.) in length. Table II presents the

Table II: Bonded Resistance Strain Gage Specifications.

Foil Alloy: constantan
Self-Temperature Compensation: 5 μstrain/°C (3 μstrain/°F)
Gage Section: 6.4 mm (0.250 in.)
Resistance: 120.0 ±0.15% Ω @ 24°C (75°F)
Gage Factor: 2.035 ±0.5% @ 24°C (75°F)
Transverse Sensitivity: +0.9 ±0.2 %
Strain Limits: 5% (Approximate)

manufacturer's specifications for the bonded strain gages. A methyl-cyanoacrylate based adhesive with a trichloroethane catalyst was used to bond the strain gages to the surface of the specimen.

2.3.4 Clip-On Extensometers

Clip-on extensometers were used for the room temperature tests on the SiC/SiC composites. The clip-on gages were acquired after the room temperature tests on the SiC/RBSN composites were completed. The gages work in conjunction with the frame's electronic controls. A built-in resistor is used to make them self-identifying to the frame's controls. As a result, the frame's controls are used to electronically calibrate the gages and process their signal. The gages have a fixed gage length of 12.7 mm (0.5 in.) with 12.7 mm (0.5 in.) extenders for a total gage length of 25.4 mm (1.0 in.). The maximum extension of these gages is ±1.27 mm (±0.05 in.). This results in a maximum strain of 5.000%. Specifications are presented in Table III. Rubber bands were

Table III: Clip-On Extensometer Specifications.

Gage Length: 25.4 mm (1.0 in.) with extender
Range: ±1.27 mm (±0.05 in.)
Output Sensitivity: 2.5 mV/V +1% -3%
Temperature Range: -70 to 200°C (-100 to 390°F)
Bridge Resistance: 350 Ω nominal
Excitation: 5 V nominal

used to hold the gages to the specimen.

2.4 System For Testing In Inert Gas

The inert tensile testing system is comprised of an environment chamber which encloses the furnace, grips, and specimen. A smaller chamber is utilized to house the extensometer, and this ancillary chamber is attached to the side of the main chamber.

The cooling system for the extensometer is a closed loop system which directs the inert gas from the environment chamber through the extensometer cooling ports. This system has a small pump that circulates the gas through coiled copper tubing mounted outside of the chamber. Electrically operated

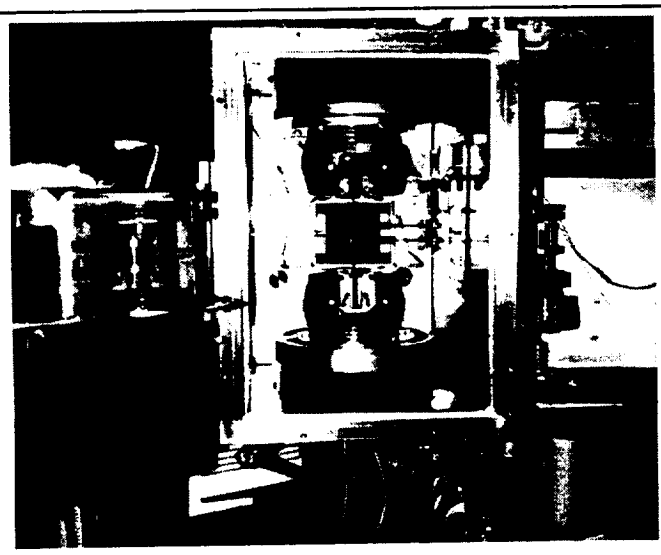

Figure 2. High temperature tensile testing system for testing specimens up to 1700°C in nitrogen or argon.

valves are mounted in the copper lines to isolate the pump from the chamber during any system purging operation. The following sections provide a description of the unique components used in the system for testing in an inert environment:

2.4.1 Grips

Water cooled, hydraulically actuated wedge grips were used for the high temperature tests in the inert environment. These grips are mounted to a rigid load train with a permanent alignment device. The alignment device has angularity and concentricity adjusters to eliminate/minimize inherent load train misalignments. The grip faces are serrated in a diamond pattern with a 1.6 mm serrated tooth spacing (16 teeth/in). An actuator operates the grip housing and allows the grip faces to remain stationary along the specimen axis. This minimizes longitudinal preloading of the specimen. The grip housing contains passages for water cooling, and thermocouples are fastened to the grips near the grip faces.

2.4.2 Furnace

The furnace used for the high temperature tests in an inert gas consists of two clam shells mounted rigidly in the chamber. One shell is mounted to the back of the chamber while the other half is mounted to the door which is the front of the chamber. The heating unit utilizes resistance graphite elements mounted in water cooled jackets. Porous carbon surrounds the elements for insulation. The furnace mounted in the test system is depicted in Figure 2. The hot section is 64 mm (2.5 in.) long. Each clam shell contains one element making this a single zone furnace. A single digital controller is used to control furnace operation. Maximum specimen temperature is approximately 1700°C (3100°F). The maximum specimen temperature is held to ±2°C within a 25 mm (1.0 in.) gage section, as specified by the manufacturer. Thermocouples are used to monitor element and specimen temperatures.

2.4.3 Chamber and Accessories

The main chamber houses the furnace, grips, and specimen as mentioned above. Bellows are used to seal the grips to the chamber. The ancillary chamber, which is attached to the side of the main chamber, houses the extensometer and the calibrator. The load cell is mounted outside of the chamber. The vacuum pump is a dual stage rotary vane pump that evacuates

the chamber during the purging process. Both argon and nitrogen gas cylinders are connected to the system, and this allows for testing in either atmosphere. A gas purifier is used to insure that oxygen content is at a negligible level. The tests are conducted at a pressure that is slightly greater than atmospheric pressure.

2.5 High Temperature Fiber Tensile Testing System

A separate tensile testing system was utilized to generate high temperature tensile data for the fibers. This is the same system used by Sayir, et al. (1994) for the testing of $Al_2O_3/Y_3Al_5O_{12}$ (YAG) eutectic fibers. In this work a 10 kN (2.2 kip) capacity universal screw type tensile testing frame was used. The system consists of a 100 N (22 lb.) load cell, pneumatic grips, and a furnace.

The pneumatic grips apply a normal force to the specimen. These grips have an 890 N (200 lb.) capacity and use smooth rubber pads for the faces in order to hold the specimen. The grips are located outside of the furnace for the high temperature tests. The upper grips are mounted to a simple universal joint. The lower grips are mounted rigidly.

The furnace has a slotted configuration and is mounted on rails. This allows the furnace to maintain the desired test temperature while being out of the way as the specimen is being installed or removed from the grips. The

furnace is a single zone type using one molybdenum disilicide element. The hot zone produces a 25 mm (1 in.) gage section. A digital controller is used to control the temperature and this controller uses a platinum/rhodium thermocouple to monitor the temperature.

A computerized data acquisition and analysis system was used to record the load and time for each test. The data was acquired through the ±10 V analog output from the tensile testing frame.

The fibers were tested individually, as opposed to tows. Tabs were utilized in the gripping area. A brief description of the specimens is provided in the next chapter.

CHAPTER III

TEST SPECIMEN CONFIGURATION

Earlier it was noted that the test specimens for this study would be fabricated from unidirectional SiC/RBSN composites and woven SiC/SiC composites. The SiC/RBSN specimens were tested from room temperature to 1550°C (2800°F) in air and 1400°C (2550°F) in an inert gas consisting of nitrogen. The SiC/SiC specimens were tested from room temperature to 1370°C (2500°F) in air. This chapter provides details regarding specific as-processed material properties and the geometry of the test specimens.

3.1 SiC/RBSN Composite System

This section covers the SiC/RBSN composite and its constituents. The test specimen geometries are presented and a brief description of the processing techniques and conditions used to make these specimens are given.

3.1.1 SiC Fibers

The fibers used in the selected composite are SCS-6[1] silicon carbide. They are cylindrical with a nominal diameter of 142 microns (μm or 5.6 mils) and consist of chemical vapor deposited (CVD) silicon carbide placed onto a 33 μm (1.3 mils) carbon core. The processing of this type of fiber was described by DiCarlo (1985). An in-depth description of the microstructure for this particular fiber was presented by Ning and Pirouz (1991). There is an approximately 3 μm (100 μin.) thick carbon rich coating on the outer surface, deposited in multiple layers, which forms an appropriate interface with the matrix material in the composite. Some geometrical data and other room temperature fiber properties are presented in Table IV. The Poisson's ratio was obtained from earlier work by Chulya et al. (1991). The coefficient of thermal expansion (CTE) was reported by Nair et al. (1991).

---

[1]Produced by Textron Specialty Materials

Fiber specimens with 200 mm (8 in.) lengths were prepared for tensile testing. The tensile tests were performed at temperatures that ranged from ambient conditions to 1550°C (2800°F) in air. One set of fibers was prepared for tensile tests in an "as-received" condition. A second set was exposed to the same processing conditions used for the SiC/RBSN composite. The fibers exposed to the composite processing conditions were laid up in plies, and sheets of graphite were used in place of the silicon slurry employed with the SiC/RBSN composite. The fiber exposure process utilized identical pressures and temperatures used with the SiC/RBSN composite. A brief description of the processing of this composite is presented later.

The fiber tensile specimens tested at room temperature had 0.13 mm (5 mil) thick aluminum foil folded over the ends in the gripped region. The

Table IV: Room Temperature Properties For SiC/RBSN Composite Constituents.

1. CVD SiC Fiber

Material: Chemical vapor deposited SiC on a carbon core with a thin carbon rich SiC coating
Diameter: 142 μm (5.6 mils)
Coefficient of Thermal Expansion: 4.4×10^{-6} °C^{-1} (2.4×10^{-6} °F^{-1})
Poisson's Ratio, ν_f: 0.22

2. Monolithic RBSN

Material: Reaction Bonded Silicon Nitride
Porosity Volume Fraction, V_p: 0.33
Coefficient of Thermal Expansion: 3.3×10^{-6} °C^{-1} (1.8×10^{-6} °F^{-1})
Poisson's Ratio, ν_m: 0.22
Fracture Surface Energy, γ_m: 36 J/m^2 (0.21 in-lbs/in^2)

aluminum foil was used as the compliant layer between the grip faces and the specimen. The specimens tested at high temperatures with an air environment were mounted on 0.23 mm (9 mil) thick cardboard tabs using a mixture of SiC powder and epoxy. Approximately 19 mm (0.8 in.) of the overall length of the fibers tested at elevated temperature is in the constructed tab. The length of each tab is approximately 50 mm (2 in.) with a width of 6.4 mm (0.25 in.). The fibers were tensile tested individually, as opposed to tensile testing tows.

3.1.2 RBSN Matrix

Monolithic RBSN coupons were fabricated, and these specimens had the same geometry as the composite coupons, that is, straight sided flat coupons with bonded tabs on each end. Each coupon was 200 mm (8 in.) long with a width of 13 mm (0.5 in.). Table IV shows selected room temperature properties of the monolithic RBSN. Poisson's ratio and matrix fracture surface energy are taken from Chulya, et al. (1991). The coefficient of thermal expansion (CTE) was taken from the work of Nair, et al. (1991). The technique for determining the porosity volume fraction is described in Appendix C.

3.1.3 SiC/RBSN Composite

The composite specimens had a fiber volume content of approximately 26%. Fibers consisted of uniaxially aligned SCS-6 CVD SiC fibers, and the matrix was reaction bonded silicon nitride. The specimen geometry consisted of 8-plies, where the fibers in each ply were spaced at approximately 4.09 fibers per millimeter (104 fibers per inch) prior to processing. Selected geometric properties are presented in Table V. Once again, the technique for determining composite porosity volume fraction is described in Appendix C.

The fabrication of the composite is summarized by Bhatt and Phillips (1990). Processing of the composite begins with the separate preparation of the fibers and a silicon tape. The fibers are then wound on a circular drum at the desired fiber spacing. Next, the fibers are coated with a fugitive polymer binder in an organic solvent. The resulting fiber mat is dried and cut into strips.

The silicon tape is a dough-like material consisting of fine silicon powder, nitridation enhancing additive, fugitive polymer binder, and a solvent. Once the components of the tape are mixed the dough is then rolled to the desired thickness and cut into strips.

Table V: SiC/RBSN Specifications.

Fiber Orientation: 0°
Fiber Volume Fraction, V_f: 0.26
Matrix Volume Fraction, V_m: 0.50
Porosity Volume Fraction, V_p: 0.24

The preform composite fabrication consists of laying up the fiber mats and the silicon tape in alternating layers in a metal die. The preform is heated in vacuum to 500°C (930°F) for binder removal. This is followed by hot pressing in vacuum or in an argon atmosphere at 1000°C. Finally, the preform composite is placed in a nitridation furnace and processed at a temperature of 1200°C (2200°F) in a constant flow of ultra pure nitrogen gas. The resulting SiC/RBSN composite panels are ground to remove any loose silicon nitride particles from the surface.

The combination of the SiC fibers and the RBSN matrix results in a composite which exhibits relatively high work of fracture. As Jamet (1989) indicated, the increased toughness for this type of material is due to the fact that the ultimate strain of the fibers is greater than the ultimate strain of the matrix, and the fiber/matrix interface allows sliding during matrix cracking, and the fibers tend to bridge the matrix cracks as they pass by the fibers. It should be noted that this composite system was studied while in the developmental stages as most CMCs are at this time.

El-Rahaiby and Solomon (1992) as well as Grathwohl (1989) have described many specimen geometries used in determining mechanical properties (especially strength) of ceramics. There is also a need to test unidirectionally reinforced ceramic matrix composites that are weak in shear relative to their longitudinal strength. This limits the number of specimen geometries that can be used successfully. The composite specimens used in this

research were flat, constant thickness, straight sided coupons with bonded tabs on either end. Glass fiber/epoxy composite tabs were used for all room temperature tests, and carbon fiber/polyimide composite tabs were utilized in high temperature tests. These tabs provided a compliant layer between the specimen and the grip faces. The tabs were bonded to the specimen using structural film adhesives. The structural film adhesives require curing temperatures of 120°C (250°F) and 180°C (350°F) for the room temperature and high temperature specimens, respectively. In the early stages of this work, metal tabs, including aluminum and copper, have been used. However, these types of tabs had large difference in CTEs between the tabs and the specimen, which led to intralaminar delamination of the SiC/RBSN composites upon cooling from the adhesive curing temperatures. For room temperature tests, specimen lengths were 114 mm (4.5 in.). The length was 200 mm (8 in.) for all high temperature tests. Note that specimen lengths for high temperature tests were dictated by the furnace height. In addition, the area near the grips had to be kept at relatively low temperatures to allow use of compliant polymer based tabs. The specimen width was 13 mm (0.5 in.) for all tests. The thickness was approximately 2.3 mm (0.09 in.). Tensile coupons were cut from a panel with a diamond impregnated abrasive wheel. There was no attempt to seal the exposed fibers at the diamond cut to protect the carbon rich interface from oxidation.

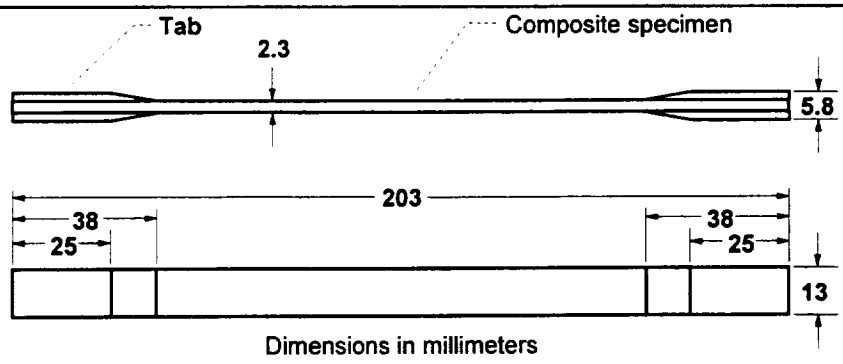

Figure 3. Flat straight sided tensile specimen with bonded tabs.

The specimen geometry was designed based on ASTM Standard D 3039-76. The specimen geometry is shown in Figure 3. ASTM Standard D 3039-76 is a standard test method for obtaining tensile properties of fiber-resin composites. The configuration has been used successfully in the past under ambient conditions with failures usually occurring within the gage section. In this research effort the carbon fiber/polyimide composite tabs were shortened to 32 mm (1.25 in.) from the ASTM standard of 38 mm (1.5 in.). The longer tabs called for in the ASTM document protruded past the grips, which caused the material to ignite when testing at high temperatures. All the tabs were 13 mm (0.5 in.) wide and 1.5 mm (0.060 in.) thick.

3.2 SiC/SiC Composite System

The SiC/SiC composite sample is a ceramic grade Nicalon[2] silicon carbide fiber reinforced enhanced silicon carbide matrix produced for AlliedSignal, Incorporated by DuPont Lanxide Composites, Incorporated. AlliedSignal supplied the specimens to NASA LeRC under an agreement through NASA's Advanced High Temperature Engine Materials Program (HiTemp).

The composite was produced by a chemical vapor infiltration (CVI) technique. The CVI technique was commercialized by the Societé Européene de Propulsion (SEP) in France according to Chawla (1993). Geoghegan (1992) describes the CVI technique as a process for forming CMCs by thermally decomposing a gaseous matrix precursor within the interstices of a porous preform. The woven Nicalon SiC fibers make up the preform in the production of the SiC/SiC composite used for this study.

Table VI: Room Temperature Properties For Nicalon SiC Fiber.

Material: mixture of β-SiC, SiO_2, and C
Diameter: 10-20 μm (390-790 μin.)
Coefficient of Thermal Expansion: $4x10^{-6}$ °C^{-1} ($2.2x10^{-6}$ °F^{-1})

Briefly, Nicalon is a multifilament fiber that consists of a mixture of β-SiC, free carbon, and silica. The fiber is produced as a yarn where each yarn

[2]Produced by Nippon Carbon Company, Ltd.

contains approximately 500 filaments as described by Takeda (1992). Selected properties of Nicalon from Chawla (1993) are presented in Table VI. The fiber tows were woven into a triaxial two-dimensional braid with yarns at 0°, 60°, and 120°, approximating a laminate in a quasi-isotropic structure. Note, the triaxial braid has fibers in three different directions in the same plane within a laminate. Five fiber plies on top of each other were chemical vapor infiltrated with enhanced silicon carbide to produce the composite. Briefly, the enhanced silicon carbide matrix consists primarily of silicon carbide with small quantities of other ceramic materials in order to improve the oxidation resistance and final density of the composite system. The added materials are proprietary. The total fiber volume fraction is approximately 40%. Seventeen percent fiber volume fraction is in the axial direction, 11.5% in the 60° direction, and 11.5% in the 120° direction. The matrix, fiber/matrix interface, and porosity made up the rest of the composite at 60% volume fraction. Porosity was approximately 10% of the composite by volume. These specifications are noted in Table VII. A similar enhanced SiC/SiC composite was described by Verrilli, et al. (1997).

The composite was supplied in 200 mm x 200 mm x 2.03 mm (8 in. x 8 in. x 0.080 in.) plates. Once delivered, the specimens were cut from the plates using wire electro-discharge machining followed by a final densification process.

Table VII: SiC/SiC Composite Specifications.

Matrix: CVI Enhanced Silicon Carbide
Fiber: Nicalon SiC
Fiber Orientations: 0°, 60°, and 120°
Fiber Volume Fraction, V_f: 0.40 ($V_{f0°}$=0.17, $V_{f60°}$=0.115, $V_{f120°}$=0.115)
Porosity Volume Fraction, V_p: 0.10

The geometry of the specimens, illustrated in Figure 3, was flat, straight sided with tabs bonded to the ends. This is the same specimen geometry that was used for the SiC/RBSN composite described in section 3.1.3. The tabs consisted of graphite fiber reinforced polyimide (graphite/PMR-15). A structural film adhesive was used to bond the tabs to the specimen.

CHAPTER IV

ALIGNMENT

In uniaxial tensile testing it is important to have the load train aligned precisely to minimize bending in the specimen. Steen and Bressers (1994) have emphasized the importance of precision alignment with the testing of CMCs. It should be noted that bending in the specimen gage section is also dependent on the gripping interface and the specimen dimensions. ASTM has a standard in place (designation E 1012-94) that outlines the alignment verification procedure. This standard was developed for testing of metallic materials. The reader should note that alignment is especially important when testing brittle, low strain-to-failure materials like ceramics. Jones and Brown Jr. (1956) as well as Hosford (1992) have pointed out that bending in tensile specimens reduces the observed load at which failure occurs. This results in conservative

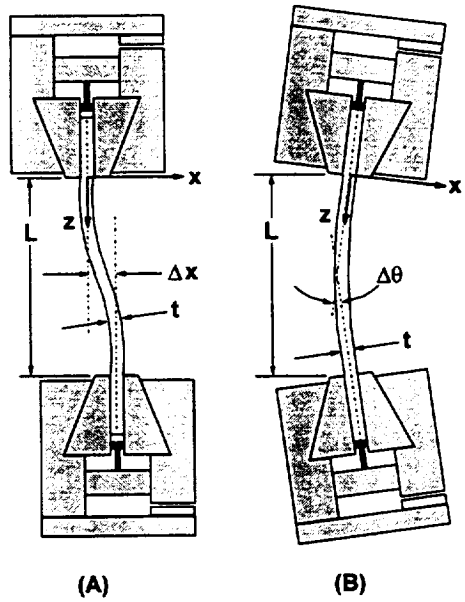

Figure 4. These are illustrations of A) lateral and B) tilt misalignment of the grips in the tensile testing system.

(i.e., underestimation of) strength data. Figure 4 presents Kotil's (1992) illustration of lateral and tilt misalignments which can be present in the load train of a tensile testing system. The additional stress can be determined by the following equations (identified as an additional bending and/or tilting normal stress) which Kotil (1992) based on simple beam theory:

$$\sigma_{B,L} = 6Et\Delta x\left[\frac{1}{2L^2} - \frac{z}{L^3}\right] \tag{4.1}$$

$$\sigma_{B,T} = \frac{Et\Delta\theta}{L^2} \tag{4.2}$$

Here:

$\sigma_{B,L}$ - bending stress due to lateral displacement of grips

$\sigma_{B,T}$ - bending stress due to tilt of grips

E - Young's modulus of the composite

t - thickness of the specimen

Δx - lateral displacement of the grips

$\Delta\theta$ - angular displacement of the grips

L - length of the specimen between the grips

z - longitudinal position along the specimen length

The maximum stress occurs at the surface of the specimen. Most of the variables in the equations are also illustrated in Figure 4.

It can be observed from equation 4.1 that the maximum bending stress due to lateral displacement of the grips occurs near the grips at the longitudinal position of z=0 or z=L. In addition, at z=L/2 equation 4.1 indicates a zero lateral bending stress. This indicates that strain gages should be mounted on a specimen near the grips to monitor bending due to lateral displacement of the grips.

Equation 4.2 shows that the bending stress, due to tilt misalignment, is constant along the length of the specimen. It was noted above that the bending strain due to lateral displacement of the grips is zero at z=L/2. As a result, to remove the effects of lateral misalignment mounting strain gages at the middle

of the specimen at z=L/2 is recommended to monitor bending due to tilt misalignment of the grips.

Finally, equations 4.1 and 4.2 indicate that bending stresses are influenced by certain geometric parameters, i.e., thickness and length. Increasing the length and/or reducing the thickness of a specimen tends to lessen bending stresses.

The alignment of the load trains was checked using untabbed aluminum bars with rectangular cross sections. Table VIII contains the geometric and material properties of the aluminum specimens, and Figure 5 illustrates one of the aluminum bars with the mounted strain gages. The aluminum properties were obtained from a handbook of materials data (Materials Selector 1988). This publication is a compilation of properties of various materials. The aluminum specimens had bonded resistance strain gages mounted on four

Table VIII: Specifications For The Aluminum Bars Used To Check The Alignment Of The Tensile Testing System Load Trains.

Material: 6061-T6 aluminum
Yield Strength: 276 MPa (40.0 ksi)
Ultimate Strength: 310 MPa (45.0 ksi)

Specimen #1
Length: 203 mm (8.0 in.)
Width: 12.77 mm (0.493 in.)
Thickness: 5.57 mm (0.229 in.)

Specimen #2
Length: 204 mm (8.0 in.)
Width: 12.53 mm (0.493 in.)
Thickness: 5.82 mm (0.229 in.)

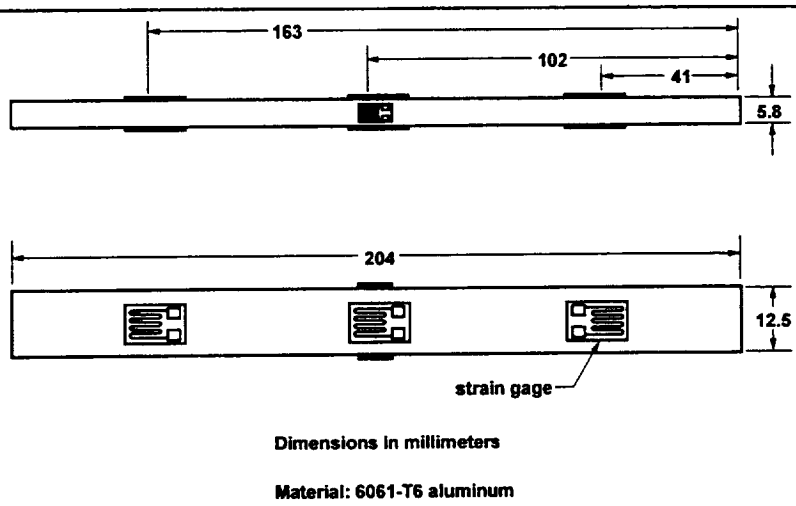

Figure 5. The aluminum bar used for checking the alignment of the load trains of the tensile testing systems.

sides at the center of each specimen. In addition, the aluminum specimens had bonded resistance strain gages mounted back-to-back near the grips. The strain gage specifications are presented in Table II.

A safety factor of 1.5 (relative to the yield strength) was used to establish maximum load for the aluminum specimens in order to avoid the onset of plastic deformation. All specimens were subjected to a stress in the gage section of 184 MPa (26.7 ksi). The corresponding maximum loads were 13.1 kN (2950 lbs) for specimen number 1, and 13.4 kN (3010 lbs) for specimen number 2, given the respective cross sectional areas of the two specimens. The specimens were stressed under load control at a rate of 20 kN/min (4500 lbs/min) which produced a stress rate of 281 MPa/min (40.8 ksi/min) in specimen number 1, and a stess rate of 274 MPa/min (39.7 ksi/min) in specimen number 2.

The percent bending was determined by using equation 4.3 which was derived by dividing the bending strain by the mean uniaxial strain, i.e.,

$$\% \text{ bending} = \frac{\varepsilon_2 - \varepsilon_1}{\varepsilon_2 + \varepsilon_1} \times 100 \tag{4.3}$$

where:

ε_1 - strain from one strain gage

ε_2 - strain from second strain gage on the opposite side of the specimen

Figures 6 through 9 depict the percent bending as a function of the mean stress in the specimen. Assuming a normal distribution, then each data point in the figures is the average, as defined in equation 4.4 from Shapiro (1990), of two to four tests. The actual number of tests per data point is noted in each of the figures. In addition, the error bars represent one standard deviation as defined by equation 4.5, also from Shapiro (1990). The standard deviation is the most common way of describing dispersion in a data set according to Dally (1993).

$$\bar{x} = \frac{1}{n}\sum x_i \tag{4.4}$$

$$s = \sqrt{\frac{n\sum x_i^2 - \left(\sum x_i\right)^2}{n(n-1)}} \tag{4.5}$$

where: $\bar{x}$ - the mean percent bending

n - the number data points

x_i - the individual data points for percent bending

s - standard deviation for percent bending

The data presented in Figures 6 and 7 are for the frame with the pneumatic wedge grips attached to the hydraulic alignment device. The system is illustrated in Figure 1. The data indicates that there is less than 2% bending within the specimen at a mean stress of greater than 50 MPa (7.3 ksi). Larsen, et al. (1993) noted that the hydraulic alignment devices are good for reducing bending but they also introduce some scatter. The same observations can be made for the system used in this study with data shown in Figures 6 and 7. Note that the bending strain is different with individual tests.

Figures 8 and 9 show the bending for the system with the rigid load train and hydraulically actuated wedge grips. The bending is less than 2% for stresses greater than 50 MPa.

The alignment of the load train is only one part of the total alignment of the system. The specimens have to be straight and flat also.

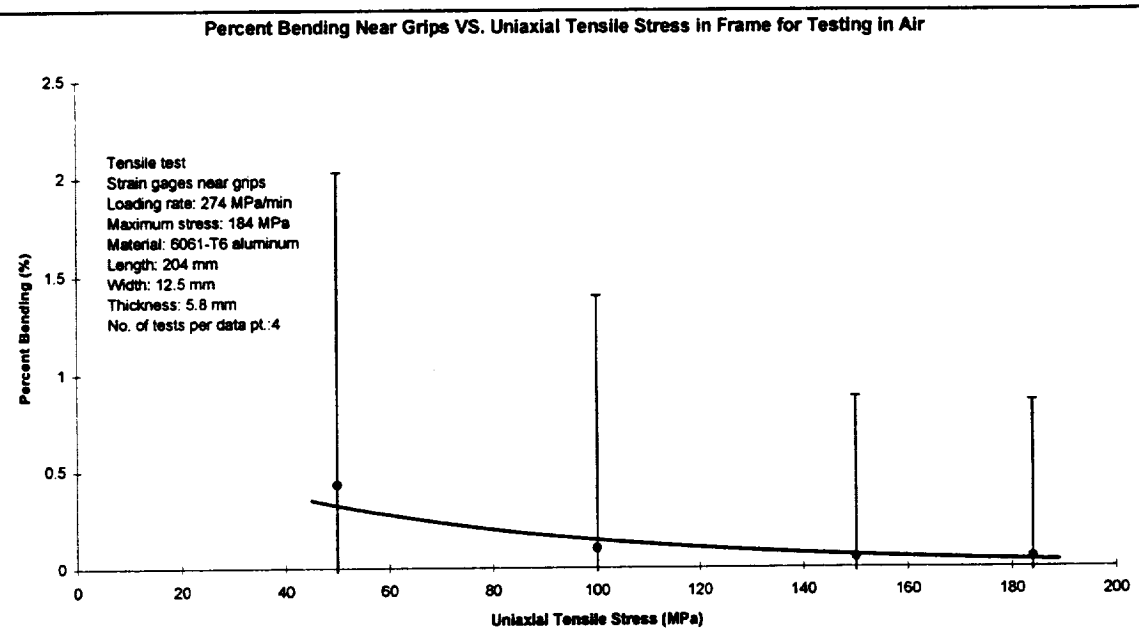

Figure 6. Percent bending near the grips versus the tensile stress in an aluminum tensile specimen. This is in the frame used for testing specimens at high temperatures in air. The frame has pneumatically actuated wedge grips with a hydraulic alignment device.

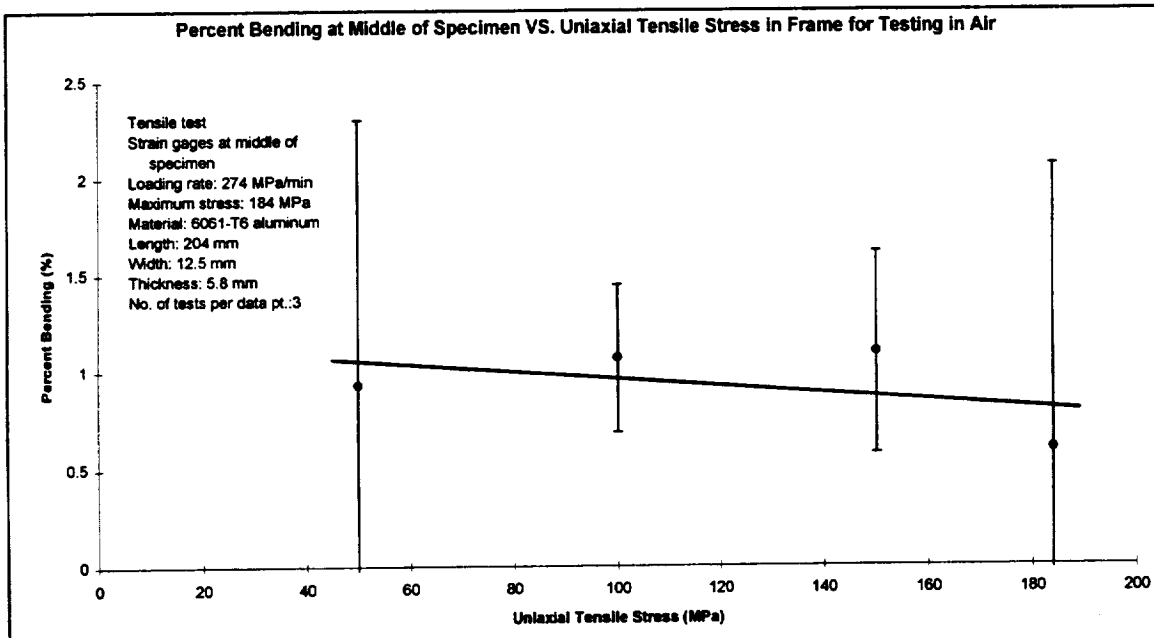

Figure 7. Percent bending at the middle of the specimen versus the tensile stress in an aluminum tensile specimen. This is in the frame used for testing specimens at high temperatures in air. The frame has pneumatically actuated wedge grips with a hydraulic alignment device.

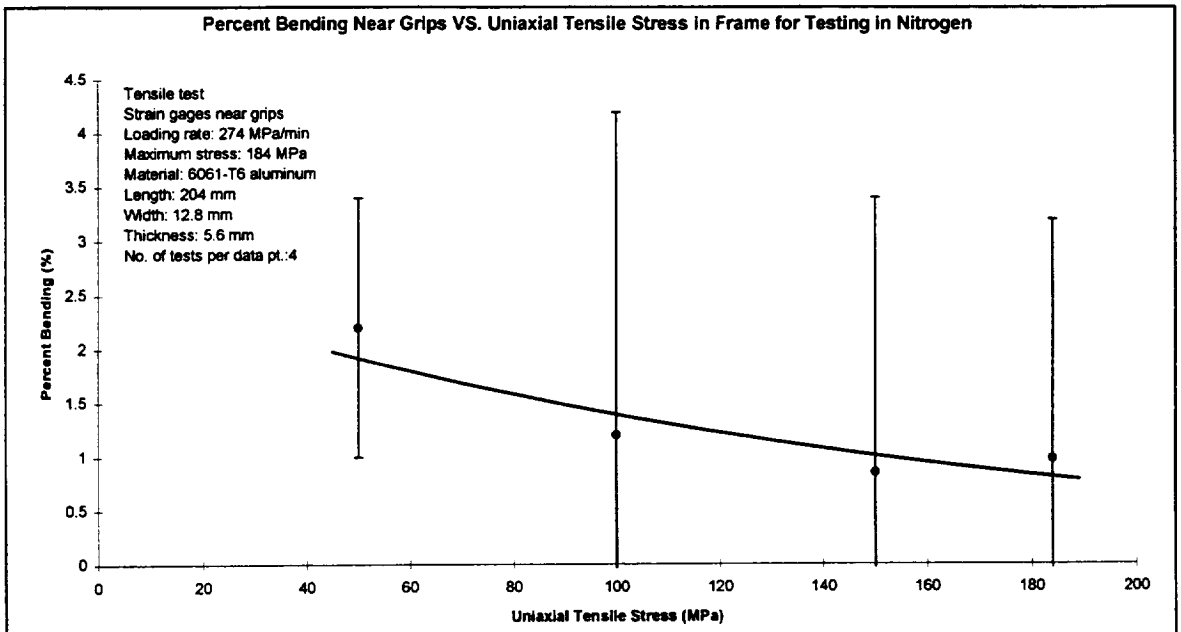

Figure 8. Percent bending near the grips versus the tensile stress in an aluminum tensile specimen. This is in the frame used for testing specimens at high temperatures in an inert gas. The frame has hydraulically actuated wedge grips mounted to a rigid train.

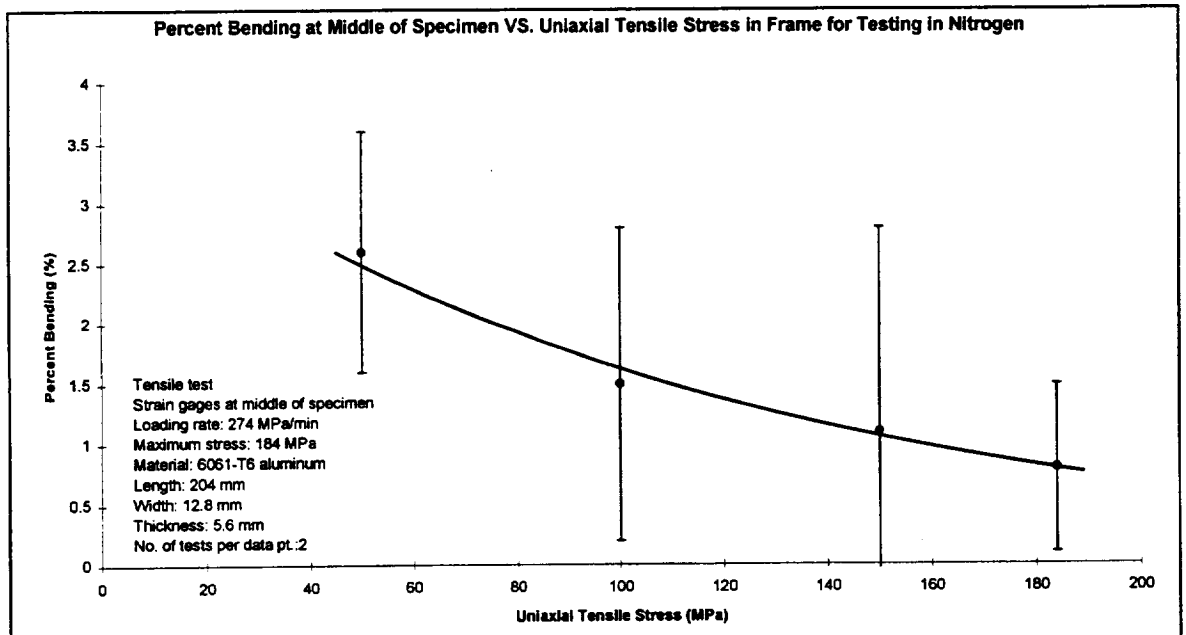

Figure 9. Percent bending at the middle of the specimen versus the tensile stress in an aluminum tensile specimen. This is in the frame used for testing specimens at high temperatures in an inert gas. The frame has hydraulically actuated wedge grips mounted to a rigid load train.

CHAPTER V

TEST PROCEDURE

Due to the limited availability of ceramic composite specimens, only two or three coupons were used for each of the test conditions.

The room temperature tests with the SiC/RBSN composites had bonded resistance strain gages on both sides of the tensile coupons to monitor the mean and bending strains. The room temperature tests with the enhanced SiC/SiC composites utilized clip-on gages mounted on opposite sides. All the specimens had the extensometers or bonded resistance strain gages attached to the flat side of the samples, as shown with the extensometers in Figure 10A with the exception of specimen number 1 of the enhanced SiC/SiC composites where the clip-on gages were mounted on the thickness side as illustrated with the extensometers in Figure 10B. It was mentioned in the previous section

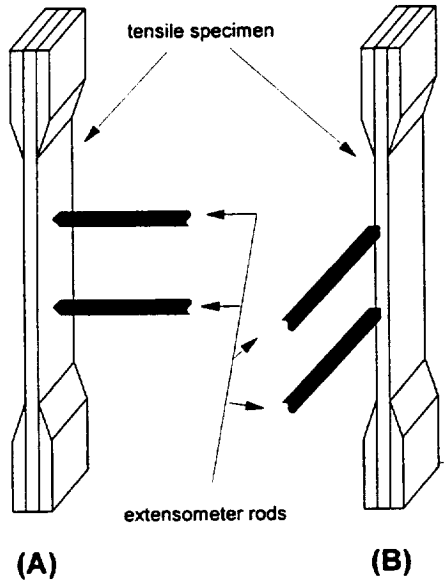

Figure 10. Extensometer rod location relative to tensile specimen.

that the SiC/RBSN specimens were cut from panels leaving exposed fibers on the cut surfaces or specimen edges. This left a surface which had debonded fibers making it difficult to obtain accurate strain measurements using the cut edges. This condition was noted by Gyekenyesi and Bartolotta (1992) and is the reason that the extensometers were not mounted as shown in Figure 10B for the SiC/RBSN composites. The specimen surface was not notched for the extensometer rods.

Bonded resistance strain gages were set up in a quarter bridge with signal conditioners. The excitation voltage was set at 2.0 volts. The conditioner output was shunt calibrated such that 10 volts corresponded to 1.0 percent strain. The clip-on gages were shunt calibrated using the tensile testing frame's controls. The gages were calibrated such that 5.0 percent strain resulted in a 10 volt output. The gages were used with the 25 mm (1.0 in.) gage

length. The mechanical extensometers were manually calibrated such that 10 volts corresponded to 1.0 percent strain.

Tests were performed on a universal, digitally controlled, tensile testing frame with an electric actuator. They were conducted in the displacement control mode which provides a constant crosshead rate. The crosshead rate was fixed at 1.00 mm/min. (0.039 in./min.). The 1.00 mm/min. (0.039 in./min.) provides a fast enough strain rate for the specimen to limit the effects of creep and oxidation, but slow enough to manually monitor and respond to any problems (i.e. with gripping or extensometry) that may arise during a test. The load cell output was shunt calibrated with the full scale of 50 kN (11 kip) equal to 10 V output.

5.1 Testing In Air

The furnace was brought up to the desired temperature before testing began for all high temperature tests in air. The heating ramp rate was a conservative 13°C per minute (23°F/min.). Pneumatic pressure for the grips was kept low at approximately 240 kPa (35 psi) for initially clamping the specimen. Then the pneumatic pressure was increased to approximately 620 kPa (90 psi). Concurrently, the crosshead was adjusted to remove any uniaxial compressive load on the specimen. Once the specimen was loaded into the grips, the furnace was pulled forward around the sample. Next, the mechanical

extensometer was inserted into the hot zone without contacting the specimen. Following stabilization of the test coupon temperature or arriving at the desired hold time for the exposure tests, the extensometer was brought into contact with the sample and the tensile test was started.

Initially, the output was recorded with analog two pen X-Y recorders. Points were manually read off the plots and the desired material properties were calculated. The modulus was determined by visually fitting a line through the linear region of the load/strain plot and calculating the modulus from the slope. Later test data were recorded by a computerized data acquisition/analysis system. The software allowed for user interaction to determine mechanical properties with a graphical interface. The cursor followed the stress/strain curve with input from the computer's keyboard and a marker was used to define various points along the curve. The user defined the beginning and end points of the linear elastic section of the stress/strain curve for the software's linear regression analysis. Also, the deviation from linearity was identified by the operator. The beginning and end points of the linear elastic region, the deviation from linearity, and ultimate strengths were identified automatically but the software allowed the operator to relocate the markers when some of the points were not clearly defined. For example, a very graceful change from the linear elastic region to the nonlinear region of the stress/strain curve and noise may make it difficult for the software to identify some of the critical points along the stress/strain curve.

5.2 Testing In Inert Gas

The specimen was inserted into the grips with only the upper grip being clamped down on the specimen end. The lower grip was brought into contact with the specimen but not clamped down. This was to avoid loading the specimen in compression during the purging process of the chamber, since the grips act like large pistons. The compliance of the load cell and the rest of the load train allows enough deflection to compress the specimen to failure. The deflection is caused by the higher atmospheric pressure acting on the outside of the grips relative to the lower pressure in the evacuated chamber. The frame could not be kept in load control to maintain a no load condition during the purging process. This is due to the fact that the load cell is outside of the chamber. Therefore, evacuating the chamber places the specimen in compression but the load cell is loaded in tension. With the load cell being in tension, the frame's control moves the crosshead to compress the load train and the specimen, increasing the compressive load on the specimen. The extensometer was also brought into contact with the specimen at this time. The lower end of the specimen was kept cool during the heating process by having the lower grip in light contact with the specimen. Next, the chamber was closed and evacuated using the vacuum pump. The chamber was pumped down to an absolute pressure of 8 Pa ($1x10^{-3}$ psi) or 60 millitorr. This was

followed by back filling of the chamber with argon or nitrogen to just above atmospheric pressure at about 30 kPa (4 psi) gage pressure. The evacuation/back filling process was repeated three more times. Once the chamber was filled with the inert gas the furnace was heated up to the desired testing temperature. The bottom grip was clamped down fully and the tensile test was initiated.

The same computerized data acquisition/analysis system was used to collect and decipher the test data as described in the previous section.

5.3 Post Tensile Test Analysis

Once the tensile tests were completed several fractured SiC/RBSN composite specimens were observed under an optical microscope to determine the average matrix crack spacing. Matrix cracks and their locations within the gage length were recorded. The mean crack spacing and its standard deviation were determined.

A section from one of the fractured enhanced SiC/SiC composites was cut with a diamond impregnated wheel. The cut was made on a plane parallel to the laminae to expose the woven fiber architecture. The section was observed under an optical microscope to determine the average fiber tow spacing within the triaxial weave. The results are used in the Results and Discussion chapter.

CHAPTER VI

THEORY

Considerable effort has been applied to the mathematical modeling of the mechanical behavior of ceramic matrix composites. A complete understanding of the mechanical behavior of these composites is necessary if designers are to make use of them for high temperature engine applications. Important properties include the stiffness, first matrix cracking stress, ultimate strength, and work of fracture from room temperature to at least 1200°C in air and inert environments.

In this section basic variables are defined for composites that are evaluated using uniaxially loaded static tensile tests. The stress in the composite is calculated from dividing the applied load by the cross sectional area of the composite shown in the following equation:

$$\sigma_c = \frac{P}{A} \tag{6.1}$$

where σ_c is the composite stress, P is the applied load, and A is the cross sectional area of the composite coupon lying in the plane perpendicular to the applied load. For a rectangular cross section the area is the product of the width and thickness of the specimen.

In unidirectional fiber reinforced composites the longitudinal load on the composite is shared by the constituents of the composite prior to failure of any of the constituents. The constituents consist of fibers and the matrix in the CMCs. Consequently, we have

$$P_{cL} = P_{mL} + P_{fL} \tag{6.2}$$

where P is the load; cL, mL, and fL refer to the composite, matrix, and fiber in the longitudinal direction, respectively. Knowing that the longitudinal load is the product of the stress in the loading direction and the cross sectional area,

$$\sigma_{cL}A_c = \sigma_{mL}A_m + \sigma_{fL}A_f \tag{6.3}$$

where σ is the stress and A is the cross sectional area of each of the constituents. Next, the equation is solved for the composite stress by dividing

through with the cross sectional area of the composite, A_c and substituting the volume fraction, V, for the area ratios. The resulting equation is referred to as the rule of mixtures for relating the longitudinal composite stress to the stresses in the constituents.

$$\sigma_{cL} = \sigma_{mL}V_m + \sigma_{fL}V_f \tag{6.4}$$

The engineering strain is defined as the change in gage length, ΔL, divided by the original gage length, L. This is expressed by the following equation:

$$\varepsilon = \frac{\Delta L}{L} \tag{6.5}$$

In the composites it is assumed that the longitudinal strain in the composite is the same as the longitudinal strain in the constituent materials in the corresponding direction within the linear elastic region of the stress/strain curve. That is, for strain compatibility,

$$\varepsilon_{cL} = \varepsilon_{fL} = \varepsilon_{mL} \tag{6.6}$$

where ε_{cL} is the composite strain, ε_{fL} is the strain in the fibers, and ε_{mL} is the strain in the matrix, all in the primary direction. A continuous fiber reinforced

composite is assumed again with no cracks, debonds, delaminations, gaps, voids, etc.

6.1 Modulus

There are five elastic constants used to describe the different stiffnesses of a transversely isotropic composite lamina. The five independent constants are

E_L - longitudinal or major modulus

E_T - transverse or minor modulus

G_{LT} - longitudinal shear modulus

ν_{LT} - longitudinal Poisson's ratio

ν_{TL} - transverse Poisson's ratio

where the subscript L denotes the longitudinal or fiber direction, and the subscript T corresponds to the in-plane transverse to the fiber direction.

The modulus of elasticity, E, is used to define the stiffness of a material. It is the slope of the linear region of a stress/strain curve and is defined as:

$$E = \frac{\Delta\sigma}{\Delta\varepsilon} \tag{6.7}$$

The stiffness of composites in the fiber direction is a function of the stiffness of the constituent materials and their respective volume fractions. Given the equation above and the assumption of longitudinal strain compatibility, by substituting into the rule of mixtures, equation 6.4, the following equation is derived for predicting the composite longitudinal modulus:

$$E_{cL} = V_f E_{fL} + V_m E_{mL} \tag{6.8}$$

where E is the modulus, V is the volume fraction, and subscripts cL, fL, and mL refer to previously defined parameters. The above equation is valid while the composite is loaded within the linear elastic range. In addition, the interfacial shear strength is assumed to be sufficient for load transfer between the fibers and the matrix. Shimansky (1989) has stated that it appears that the above equation can accurately predict the longitudinal modulus for CMCs regardless of the interfacial condition. This may be due to the low fiber/matrix interfacial shear stress usually obtained upon loading within the linear elastic region of the stress/strain curve. As a result, the assumption presented by equation 6.6 is still valid.

Shimansky (1989) reported on various techniques for determining the composite transverse modulus. Some of these methods will be covered in this section. A simple mathematical model to predict the transverse modulus of a unidirectional fiber reinforced composite in terms of the constituent moduli

was also presented by Agarwal and Broutman (1980). The transverse direction is considered to be in the plane of the laminate and perpendicular to the direction of the parallel fibers. A continuous bond between the fiber and the matrix is assumed. It should be noted that the assumption of a strong fiber/matrix interfacial bond would present an upper bound for the transverse stiffness. In addition, the fibers are assumed to be uniform in properties and diameter, continuous and parallel throughout the composite. The fiber and the matrix are modeled by layers placed in series with identical lengths and depths, and thicknesses being proportional to the respective volume fractions. A load is applied in the transverse direction. The resulting composite elongation, δ_{cT} in the direction of the load is the sum of the elongation in the fibers, δ_{fT}, and the matrix, δ_{mT}. Therefore,

$$\delta_{cT} = \delta_{fT} + \delta_{mT} \tag{6.9}$$

with the subscript T denoting the transverse direction. The elongation of each constituent is the product of the strain and the cumulative thickness, t, of the respective constituent, so that

$$\delta_{cT} = \varepsilon_{cT} t_c \tag{6.10}$$

$$\delta_{fT} = \varepsilon_{fT} t_f \tag{6.11}$$

$$\delta_{mT} = \varepsilon_{mT} t_m \tag{6.12}$$

Substituting the above equations into equation 6.9 the result is

$$\varepsilon_{cT} t_c = \varepsilon_{fT} t_f + \varepsilon_{mT} t_m \tag{6.13}$$

Equation 6.13 is divided through by the composite thickness, t_c. The constituent thickness ratios are proportional to the constituent volume fractions resulting in the following equation:

$$\varepsilon_{cT} = \varepsilon_{fT} V_f + \varepsilon_{mT} V_m \tag{6.14}$$

The constituents are assumed to deform elastically with the applied load. Applying Hooke's law, $\sigma = E\varepsilon$, the resulting equation is

$$\frac{\sigma_{cT}}{E_{cT}} = \frac{\sigma_{fT}}{E_{fT}} V_f + \frac{\sigma_{mT}}{E_{mT}} V_m \tag{6.15}$$

Here, E_{cT} is the composite transverse modulus. Since, the fibers and the matrix are in series the stress in the loading direction within the constituents is the same, that is

$$\sigma_{cT} = \sigma_{fT} = \sigma_{mT} \tag{6.16}$$

Applying the condition presented in equation 6.16 to equation 6.15 the resulting equation for the transverse modulus of the composite, E_{cT}, with a strong fiber/matrix interfacial bond is

$$E_{cT} = \left[\frac{V_f}{E_{fT}} + \frac{V_m}{E_{mT}}\right]^{-1} \tag{6.17}$$

In case of a weak or frictional fiber/matrix interface, which is common in most CMCs, it can be assumed that the fibers offer little or no contribution to the composite transverse tensile modulus. This is due to the fact that the applied load is not transferred to the fibers from the matrix by the interface. Therefore, the transverse tensile modulus of the composite is primarily a function of the matrix stiffness with the fibers acting like holes within the matrix. Shimansky (1989) describes a unidirectional composite with a weak fiber/matrix interface as a matrix containing cylindrical voids for the transverse stiffness analysis. The cylindrical voids may be treated as porosity within the matrix. The procedure for accounting for porosity is covered later in section 6.2. Another technique makes use of Halpin's and Tsai's (1969) generalized empirical equations to estimate properties of unidirectional fiber

reinforced composites. These equations offer a simplified solution relative to the more complex micromechanical equations. Bhatt and Phillips (1990) used the empirically developed equations of Halpin and Tsai (1969), given by equation 6.18 below, and set the transverse fiber modulus, E_{fT}, to zero to model weak interface CMCs. The result, with $E_{fT}=0$, is presented in equation 6.19.

$$E_{cT} = E_{mT}\left[\frac{1+\xi\eta V_f}{1-\eta V_f}\right] \tag{6.18}$$

$$E_{cT} = E_{mT}\left[\frac{2-V_f}{1+V_f}\right] \tag{6.19}$$

where

$$\eta = \frac{\frac{E_{fT}}{E_{mT}} - 1}{\frac{E_{fT}}{E_{mT}} + \xi}$$

and $\xi = 2$ for cylindrical fibers. The variable, ξ, is a measure of reinforcement and is a function of fiber geometry, packing geometry, and loading conditions. Shimansky (1989) showed that the Halpin and Tsai equation with the fiber modulus set equal to zero compared well with a finite element analysis of a composite containing a debonded fiber/matrix interface.

The shear modulus of a lamina, G, is a function of the shear moduli of the constituents. For this study the constituents are assumed to be isotropic. Thus, the shear moduli of the constituents are calculated using the following equation:

$$G = \frac{E}{2(1+\nu)} \tag{6.20}$$

where E is modulus of elasticity and ν is the Poison's ratio for the constituents, respectively. Agarwal and Broutman (1980) used Halpin's and Tsai's (1969) generalized empirical equations to also predict the composite shear modulus. The results are accurate for fiber volume fractions of less than 55%, at least for composites with strong fiber/matrix interfaces. The Halpin and Tsai (1969) approximation of the shear modulus is

$$G_{LT} = G_m\left[\frac{1+\xi\eta V_f}{1-\eta V_f}\right] \tag{6.21}$$

where

$$\eta = \frac{\frac{G_f}{G_m}-1}{\frac{G_f}{G_m}+\xi}$$

and ξ is assumed to be one per suggestion of the authors. Bhatt and Phillips (1990) have suggested setting the fiber shear modulus, G_f, equal to zero in the above equation as with the equation for determining the transverse tensile modulus for the case of a debonded fiber/matrix interface.

Next, the modulus near the ultimate strength of the composite is analyzed. It is assumed that the fiber failure stress and strain is greater than the matrix failure stress and strain, respectively. Therefore, the composite stiffness near the ultimate strength is mainly a function of the fiber stiffness with little or no contribution from the matrix. This is due to the fibers carrying all the load with negligible support from the by then widely cracked matrix. Using the rule of mixtures, the composite modulus near the ultimate strength of the composite is

$$E_{cL2} = E_{fL}V_f \tag{6.22}$$

The above equation assumed that the majority of the fibers remain intact.

6.1.1 Modulus With A Triaxially Woven Fiber Architecture

Woven fiber architectures increase the complexity of analytically predicting composite properties relative to simple unidirectionally reinforced

composites. In this section various techniques will be presented that predict the longitudinal modulus of a triaxially woven two dimensional fiber reinforced lamina.

One technique for modeling two dimensional woven fiber reinforced composites is to assume a composite laminate consisting of unidirectional fiber reinforced laminae oriented in the same directions as the woven fibers. This usually leads to an upper bound for stiffness and strength since the fibers are assumed to be straight in the laminae. A triaxially woven (0°/60°/120°) fiber reinforced composite can be modeled as a composite consisting of at least five equal thickness plies with a $[\pm 60/\bar{0}]_s$ lay-up. A symmetrically constructed laminate having a 0° ply at the center with +60° plies at the outer surfaces and a -60° ply between the 0° ply and each +60° ply. The $[\pm 60/\bar{0}]_s$ composite layup approximates the triaxially woven composite with a minimum number of plies. The order of the 60° plies is not significant as long as the symmetric construction is maintained. The symmetric construction of the composite uncouples the axial and bending reactions as noted by Agarwal and Broutman (1980). This is due to the resulting sections of the overall stiffness matrix of the laminated composite that couple the axial and bending reactions being zero. The ply volume fractions are divided such that the total volume of the fibers, matrix, and porosity are the same as for the triaxially woven fiber composite. Swanson and Smith (1996) and Masters, et al. (1992) also compared braids and laminates by calculating an equivalent laminate using this

technique. Each equivalent unidirectional ply is analyzed to determine the longitudinal stiffness, transverse stiffness, shear stiffness, and Poisson's ratio from the constituent properties. Finally, the stiffness of each lamina is transformed to the longitudinal direction of the specimen. The stiffness transformation is performed using

$$E_x = \left[\frac{\cos^4\theta}{E_L} + \frac{\sin^4\theta}{E_T} + \frac{1}{4}\left(\frac{1}{G_{LT}} - \frac{2\nu_{LT}}{E_L} \right) \sin^2 2\theta \right]^{-1} \tag{6.23}$$

where E_x is the laminate elastic modulus along the primary axis of the laminated composite. Equation 6.23 is derived by using stress and strain tensorial transformations substituted into the equation $E_x=\sigma_x/\varepsilon_x$. The direction of interest is the longitudinal direction of the specimen. The major Poisson's ratio, ν_{LT}, of each lamina is determined by using the rule of mixtures

$$\nu_{LT} = V_f\nu_f + V_m\nu_m \tag{6.24}$$

Finally, the total laminate stiffness in the loading direction is determined through summing the contributions of all the laminate plies. The longitudinal modulus of the laminate is calculated by rationing the number of laminae in the different directions. Thus,

$$E_{cL} = \frac{n_{0°}}{n_{tot}} E_{x0°} + \frac{n_{60°}}{n_{tot}} E_{x60°} \tag{6.25}$$

where $n_{0°}$ is the number of 0° plies, $n_{60°}$ is the number of +60° and -60° plies, and n_{tot} is the total number of plies. Equation 6.25 is only valid for the case where all the plies have the same geometric dimensions, as presented by Agarwal and Broutman (1980).

In attempt to increase the accuracy of the predicted response of the composite it is necessary to account for the undulations in the fibers of the weave. Chou and Ishikawa (1989) showed a technique using shape functions to model a composite with a square weave fiber architecture. This work was used by Mital, et al. (1996) with reasonable success to predict the modulus of a SiC/SiC plain weave composite and was expanded to model composites with a triaxially woven fiber architecture. The approach starts with the composite being modeled with a $[\pm 60/\bar{0}]_s$ lay-up as illustrated in Figure 11. A unit cell (Figure 12) is taken to identify the triaxial weave of the composite with

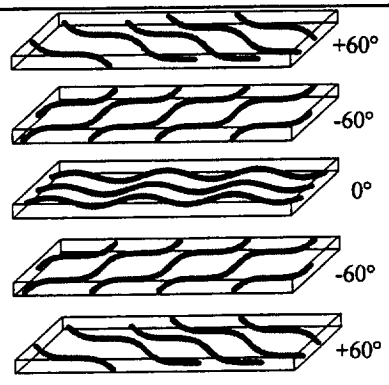

Figure 11. Laminated composite with $[\pm 60/\bar{0}]_s$ architecture and undulating fibers.

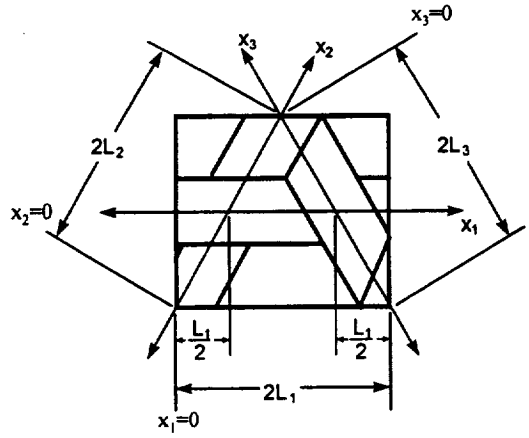

Figure 12. Unit cell for a triaxial woven architecture as presented by Yang and Chou (1989).

coordinates and selected dimensions. The individual fiber tows along the x_1, x_2, and x_3 directions with their undulations are represented by the illustrations in Figure 13. The following shape functions, as presented by Yang and Chou (1989), mathematically define the geometric undulations of the fibers. The shape functions for the fiber tows along the x_1, x_2, and x_3 directions are

$$Z(x_1) = \left[1 + \sin\frac{\pi x_1}{L_1}\right]\frac{H}{2} \qquad (0 \le x_1 \le 2L_1) \tag{6.26}$$

$$Z(x_2) = \left[1 - \sin\left(\frac{x_2}{L_2} - \frac{1}{2}\right)\pi\right]\frac{H}{2} \qquad (0 \le x_2 \le 2L_2) \tag{6.27}$$

$$Z(x_3) = \left[1 + \sin\left(\frac{x_3}{L_3} - \frac{1}{2}\right)\pi\right]\frac{H}{2} \qquad (0 \le x_3 \le 2L_3) \tag{6.28}$$

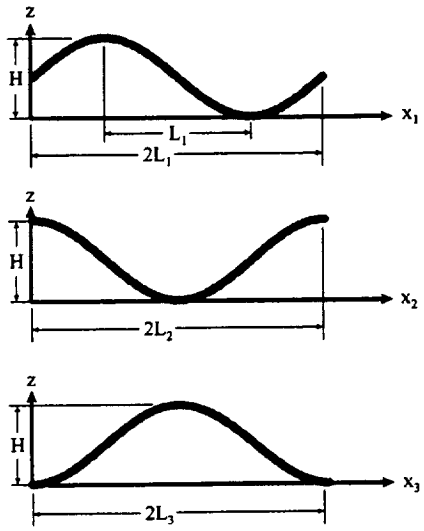

Figure 13. Geometric undulation in fiber as presented by Yang and Chou (1989).

where H is the thickness of the undulated lamina and L is one half of the fiber tow spacing. Equation 6.29 differentiates the shape functions with respect to their axis to determine the local off axis angle, ϕ, at any point along the length of each fiber tow, that is

$$\phi_i = \tan^{-1}\left[\frac{dZ(x_i)}{dx_i}\right] \tag{6.29}$$

where the subscript, i, is 1, 2, or 3. The off axis angle is the instantaneous angle of the longitudinal axis of the fiber relative to the axis along the fiber direction within the plane of the lamina. The local angle, ϕ, is used to determine the lamina properties at the selected point along the fiber tows. The following equations are used to predict the various properties of the laminae as a function of ϕ:

$$E_L(\phi) = \left[\frac{\cos^4\phi}{E_L} + \left(\frac{1}{G_{LT}} - \frac{2\nu_{LT}}{E_L}\right)\sin^2\phi\cos^2\phi + \frac{\sin^4\phi}{E_T}\right]^{-1} \tag{6.30}$$

$$E_T(\phi) = E_T \tag{6.31}$$

$$\nu_{LT}(\phi) = E_L(\phi)\left[\frac{\nu_{LT}\cos^2\phi}{E_L} + \frac{\nu_{TL}\sin^2\phi}{E_T}\right] \tag{6.32}$$

$$G_{LT}(\phi) = \left[\frac{\sin^2\phi}{G_{TT'}} + \frac{\cos^2\phi}{G_{LT}}\right]^{-1} \tag{6.33}$$

where the subscript TT' refers to the plane defined by the in-plane transverse axis, T, and the out of plane axis, T'.

It is assumed that each composite lamina segment is loaded with the same stress. Next, the strain in the fiber tows is determined as a function of the angle, ϕ.

$$\varepsilon_L(\phi) = \frac{\sigma_L}{E_L(\phi)} \tag{6.34}$$

$$\varepsilon_T(\phi) = -\nu_{LT}(\phi)\frac{\sigma_L}{E_L(\phi)} \tag{6.35}$$

The average strains along the longitudinal axis of each lamina are derived by integrating the above equations as shown by the equations below

$$\bar{\varepsilon}_L = \frac{1}{2L}\int_0^{2L} \varepsilon_L(\phi)\, dx \tag{6.36}$$

$$\bar{\varepsilon}_T = \frac{1}{2L}\int_0^{2L} \varepsilon_T(\phi)\, dx \tag{6.37}$$

After determining the average strains in the fiber tows the average moduli and the major Poisson's ratio can be calculated using equations 6.38 through 6.40.

$$\bar{E}_L = \frac{\sigma_L}{\bar{\varepsilon}_L} \tag{6.38}$$

$$\bar{E}_T = E_T \tag{6.39}$$

$$\bar{\nu}_{LT} = -\frac{\bar{\varepsilon}_T}{\bar{\varepsilon}_L} \tag{6.40}$$

The average shear modulus is:

$$\overline{G}_{LT} = \frac{1}{2L}\int_{0}^{2L} G_{LT}(\phi)\, dx \tag{6.41}$$

Equations 6.23 and 6.25 are again used to determine the laminate modulus and the overall composite stiffness, respectively, in the longitudinal direction of the specimen containing the undulated fiber tows.

6.2 Porosity

Porosity within a material usually reduces its stiffness and strength when compared to a fully dense material. Moulson (1979) has shown that the stiffness of a material is an exponential function of the porosity. He proposed the following equation for the elastic modulus:

$$E = E_o e^{-3P} \tag{6.42}$$

where

E_o - Young's modulus of the fully dense material

P - Fraction of porosity between 0 and 1 where P=0 for a fully dense material

For a composite where all the porosity is in the matrix Equation 6.43 below gives the porosity volume fraction, $V_{p,m}$. This equation was derived in Appendix C and is used to show how the porosity within the matrix changes with introduction of the reinforcing fibers.

$$V_{p,m} = \frac{V_p}{V_m + V_p} \tag{6.43}$$

6.3 Matrix Cracking and Interfacial Shear Properties

In addition to studying the composite modulus, the proportional limit, in the direction of the fibers, needs to be investigated. It is assumed that the proportional limit on a stress/strain curve and the first matrix cracking stress are the same. This is a common assumption, as noted by Woodford and his associates (1993). The first matrix crack is taken by definition as the first through the cross section crack, wherein only the fibers are left to carry the total composite load. Any minor cracking within the composite before this condition or load is reached, is ignored in this definition. As noted earlier, it is assumed that the fiber failure stress and strain is greater than the matrix failure stress and strain, respectively. The first matrix cracking stress is the onset of permanent major damage in a composite making it a critical design parameter. Shimansky (1989) describes the cracking process for CMCs with an

increasing load as usually initiating with microcracks within an amorphous region at the fiber/matrix interface. The microcracks coalesce upon further increase in the applied load, forming major matrix cracks perpendicular to the loading axis that eventually traverse the whole composite cross-section. As the applied load continues to increase the matrix cracks at other points along the load axis. Finally, the matrix becomes saturated with regularly spaced parallel cracks. Once the composite matrix is saturated with cracks the remaining fiber/matrix interface area with each matrix segment is insufficient to transfer an adequate load to cause the matrix to fracture into smaller segments.

The first matrix cracking stress is dependent on many parameters. One of the key parameter is the fiber/matrix interfacial shear strength. Kerans (1989) has noted that the interfacial shear strength is difficult to characterize and may vary with location. In this work, the fiber/matrix interfacial shear strength is determined from matrix crack spacing measurements in a composite that has been loaded to or near its ultimate strength. Loading a specimen near the ultimate strength leads to matrix crack saturation. The average crack spacing for each specimen is used to determine the mean fiber/matrix interfacial shear strength, τ, using the equation

$$\tau = \frac{\beta \, R \, V_m \, E_m \, \sigma_y}{2 \, V_f \, E_c \, x} \tag{6.44}$$

where β=1.337 from Kimber and Keer (1982), R is the fiber radius, σ_y is the composite stress where matrix cracking initiates, and x is the mean crack spacing. This equation is derived from a simple summation of forces within the composite as presented by Aveston, et al. (1971). The derivation is shown in Appendix A. Aveston, et al. showed that the crack spacing is between x and 2x. Kimber and Keer (1982) demonstrated analytically that the crack spacing was closer to 1.337x. This equation is deterministic since it is assumed that the composite stress where matrix cracking initiates, that is σ_y, is constant.

Hsueh (1988 and 1990) presented an equation for determining the critical interfacial shear strength below which interfacial debonding occurs, without fiber fracture, upon matrix cracking. The theory was derived by modeling the composite as concentric cylinders with a fiber surrounded by the matrix. The ratio of the square of the radii of the fiber and the matrix are equal to the fiber volume fraction. This equation is

$$\tau_{cr} = \frac{(1 - V_f)E_m\sigma_{fu}}{\left\{2(1 + \nu_m)E_f\left[V_fE_f + (1 - V_f)E_m\right]\left[V_f - 1 - \ln(V_f)\right]\right\}^{\frac{1}{2}}} \qquad (6.45)$$

A few of the variables were defined earlier. These include the variables, E, V, and ν referring to the Young's modulus, volume fraction, and Poisson's ratio, respectively. The subscripts of f and m refer to the fiber and matrix, respectively. The variable, σ_{fu}, is the mean ultimate strength of the fiber.

In most composite systems there is a coefficient of thermal expansion (CTE) mismatch between the fibers and the matrix. This results in residual stresses within the composite at temperatures other than the processing temperature. The following equation from Budiansky, et al. (1986) is used to determine the axial residual stress within the matrix:

$$\sigma_{m\alpha} = \left[E_m \frac{\phi_2}{\phi_1}\right]\left[\frac{E_f}{E_c}\right]\left[\frac{V_f}{1 - \nu_m}\right]\varepsilon_T \tag{6.46}$$

where:

$$\varepsilon_T = (\alpha_f - \alpha_m)\Delta T \tag{6.47}$$

$$\Delta T = (T - T_{proc}) \tag{6.48}$$

$$\phi_1 = 1 - 0.5\left[\frac{1 - 2\nu}{1 - \nu}\right]\left[1 - \frac{E_c}{E_f}\right] \tag{6.49}$$

$$\phi_2 = 0.5\left[1 + \frac{E_c}{E_f}\right] \tag{6.50}$$

The variables α_f and α_m are the coefficients of thermal expansion for the fiber and matrix, respectively. The processing temperature is T_{proc} and the test

temperature is T. The Poisson's ratio, ν, for the fiber and the matrix is assumed to be the same as noted in Table IV.

Aveston, et al. (1971) derived an equation for predicting the composite stress where matrix cracking initiates in brittle matrix composites. This is commonly referred to as the ACK theory and the result is presented in equation 6.51. The parameters include the fiber/matrix interfacial shear strength τ, the matrix fracture surface energy γ_m, the fiber radius R, the constituent volume fractions V, and constituent moduli E.

$$\sigma_y = \left[\frac{12\tau\gamma_m E_c^2 E_f V_f^2}{E_m^2 V_m R} \right]^{\frac{1}{3}} \tag{6.51}$$

Note that the above equation is independent of crack size. It is a discrete model that was derived using an energy balance approach. The ACK theory uses the change in energy states within the composite from just prior to matrix crack initiation to just after the crack propagates completely through the matrix. Important assumptions included are: (1) the fiber failure strain is greater than the matrix failure strain, (2) a frictional interfacial bond between the fiber and the matrix exists, and (3) the fibers can bear the load without any support from the matrix.

Chawla (1993) pointed out some limitations or problems with the ACK theory. First, the theory indicates that the matrix strain to failure, or the first

matrix cracking stress in equation 6.51, goes to zero as the fiber volume fraction goes to zero, whereas, the limit should be the strain or stress to failure of the monolithic matrix material. The model predicts that the strain to failure increases with increasing fiber/matrix interfacial shear strength. Unfortunately, the theory does not account for the limitation where fiber/matrix interfacial debonding and/or sliding does not occur. The lack of relative displacement at the fiber/matrix interface prevents fiber bridging of the matrix crack, resulting in linear elastic behavior.

Aveston, et al. (1971) considered a weakly bonded fiber/matrix interface, as an upper limit, also. It was assumed that the interfacial debonding energy G_{II} is unlikely to exceed the matrix fracture energy, γ_m. As an upper constraint G_{II} is set equal γ_m. The result is a third degree polynomial function of the matrix cracking strain, ε_{mu}, as presented in the following equation:

$$\varepsilon_{mu}^3 - \frac{12\gamma_m E_f V_f^2}{E_m V_m E_c R}\varepsilon_{mu} - \frac{12\gamma_m \tau E_f V_f^2}{E_m^2 V_m E_c R} = 0 \qquad (6.52)$$

All the other assumptions applied to equation 6.51 apply to the above equation also.

Another equation for predicting the first matrix cracking stress was developed by Marshall and Cox (1988) using the crack closure pressure suggested by McCartney (1987). This approach was applied by Chulya, et al. (1991) to SiC/RBSN to calculate the first matrix cracking stress. Marshall and

Cox (1988) used linear elastic fracture mechanics and assumed a single crack, loaded in mode I, propagating through a semi-infinite medium. The traction from the bridging fibers was superimposed on the crack model as closing pressure. The resulting equation is similar to the ACK results. Marshall and Cox also assumed a weak frictional fiber/matrix interface with bridging fibers. The resultant equation for predicting the composite stress where steady state matrix cracking begins within the lamina is

$$\sigma_y = \left[\frac{6\tau\gamma_m E_c^2 E_f V_f^2}{E_m^2 V_m R} \right]^{\frac{1}{3}} \tag{6.53}$$

Combining equations 6.46 and 6.53 leads to an equation which predicts the composite cracking stress with residual stress effects included. The result is

$$\sigma_{y\alpha} = \sigma_y - \sigma_{m\alpha} \frac{E_c}{E_m} \tag{6.54}$$

Danchaivijit and Shetty (1993) and Budiansky, et al. (1986) have pointed out that the ACK result, as well as equation 6.53 above, lead to lower bound predictions.

6.4 Fiber Properties

As mentioned earlier, ceramic matrix composites contain fibers that have a higher failure strain than the matrix. As a result, the composite's mechanical properties are fiber dominated near the material's ultimate strength. This section discusses the behavior of ceramic fibers in preparation for analyzing the ultimate strength of unidirectional composites.

Most brittle materials, including ceramic fibers, show a large variation in their tensile strength. Therefore, it is appropriate to apply statistical techniques for predicting their reliability and probability of failure. Statistical analysis allows the designer to use data generated from a small sample to systematically predict the stochastic response of complex structures.

Bergman (1984) reported that the cumulative distribution function proposed by Weibull (1939) is the most useful for characterization of brittle materials. Weibull analysis is based on the weakest link theory, where failure is assumed to occur at the largest flaw within the material. The theory is purely statistical in nature. It should be noted that a single flaw population and a strength that is independent of time will be assumed. The three parameter Weibull cumulative distribution function for the failure probability of ceramic fibers is

$$P_f = 1 - e^{-\int_v \left(\frac{\sigma - \sigma_t}{\sigma_0}\right)^m dV} \tag{6.55}$$

where P_f is the probability of failure by fracture at a given stress, σ, m is the shape factor, known as the Weibull modulus, V is the stressed volume, σ_0 is the scale factor, and σ_t is the location parameter defined as the threshold stress below which the probability of failure is zero. The scale factor, σ_0, has the dimension of stress times (volume)$^{1/m}$ for P_f to be dimensionless. The above equation can be simplified by taking the conservative assumption of setting the threshold stress to zero, assuming uniaxial fiber stress acting in a material volume with only internal imperfections. Consequently, equation 6.55 can be expressed as

$$P_f = 1 - e^{-V\left(\frac{\sigma}{\sigma_0}\right)^m} \tag{6.56}$$

The above equation is linearized by taking the natural logarithm twice, resulting in the following equation:

$$y = \ln\left[\ln\left(\frac{1}{1-P_f}\right)\right] = \ln(V) + m\ln\left(\frac{\sigma}{\sigma_0}\right) \tag{6.57}$$

This equation can be plotted on a Weibull plot of y versus ln σ wherein the Weibull modulus, m, is the slope of the plotted line. The Weibull characteristic strength may be substituted for the volume and Weibull scale parameter to

simplify the above equations. The Weibull characteristic strength, σ_θ, is a function of the Weibull scale parameter, σ_o; the stressed volume, V; and the Weibull modulus, m; as shown in the following equation:

$$\sigma_\theta = \frac{\sigma_o}{V^{\frac{1}{m}}} \tag{6.58}$$

Equation 6.59 is valid for the condition where the stress is evenly distributed over the volume, V, as is the case in uniaxial tension. Substituting equation 6.58 into equations 6.56 and 6.57 we get

$$P_f = 1 - e^{-\left(\frac{\sigma}{\sigma_\theta}\right)^m} \tag{6.59}$$

$$y = \ln\left[\ln\left(\frac{1}{1-P_f}\right)\right] = m \ln\left(\frac{\sigma}{\sigma_\theta}\right) \tag{6.60}$$

Pai and Gyekenyesi (1988) report that the least squares analysis and maximum likelihood method are the most popular techniques for estimating Weibull parameters from experimental data. The least squares method offers simplicity. with the estimated Weibull modulus being the slope of the best fit line by linear regression on a Weibull plot of y versus ln(σ). Bergman (1984) also states that the use of the least squares method implies that the ln σ values

follow a Gaussian distribution around the line obtained from equation 6.57. The maximum likelihood technique is a nonlinear model offering efficiency and is better suited to model uniaxial strength data of brittle ceramics. ASTM (1995) has a standard (Designation: C 1239-94a) utilizing the maximum likelihood technique for estimating the Weibull parameters. The maximum likelihood method will be used for this work. The likelihood function, from the ASTM (1995) standard, for the two-parameter Weibull distribution, with a single-flaw population or uncensored data set is

$$\mathcal{L} = \prod_{n=1}^{n_{tot}} \left(\frac{m}{\sigma_\theta}\right)\left(\frac{\sigma_n}{\sigma_\theta}\right)^{m-1} e^{-\left(\frac{\sigma_i}{\sigma_\theta}\right)^m} \tag{6.61}$$

where n is the rank of a specimen and n_{tot} is the total number of specimens in a sample.

The estimates of the Weibull modulus and the characteristic strength are determined by taking the partial derivatives of the natural logarithm of the likelihood function, equation 6.61, with respect to m and σ_θ and equating the resulting expressions to zero. Following are the resulting equations, for an uncensored sample, which are to be solved numerically.

$$\frac{\sum_{n=1}^{n_{tot}} \sigma_n^m \ln(\sigma_n)}{\sum_{n=1}^{n_{tot}} \sigma_n^m} - \frac{1}{n_{tot}} \sum_{n=1}^{n_{tot}} \ln(\sigma_n) - \frac{1}{m} = 0 \tag{6.62}$$

$$\sigma_\theta = \left[\left(\sum_{n=1}^{n_{tot}} \sigma_n^m \right) \frac{1}{n_{tot}} \right]^{\frac{1}{m}} \tag{6.63}$$

The ASTM (1995) standard, designation C 1239-94a, states that the estimated Weibull modulus tends to be statistically biased. The bias is a function of the sample size. The bias decreases as the sample size is increased. The ASTM (1995) standard, designation C 1239-94a, provides a table of unbiasing factors as a function of sample size.

A probability estimator is used to give the probability of failure for each failure stress. These probability values are used to calculate y for a given corresponding stress. The measured fracture strengths of the fibers are ranked in ascending order. The following estimator is used to calculate the failure probability:

$$P_n(\sigma_n) = \frac{n - 0.5}{n_{tot}} \tag{6.64}$$

where n is the rank of the specimen data point and n_{tot} is the sample size. Other common probability estimators were discussed by Bergman (1984). The

above probability estimator, which gives an average value of the empirical density function about the corresponding stress, is most useful for small samples of less than 50 as discussed by Bergman (1984). Also, the probability estimator of equation 6.64 is part of the ASTM (1995) standard, mentioned above.

6.5 Ultimate Strength

The ultimate strength of these composites is primarily dependent on fiber properties. The strength properties of CVD SiC fibers, as a function of temperature, were measured in separate tests.

A simple approximation for predicting the composite ultimate tensile strength utilizes the rule of mixtures and the mean fiber strength. For the unidirectional lamina, assuming that the in-situ fiber and the independent fiber strengths are identical and that the matrix carries no load, we have

$$\sigma_{cu} = V_f \sigma_{fu} \tag{6.65}$$

where: σ_{cu} - the composite ultimate strength

σ_{fu} - the mean fiber ultimate strength

It is further assumed here that all the fibers are intact until just prior to the composite ultimate loading.

The assumption of uniformly strong fibers would be the ideal situation, but in practice the fibers tend to fail sequentially starting with the weakest fiber, until the applied load cannot be supported leading to total fracture. Since the fibers are brittle and exhibit stochastic behavior, it is more appropriate to apply statistics to determine their ultimate strength. Duffy, et al. (1991) have pointed out that the strength distribution of the fibers needs to be incorporated into an analytical model for predicting the ultimate strength of the composite.

Equation 6.66 from Curtin, et al. (1993) and Curtin (1993) has been used to determine the composite's ultimate strength in terms of fiber properties.

$$\sigma_{cu} = V_f\left(\frac{2}{m+2}\right)^{\frac{1}{m+1}}\left(\frac{m+1}{m+2}\right)\left[\frac{\sigma_{fu}^m \tau L_f}{R\ln(2)}\right]^{\frac{1}{m+1}} \tag{6.66}$$

where: L_f - fiber gage length at which the strength was determined

m - Weibull modulus of fiber

σ_{fu} - mean fiber strength

It is of interest to compare the above result to that found for a "dry" bundle containing only fibers and no matrix. The composite strength based on bundle ultimate strength, σ_{cub}, can be calculated, per Evans, et al. (1995), from

$$\sigma_{cub} = V_f \sigma_{fu} \left(\frac{L_f}{L_c} \right)^{\frac{1}{m}} e^{-\frac{1}{m}} \tag{6.67}$$

where L_c is the fiber bundle gage length and L_f is the fiber length used to determine σ_{fu} and m. In all cases, the composite ultimate strength, σ_{cu}, is greater than the fiber bundle strength, σ_{fub}.

Evans (1989), as well as Evans and Marshall (1989), presented a model for predicting the composite ultimate strength based on weakest link statistics, incorporating the fiber Weibull modulus, m. The model is a modified bundle failure analysis which assumes failed fibers have no load bearing ability. The model of the modified bundle failure theory is presented in the following equation:

$$\sigma_{cubm} = V_f \sigma_{fub} e^{-\frac{1-\left(1-\frac{\pi x}{R\sigma_{fub}}\right)^{m+1}}{(m+1)\left[1-\left(1-\frac{\pi x}{R\sigma_{fub}}\right)^{m}\right]}} \tag{6.68}$$

The fiber bundle strength, σ_{fub}, is determined by iteratively solving the following equation:

$$\left(\frac{R\sigma_{fub}}{\tau x}\right)^{m+1} = \frac{A_o}{2\pi RL_c}\left(\frac{R\sigma_o}{\tau x}\right)^m\left[1-\left(1-\frac{\tau x}{R\sigma_{fub}}\right)^m\right]^{-1} \tag{6.69}$$

where τ is the interfacial shear stress as defined by equation 6.44, x is the saturated matrix crack spacing, R is the fiber radius, L_c is the composite gage length, and A_o is an area normalizing factor. The scale parameter, σ_o, is defined, according to Chulya, et al. (1991), by the following equation:

$$\sigma_o = \frac{\sigma_{fu}}{\Gamma\left(1+\frac{1}{m}\right)}(2\pi RL_f)^{\frac{1}{m}} \tag{6.70}$$

Here L_f is the fiber gage length and Γ is Euler's gamma function, defined as:

$$\Gamma\left(1+\frac{1}{m}\right) = \int_0^\infty t^{\left(1+\frac{1}{m}\right)-1}e^{-t}dt \tag{6.71}$$

Cao and Thouless (1990) made an attempt to predict the ultimate strength of a ceramic composite with the application of two parameter Weibull statistics. Their theory assumed that the matrix is saturated with cracks. As a result, the initial linear elastic behavior and the nonlinear deformation associated with matrix cracking are not incorporated. Another simplifying assumption is that upon fracture of a fiber anywhere within the gage length of

the composite, the fiber is unable to carry any load. Given the assumptions, the following equation is used to predict the ultimate strength of a ceramic composite:

$$\sigma_{cu} = V_f \Sigma \left(\frac{\Sigma R}{m(m+1)\tau L_c} \right)^{\frac{1}{m}} e^{-\frac{1}{m}} \tag{6.72}$$

where:

$$\Sigma = \left[\frac{A_o \sigma_o^m \tau (m+1)}{2 \pi R^2} \right]^{\frac{1}{m+1}} \tag{6.73}$$

As with the other theories in this section, this theory is based on fiber statistics, primarily the Weibull modulus and the scale parameter, and the variables are as defined in the statistical failure theories above.

6.5.1 Ultimate Strength With A Triaxially Woven Fiber Architecture

As in unidirectionally fiber reinforced composites, the ultimate strength of the woven fiber reinforced composite is fiber dominated. Dadkhah, et al. (1995) have concluded that the off axis braids, the ±60° fibers of the SiC/SiC in this work, do not contribute significantly to the axial strength of a triaxially woven fiber reinforced composite. The work of Dadkhah, et al. (1995) was based on triaxially woven glass fiber reinforced urethane composites with axial tows and braids ranging from ±39° to ±54°. As a result, axial strength is primarily dependent on the strength of the fibers in the axial direction. The

ultimate strength of the composite can be approximated using the volume fraction of axial fibers and the theories mentioned above for unidirectional fiber reinforced composites. According to Dadkhah, et al. (1995) equation 6.65 is a good empirical guide to strength in the axial direction.

6.6 Modulus of Toughness

The concept of introducing fibers into ceramic matrices is to improve the toughness of the material. One parameter that gives an estimate of the toughening effect of fibers is the area under the tensile stress/strain curve of the composite. This area, referred to as the modulus of toughness, U_T, is determined by integrating the stress with respect to the strain from zero to the composite fracture strain, ε_{cf}. This is illustrated with the following equation

$$U_T = \int_0^{\varepsilon_{cf}} \sigma \, d\varepsilon \tag{6.74}$$

The technique is currently being reviewed by ASTM to provide an interim technique for determining the ability of the composite to sustain damage.

CHAPTER VII

RESULTS AND DISCUSSION

In this chapter the high temperature tensile test results are presented and compared with theory to predict the mechanical behavior of the selected CMCs. First, the unidirectional fiber reinforced SiC/RBSN composite system will be addressed in section 7.1. Next, the triaxially woven fiber reinforced SiC/SiC composite system will be discussed in section 7.2.

7.1 SiC/RBSN Composite System

Stress-strain curves from individual tensile tests of SiC/RBSN specimens are presented in Figures 14 through 22 to illustrate typical curves at various temperatures in air and nitrogen. Figure 14 shows one SiC/RBSN

stress/strain curve at each temperature on one chart to illustrate the deteriorating properties with increasing temperature. Figures 15 through 22 are the individual SiC/RBSN stress/strain curves with more detail of the mechanical properties. All the specimens exhibited pseudo-toughness, or an ability to sustain progressive damage, from room temperature to 1550°C (2820°F) in air and to 1400°C (2550°C) in nitrogen. These temperatures were selected to represent potential service conditions, and in view testing equipment limitations. The stress-strain curves show a linear elastic region, followed by matrix cracking producing the nonlinear region. A second linear region can be observed as the curves approach the ultimate strength of the composite. The second linear region is attributed to the fibers supporting the applied load with little or no contribution from the matrix. Again, it should be noted that these were short term tests in which oxidation of the specimens tested in air was limited. As a result, no significant differences were noted between specimens tested in air or nitrogen at the same temperature. The measured mechanical properties for all the short term static tensile tests for the SiC/RBSN composite system are presented in Tables IX for the air environment and X for the nitrogen environment. Missing values in the tables are due to difficulties encountered with the recording device or the strain measuring device during a test.

A limited number of specimens were tested by exposure to a static oxidizing environment prior to loading. The exposure tests were conducted in

the same tensile testing system as the other high temperature tests in air for this work. The specimen was mounted in the grips with no load applied. The Furnace was held at the desired temperature. The exposure times consisted of one and four hours. As with the short term tests all the specimens exhibited pseudo-toughness or an ability to sustain damage up to 1550°C (2820°F) in air. The mechanical properties are presented in Tables XI and XII.

A preliminary group of tests were conducted to study the ability to support a load near the first matrix cracking stress at high temperatures in an oxidizing environment. The tests are used to determine the time to failure by fracture. Specimens were loaded until the deviation from linearity was observed or first matrix cracking stress on the stress/strain curve. Once, the first matrix cracking stress was reached, the load was held until failure by fracture at 1400°C (2550°F) in air. With the mean first matrix cracking stress being established, another group of specimens were loaded to approximately to 80% of the first matrix cracking stress and held there until failure by fracture. The environment consisted of air at 1400°C (2550°F) also. The data are presented in Table XIII.

7.1.1 Tensile Modulus of SiC/RBSN

Figure 23 and Table XIV show the Young's modulus of the composite as a function of temperature. The measured moduli, including tests in air and

nitrogen, and the moduli calculated from the rule of mixtures are plotted. The rule of mixtures values were calculated using Equation 6.8. The fiber moduli were taken from DiCarlo (1986) and the room temperature monolithic RBSN modulus, E_{RBSN}=110 Gpa (16x10^6 psi), was taken from Chulya, Gyekenyesi, and Bhatt (1991). The monolithic RBSN modulus at 1000°C (1800°F) was measured to be 90 GPa (13x10^6 psi) in air and 82 Gpa (12x10^6 psi) in nitrogen. The monolithic RBSN also had a modulus of 82 Gpa (12x10^6 psi) at 1400°C (2550°F) in nitrogen. The other values were derived using linear interpolation for the RBSN moduli at 600°C (1110°F) and 800°C (1470°C) in air and extrapolation for the RBSN modulus at 1400°C (2550°F) in air. The constituent moduli as a function of temperature are presented in Table XV.

Porosity was determined in the monolithic RBSN and the SiC/RBSN composites as outlined in Appendix C. Table XVI presents the results. Measuring an average porosity volume fraction of P=0.33 in the monolithic RBSN and a room temperature modulus of E=110 GPa (16x10^6 psi) equation 6.42 results in a theoretical modulus of E_o=296 GPa (43x10^6 psi) for a fully dense material (P=0). This compares well with the 300 GPa (44x10^6 psi) used by other researchers for a fully dense RBSN specimen, as pointed out by Moulson (1979).

The porosity volume fraction within the composite was determined to be V_p=0.24. All the porosity within the SiC/RBSN composite is in the matrix. Equation 6.43 was derived, as discussed in Appendix C, using this assumption,

and is used for determining the porosity volume fraction with respect to the matrix volume, $V_{p,m}$.

The porosity within the matrix of the composite was calculated to be $V_{p,m}$=0.32. This shows that the porosity within the matrix does not change significantly with the introduction of the fibers in this composite system. Table XV reflects this by showing that the modulus of the monolithic RBSN, E_{RBSN}, is nearly the same as the calculated modulus for the RBSN matrix, E_m, in the SiC/RBSN composite. There were concerns that the fibers would hinder the even distribution and conversion of the silicon to silicon nitride during processing of the SiC/RBSN composite, resulting in a lower average matrix density relative to monolithic RBSN.

Up to 1400°C (2500°F) there is good correlation between the measured composite moduli, in air and nitrogen, and the moduli derived from the rule of mixtures using constituent properties. This can be observed in Figure 23 and Table XIV. At 1550°C (2820°F) in air, excessive scatter in the test data existed from specimen to specimen. Some of the discrepancy is believed to be due to creep in one or more of the constituents of the composite. Other research has been conducted to evaluate the creep properties of CVD type SiC fibers by Morscher and DiCarlo (1991) and SiC/RBSN composites by Holmes and Chermant (1993) and by Holmes, Jones, and Bhatt (1992). Morscher, et al. (1995) and DiCarlo, et al. (1997) have shown significant creep in the CVD SiC fibers at 1400°C (2500°F). The results from DiCarlo, et al. (1997) show fiber

creep strain over 0.5% within an hour of exposure to 1400°C (2550°F) in air under stress at 270 MPa (39 ksi). It is difficult to relate the fiber creep properties with the SiC/RBSN composite due to the large transient behavior of the fibers before reaching a steady state creep rate. Hilmas, Holmes, Bhatt, and DiCarlo (1993) have observed a creep rate of 5.1×10^{-8} per second at 150 MPa (22 ksi) at only 1300°C (2370°F) in the SiC/RBSN composite. The 150 MPa (22 ksi) load is near the first matrix cracking stress at temperatures above 600°C (1110°F). The recrystallization of the SiC in the fiber above 1400°C (2550°F) is another mechanism that causes a degradation in the mechanical properties of the fiber as observed by Bhatt (1994).

It was mentioned at the beginning of this section that most of the composites exhibited a linear region just prior to the ultimate strength. This is attributed to the fibers carrying all the load, with negligible support from the matrix. Using the rule of mixtures, the composite modulus near the ultimate strength of the composite should be the product of the fiber modulus and the fiber volume fraction, as indicated by equation 6.23. The matrix is assumed to have negligible load bearing ability. The measured and predicted values for the secondary modulus near the ultimate strength of the SiC/RBSN composite are presented in Table XVII. Unfortunately, the rule of mixtures significantly over-predicts the secondary moduli. Bhatt (1990) had similar results for room temperature tests of SiC/RBSN. Daniel, Anastassopoulos, and Lee (1993) had similar results with a SiC/CAS composite system also, and surmised that the

difference may be due to some of the fibers being damaged within the composite. It should be noted that Equation 6.23 is based on the rule of mixtures with the assumptions that all the fibers are intact and the composite stress is equally distributed among the fibers.

Using Weibull statistics the probability of failure for individual fibers was determined for the average stress at the initiation of the secondary modulus, E_{c2}. Mechanical properties of CVD SiC fibers, including failure strength statistics, are covered in greater detail in Sections 6.4 and 7.1.3. The secondary moduli, composite stress and calculated fiber stress at the initiation of the secondary moduli region, and the corresponding fiber failure probability are presented in Tables XVIII and XIX. Table XVIII presents data for specimens tested in air and Table XIX presents data for specimens tested in nitrogen. The fiber stresses are derived from the composite stresses using the rule of mixtures with the assumption that the matrix is saturated with cracks and does not carry a significant load. Tables XVIII and XIX indicate a maximum failure probability of 0.4% at 1000°C (1800°F) in a nitrogen environment. This indicates that nearly all the fibers should be intact at the initiation of the secondary linear region for all the tests. One possible cause for the discrepancy in moduli is that the exposure time at temperature differs for the fibers and the composite due to the different thermal masses. It takes considerably more time for the composite specimen to heat up to the test temperature relative to the time it takes the fiber to reach the same

temperature. As a result, there is a chance the carbon coating on the fiber may have oxidized to a greater degree in the composite, reducing the fiber modulus within the composite. It is possible that the processing conditions of the SiC/RBSN damaged the fibers enough to significantly raise the probability of failure at the stress levels of the secondary linear region. The assumption that the composite stress is evenly distributed among the reinforcing fibers may not hold true by the secondary linear region. The matrix damage may be extensive enough to preclude the even loading of all the fibers which would result in the lower secondary modulus. This requires further study.

A few specimens were exposed to high temperatures in air for a fixed duration prior to loading to study the effects of oxidation on the mechanical properties. The data are presented in Tables XI and XII with one hour and four hours exposure, respectively. The Young's moduli are plotted for different temperatures versus time of exposure in Figure 24. The figure indicates insignificant changes in modulus as a function of time at temperature up to 4 hours of exposure. It should be noted that there was only one specimen tested at each temperature for the four hour tests. Bhatt (1992) showed a weight loss of approximate 0.5% for the SiC/RBSN composite from zero to roughly four hours of exposure to flowing oxygen of 99.99% purity at 600°C (1110°F). At 1000°C (1830°F), Bhatt (1992) showed approximately 0.4% loss from zero to one hour of exposure to flowing oxygen. The same work showed a weight loss of approximately 1% in the first few minutes of exposure to the flowing oxygen

followed by a weight gain of approximately 5% by about four hours of exposure to flowing oxygen at 1400°C (2550°F). The specimens in this work were exposed to static air which should have reduced the oxidation rate relative to Bhatt's (1992) work. The result is that the oxidation that occurred was not enough to change the composite modulus in these tests.

7.1.2 Matrix Cracking and Interfacial Shear Properties for SiC/RBSN

The effect of temperature on the proportional limit also was studied. It was assumed that the proportional limit, on a stress/strain curve, and the first matrix cracking stress were the same. The first matrix cracking stress is the onset of permanent damage in a composite, making it a critical design parameter.

The first matrix cracking stress is affected by various parameters. One of these parameters is the fiber/matrix interfacial shear strength. Other parameters are addressed later in this section. It has been noted by Kerans, et. al. (1989) that the interfacial shear strength is difficult to characterize with certainty. In this case the fiber/matrix interfacial shear strength is determined as a function of matrix crack spacing in a composite that has been loaded to or near the ultimate strength of the composite. Loading a specimen near the ultimate strength results in the number of matrix cracks reaching a saturation value. Figure 25 and Table XX illustrate the average matrix crack spacing as a

function of temperature in air and nitrogen. Significant scatter was observed in the matrix crack spacing as indicated by the first standard deviations accompanying the mean values in Table XX and the error bars in Figure 25. Cho, Holmes, and Barber (1992) had similar results with uniaxial SiC/CAS and they concluded that a large variance is to be expected in the crack spacing distribution even when the matrix strength has low scatter. The matrix crack spacing was measured using an optical microscope. Next, the average crack spacing for each specimen was used to determine the mean fiber/matrix interfacial shear strength, τ, using equation 6.44. It is assumed that the matrix is characterized by a single value for strength. Yang and Knowles (1992) have made an attempt to apply Weibull statistics to characterize the matrix crack spacing with limited success, but more in depth analysis is required.

Table XX shows the theoretical critical interfacial shear strength as a function of mean fiber strength below which fiber/matrix debonding occurs without fracturing the bridging fibers upon matrix cracking. The critical interfacial shear strength, τ_{cr}, is calculated using equation 6.45 and the mean ultimate strength of treated fibers presented in Table XXII. It can be observed in Table XX that the fiber/matrix interfacial shear strength of the SiC/RBSN composite is significantly below the calculated theoretical critical interfacial shear strength that allows fiber pullout to occur. The data also indicates that the ultimate strength of the fibers would have to degrade by almost an order of

magnitude before the toughening effect of the fibers in the matrix becomes negligible.

Referring to Figure 25 or Table XX it is difficult to conclude how matrix crack spacing varies with temperature. This may be due to other properties changing significantly enough to affect the crack spacing. Figure 26 and Table XX show the calculated interfacial shear strength, using equation 6.44, as a function of temperature in air and nitrogen. As with the matrix crack spacing the interfacial shear strength does not seem to vary significantly with temperature. The room temperature interfacial shear strength of 8.5 MPa (1.2 ksi), from Figure 26 or Table XX, compares reasonably well with the previously published value of 8.1±0.5 MPa (1.2±0.1 ksi) by Eldrige and Honecy (1990) which was derived from fiber push-out tests. It is within the same order of magnitude as the interfacial shear strength of 10 MPa (1.5 ksi) derived, using equation 6.12, from specimens tested in flexure by Bhatt (1985). These values include the radial residual stress effect. The interfacial shear stress can vary significantly within a composite due to variations in processing conditions, matrix porosity, and effects of neighboring fibers as proposed by Chulya, Gyekenyesi, and Bhatt (1991). Research is continuing to identify a test for accurately determining the interfacial shear strength between the fiber and the matrix of various composite materials. This includes tensile tests of single fibers coated with the matrix material by Morscher, Martinez-Fernandez, and Purdy (1994) and fiber push-out tests by Eldridge, Bhatt, and Kiser (1991).

Eldridge and Ebihara (1994) and Eldridge (1995) developed a high temperature fiber push-out system capable of testing specimens up to 1100°C (2010°F) in a vacuum environment. The small size of the push-out specimen results in the carbon fiber/matrix interface being completely exposed to the atmosphere making it impractical to do push-out tests at high temperatures in an oxidizing environment. Eldridge's (1995) results show greater fiber/matrix interfacial shear strengths for the SiC/RBSN composites tested in a vacuum than the results of this work where the composites were tested in air. At room temperature, Eldridge's (1995) results show an interfacial shear strength of approximately 13 MPa (1.9 ksi) as opposed to 8.5 MPa (1.2 ksi) derived from matrix crack spacing in this work. At 600°C (1110°F) and 800°C (1470°F), Eldridge (1995) showed approximate interfacial shear strengths of 24 MPa (3.5 ksi) and 27 MPa (3.9 ksi), respectively. Table XX indicates shear stresses of 11.4 MPa (1.7 ksi) and 8.9 MPa (1.3 ksi) at 600°C (1110°F) and 800°C (1470°F) in air, respectively. At 1000°C, Eldridge (1995) showed an interfacial shear strength of 26 MPa (3.8 ksi) as opposed to 8.4 MPa in air and 13.6 MPa (2.0 ksi) in nitrogen observed in this work. Differences are believed to be due to Poisson's effect and oxidation. Push-out tests place the fiber in compression, therefore, increasing the diameter and resulting interfacial shear stress. Tensile tests place the fibers in tension, therefore, decreasing the diameter of the fiber and reducing the interfacial shear stress.

The CTE for the matrix and fibers are different, as shown in Table IV, with α_f=4.4x10^{-6} °C^{-1} for the fiber and α_m=3.3x10^{-6} °C^{-1} for the matrix. This results in residual stresses within the composite at temperatures other than the processing temperature. The processing temperature of 1200°C (2200°F), as noted by Bhatt (1986), is used as the reference temperature at which there are no residual stresses due to the CTE mismatch within the composite. Equation 6.46 is used to determine the residual stress within the matrix. The Poisson's ratio, ν, for the fiber and the matrix is assumed to be the same as in the work of Chulya, et al. (1991) and noted in Table IV at $\nu=\nu_f=\nu_m$=0.22.

The stress values at the proportional limit are illustrated in Figure 27 and Table XXI. Table XXI presents additional results from the ACK theory with the assumption of a bonded fiber/matrix interface. The interfacial debonding energy, G_{II}, is assumed to equal the matrix fracture energy, γ_m, at 36 J/m^2 (0.21 in-lb$_f$/in^2). Aveston, et al. (1971) have suggested that the interfacial debond energy is not likely to exceed the matrix fracture energy. Equating the two parameters presents an upper limit for the ACK theory. In addition, Eldridge, et al. (1991) have observed the presence of a very weakly bonded interface from their work with push-out tests. The resulting polynomial, equation 6.52, was solved using a numerical technique utilizing the secant method. The composite stress at which matrix cracking initiated was calculated from the resulting critical strain and the composite modulus using Hooke's law. The results are presented in Table XXI. It can be observed in

Table XXI that the assumption of an interface at G_{II}=36 J/m^2 (0.21 in-lb$_f$/in^2) significantly overestimates the first matrix cracking stress. The predicted stress levels are comparable to the ultimate strength of the SiC/RBSN composite from room temperature to 600°C (1110°F). The assumption that the matrix fracture energy equals the fiber/matrix interfacial debonding energy for the ACK theory produces results that exceed the measured ultimate strength from 800°C (1470°F) to 1550°C (2820°F). As a result, the rest of the work in this section is based on the assumption of a frictional fiber/matrix interface.

Looking at Figure 27 and Table XXI we find that the predicted values of the ACK theory (equation 6.51) and the Marshall and Cox theory combined with the McCartney theory (equation 6.54) were conservative at temperatures below approximately 800°C (1470°F) while not accounting for residual stresses and assuming a frictional fiber/matrix interface. The same theories predict values that are fairly accurate at temperatures above approximately 800°C (1470°F). The ACK theory, with the assumption of a frictional fiber/matrix interface and not accounting for residual stresses, is recognized as a lower bound as pointed out by Danchaivijit and Shetty (1993) and Budiansky, Hutchinson, and Evans (1986), although, the Marshall-Cox theory combined with McCartney's theory, and not accounting for residual stresses, results in a more conservative prediction.

Equation 6.54 is used to modify the theories mentioned above to incorporate the effects of residual stresses. This produces overly optimistic

predictions for the first matrix cracking stress from room temperature to approximately 1000°C (1830°F) for the ACK theory. The Marshall and Cox theory combined with the McCartney theory over-predicts the first matrix cracking stress at room temperature, but produces fairly accurate results from approximately 600°C (1110°F) to 1000°C (1830°F) while accounting for residual stresses. Above approximately 1000°C (1830°F), the theories produce conservative predictions while accounting for residual stresses. At 1200°C (2190°C) the theoretical residual stresses are considered to be zero, producing the same predictions from the respective theories whether the residual stresses are accounted for or not. From Figure 27 it can be observed that the slope of the curves accounting for the constituent CTE mismatch is greater in magnitude than the experimentally derived curve. This may be an indication that the residual stresses may not be as great as initially assumed. It is possible that some of the residual stresses are relieved due to the weak fiber/matrix interface. Another possible source of discrepancy is that matrix cracking may have initiated prior to the proportional limit. There were no through the matrix cracks observed in the specimen surface prior to testing. Chawla (1993) noted that it is not unusual to observe small but distinct cracks in the matrix well before extensive, large scale cracking occurs. Chulya, Gyekenyesi, and Bhatt (1991) showed that acoustic emissions, due to matrix cracking, were detected before the proportional limit, although this is believed to be just microcracking where the crack propagation is arrested. Most

composite cracks do occur where the proportional limit is observed on the stress/strain curve. Detecting possible modulus changes, due to matrix cracking, before the proportional limit was below the resolution of the tensile testing equipment.

One of the variables in the equations for predicting the first matrix cracking stress is the interfacial shear stress. The shear stress is calculated from the matrix crack spacing as noted above. There was significant scatter in the matrix crack spacing. As a result, this could have been another meaningful source of error. Oxidation may have also increased the discrepancy between the measured and predicted values of the stress at the proportional limit. In fact, Bhatt (1992) has shown that the carbon fiber/matrix interface oxidizes significantly within the composite between 600°C (1110°F) and 1000°C (1830°F) due to oxygen entering through the matrix porosity. Above 1000°C (1830°F) the matrix porosity is sealed by the formation of silica at the composite surface. Bhatt (1992) showed that the reduction in mechanical properties for specimens treated in flowing oxygen between 600°C (1110°C) and 1000°C (1830°F) was primarily due to the oxidation of the fiber/matrix interface. Although, Bhatt's (1992) work was with room temperature residual mechanical properties after treating the specimens under flowing oxygen at high temperatures.

Figure 28 illustrates the first matrix cracking stress as a function of time at high temperatures in air for different temperatures. The curves show a

slight decrease in the first matrix cracking stress for exposure times of zero hours to one hour of exposure for the test temperatures of 600°C (1110°F), 1000°C (1800°F), and 1400°C (2550°F). There is an insignificant change in the first matrix cracking stress between one hour and four hours of exposure time at the test temperatures of 600°C (1110°F) and 1400°C (2550°F). (It should be noted that there was only one specimen tested at each temperature with the four hour exposure.)

It is believed that the majority of the oxidation of the carbon interface between the fiber and the matrix takes place within the first hour of exposure. Chu, et al. (1993 and 1995) have suggested, it is possible that the carbon interface is replaced by weak oxide layers. Also, it is possible that silica formed on the surface of the composite within the first hour of exposure reducing the oxidation rate of the constituents. Bhatt (1992) has shown that at 1200°C (2200°F) and 1400°C (2550°F) oxidation of the RBSN matrix quickly seals the porosity, reducing the oxidation rate of the fiber/matrix interface. It was noted in the section on the modulus that Bhatt (1992) showed weight loss in the SiC/RBSN composite in the first few minutes to exposure to oxygen at 1400°C (2550°F) followed by a weight gain, due to the formation of silica, effectively sealing the composite.

7.1.3 CVD SiC Fiber Properties

The CVD SiC fibers were tested in an "as-received" condition and a treated condition. The untreated fibers were taken directly off the spool on which they were delivered and then tested. Another set of fibers were put through the processing conditions of the SiC/RBSN composites using the same temperatures and pressures to determine the effects on the tensile strength of the fibers. The processing conditions are covered in the chapter on the specimen configuration.

The properties including the ultimate strength of individual fibers, mean ultimate strength with a variance of one standard deviation, Weibull modulus, and Weibull characteristic strength as a function of temperature for the CVD SiC fibers are presented in Table XXII. In addition, the mean fiber ultimate strengths with one standard deviation are plotted as a function of temperature in Figure 29. Figures 30 through 36 present the two-parameter Weibull plots with $Ln(Ln(1/(1-P_f))$ versus the fiber ultimate strength for the 'as-received' CVD SiC fibers. In addition, the same figures illustrate the 90% confidence bounds as determined using the ASTM (1995) standard designation C 1239-94a. Figures 37 through 43 present the same information for treated CVD fibers. Figures 44 and 45 present the Weibull moduli as a function of temperature with 90% confidence bounds for the 'as-received' and the treated fibers, respectively.

The Weibull modulus is determined by numerically solving equations 6.62 and 6.63, which are part of the maximum likelihood method.

The data from Table XXII and Figure 29 indicate a steady decrease in ultimate strength with increasing temperatures from room temperature to 1550°C (2820°F). The mean strength for the untreated fibers compares well with previously published data by DiCarlo (1991). The effects of the processing conditions seem to be negligible when comparing the mean ultimate strengths of the treated and untreated fibers. Weibull moduli do not seem to be affected to any significant degree from room temperature to approximately 1550°C (2820°F) for either the 'as-received' or the treated fibers. The one exception is the slight increase in the Weibull modulus for the 'as-received' fibers tested at 1400°C (2550°F) in air. It is known that the strength is heavily dependent upon surface and volume defects in the fibers. It is believed that the effect from the intrinsic degradation of the material overcomes the effects from surface and volume defects increasing the consistency of the ultimate strength. The intrinsic degradation is attributed to grain growth, as noted by Bhatt and Hull (1993). Although, the Weibull modulus did not change significantly at the high temperatures possibly indicating minimal changes in the fibers chemical makeup. The scatter of the Weibull moduli as a function of temperature with the wide confidence bounds may be an indication that a larger sample of fibers is needed.

Additional data are presented in Table XXIII for the treated CVD SiC fibers. The Weibull modulus, m, and the characteristic strength, σ_θ, were derived by the maximum likelihood method as mentioned above. Also, the mean fiber stresses at the initiation of the secondary moduli in the SiC/RBSN with the corresponding probability of failure are presented in the same table. The probability of failure at the given stress was determined using the Weibull cumulative distribution function, equation 6.59. The results showed a very low probability of failure for the fibers at the initiation of the secondary modulus for the SiC/RBSN composites. The highest probability of failure is 0.4% at 1000°C (1830°F) in a nitrogen environment. These results were used in the previous section analyzing the secondary modulus of the SiC/RBSN composite.

7.1.4 Ultimate Tensile Strength of SiC/RBSN

The ultimate strength of these composites are primarily dependent on fiber properties. The strength properties, as a function of temperature, of the CVD SiC fibers were measured in separate tests and discussed in the previous section.

The ultimate tensile strengths of the composites are plotted as a function of temperature in Figure 46. The plot includes the mean ultimate strength with one standard deviation from tensile tests in air and nitrogen and theoretical curves using constituent properties, that is the treated fiber

properties. The same properties are presented in Table XXIV. Figure 46 and Table XXIV indicate an insignificant change in the ultimate strength of the SiC/RBSN composite from room temperature to approximately 600°C (1110°F). A significant drop in ultimate strength occurs near 800°C (1470°F) followed by a smaller reduction in strength up to 1550°C (2820°F). No significant differences in the ultimate strength were noted for tests in air and nitrogen for the short term tests, although, the tests in nitrogen were only conducted at 1000°C (1830°F) and 1400°C (2550°F).

It can be observed in Figure 46 and Table XXIV that the rule of mixtures, equation 6.65, over-predicts the ultimate strength considerably. It is only at 1550°C (2820°F) where the rule of mixtures predicts the ultimate strength with any degree of accuracy, but it is still higher than the experimentally derived values and the other theoretical predictions utilized in this section. It was mentioned in the previous chapter that this approach assumes that all the fibers are intact just prior to the composite ultimate strength. The rule of mixtures does not account for the brittle nature of the reinforcing fibers and the corresponding variance in the strength of the fibers. As a result, the rule of mixtures assumes ideal conditions, producing optimistic strength values relative to the experimentally derived measurements of the SiC/RBSN composites.

Since the fibers are brittle and exhibit linear elastic behavior with a variance in strength it is more appropriate to apply statistics to determine the

ultimate strength. Curtin's (1993) theory, equation 6.66, incorporates Weibull statistics to address the variance in the strength of the fibers. Data from Tables XX and XXII were used with Curtin's theory. The fiber gage length, L_f, is 25 mm (0.98). The results are presented in Table XXIV and Figure 46. Curtin's theory also produces optimistic values for the ultimate strength. At room temperature to 600°C (1110°F) the theory predicts 9-12% greater or just outside of one standard deviation for the experimental values. At 800°C (1470°F) the experimentally derived values for the ultimate strength of the SiC/RBSN decrease significantly, whereas, Curtin's theory, based on fiber strength data, does not change as much, resulting in a significantly higher prediction. At 1000°C (1830°F) to 1550°C (2820°F) the theory predicts higher strengths relative to the experimentally derived values from 34% over at 1000°C (1830°F) to 15% over at 1550°C (2820°F). Curtin's theory is a significant improvement over the simple rule of mixtures for predicting the ultimate strength of the brittle fiber reinforced SiC/RBSN composite system.

Evans, et al. (1995) tried to predict the ultimate strength of the composite using the rule of mixtures, the fiber bundle strength with Weibull statistics, and with the assumption that influence from the matrix was insignificant. The theory is presented in Equation 6.67. The results are shown in Figure 46 and Table XXIV. The mean fiber strengths and the fiber Weibull moduli were taken from Table XXII. All gage lengths, L_f and L_c, are 25 mm except at room temperature where the composite gage length, L_c, assumed to

be the same as the bundle gage length, is 38 mm. The theory overestimates the ultimate strength of the SiC/RBSN at all temperatures but it shows a similar curve to Curtin's theory. The curves show a reduction in ultimate strength from room temperature to approximately 600°C (1110°F) with a slight increase from 600°C (1110°F) to 800°C (1470°F). The reduction in strength continues from 800°C (1470°F) to 1550°C (2820°F). At room temperature only the rule of mixtures predicts a higher ultimate strength. At temperatures between 1000°C (1830°F) to 1550°C (2820°F) the results are similar to the estimates from Curtin's theory.

Evans (1989) presented a model based on a modified fiber bundle theory. The theory is presented in equation 6.68. The results are presented in Figure 46 and Table XXIV. The required parameters of the fiber bundle strength, σ_{fub}, was solved iteratively using equation 6.69 and the scale parameter, σ_o, was determined using equation 6.70. These results are presented in Tables XXIV and XXV. The area normalizing factor, A_o=1.0 m^2. All gage lengths, L_f and L_c, are set at 25 mm (0.98 in.) except at room temperature where L_c=38 mm (1.5 in.). The theory produces results which are slightly better than Curtin's theory (1993). At room temperature the prediction is 6% greater and within one standard deviation of the experimentally derived data and only 4% over at 600°C (1110°F). At 800°C (1470°F) the theory predicts an increase in the ultimate strength as do most of the other theories reviewed in this section, in contrast to the decrease shown

by the experimentally derived data. At 1400°C (2550°F) the modified fiber bundle theory produces an estimate that is nearly identical to the result from Curtin's theory (1993), but it is 31% greater than the experimentally derived value. Finally, at 1550°C (2820°F) the modified fiber bundle theory results in a value that is again nearly identical to Curtin's theory but 12% higher than the experimentally derived value.

Cao and Thouless (1990) also presented a theory for predicting the ultimate strength for a ceramic composite. It is based on two parameter Weibull statistics as described in the previous chapter. The theory was applied to the SiC/RBSN system with the results presented in Figure 46 and Table XXIV. The same scale parameters, σ_o, calculated for the modified fiber bundle theory of Evans (1989), were used for this theory. The values are presented in Table XXV. The composite gage length, L_c, is set at 38 mm (1.5 in.) for room temperature and 25 mm (0.98 in.) for temperatures greater than room temperature. At room temperature and at 600°C (1110°F), the theory predicted the composite ultimate strength within 2% and 0.3%, respectively. At 800°C (1470°F) the theoretical value was significantly greater than the experimentally measured value for the composite ultimate strength. The theoretical predictions improve again as the temperature increases but it is still significantly overestimating the ultimate strength of the composite. The theoretical prediction is within 3% of the experimentally obtained value at 1550°C (2820°F).

All the theories that were addressed in this section using the treated fiber properties overestimated the ultimate strength of the SiC/RBSN composite. At 800°C (1470°F), the extensive reduction in the ultimate strength may be attributed to oxidation of the fibers initiating prior to the first matrix cracking stress. Bhatt (1992) showed that oxygen accesses the fiber/matrix interface through the matrix porosity approximately between 600°C (1110°F) and 1000°C (1830°F). Above 1000°C (1830°F), the formation of silica at the composite surface effectively seals the porosity. Overall, the slightly lower values of the experimentally obtained ultimate strength measurements for the SiC/RBSN composite may be due to fiber damage incurred during processing of the SiC/RBSN or due to possible surface damage produced upon matrix fracture during the tensile test. The use of graphite sheets in place of the silicon slurry to treat the fibers, as described in the chapter on the specimen configuration, may not have been enough to truly reproduce the processing conditions of the SiC/RBSN. It is possible that the silicon slurry, used as a precursor for the RBSN matrix, damages the fiber surfaces to a greater degree than the graphite sheets under the SiC/RBSN processing conditions. Although by the time the temperature approaches 1500°C (2700°F), the fiber strength degrades rapidly due to grain growth as noted by Bhatt (1992). Bhatt and Hull (1993) showed fairly rapid grain growth in the CVD fibers at temperatures over 1400°C (2550°F). This degradation of intrinsic strength becomes more significant than the strength reduction due to surface damage. As a result, the

predicted composite ultimate tensile strength, based on fiber properties, becomes more accurate when compared with the measured composite ultimate tensile strength. The application of the mean fiber strength and the fiber Weibull modulus does predict the ultimate strength of the composite with reasonable accuracy. Increasing the number of specimens per test should show more accurate results when applying statistics. In addition, a more accurate technique is needed to model the fiber damage due to the processing of the SiC/RBSN composite. Lastly, the mean strengths and Weibull moduli for the fibers were generated by testing individual fibers. Hill and Okoroafor (1995) have observed a reduction in strength of fiber bundles due to inter-fiber friction. This inter-fiber friction may be causing some of the reduction in strength of the experimentally derived composite data relative to the theoretical values derived from individually tested fibers. On an interesting note, Cox, Marshall, and Thouless (1989) found that the fracture of composites is not greatly influenced by the breadth of the fiber strength distribution. Although the theories incorporating the scatter in fiber strength improved the predictions of the composite ultimate strength, the conclusions of Cox, Marshall, and Thouless (1989) reinforces the idea that the lower strength of composites is most likely due to damaged fibers caused by the processing conditions of the composite.

Figure 47 illustrates the ultimate strength as a function of time at high temperatures in air for different temperatures. The curves are similar to the

curves in Figure 24 illustrating the changes in the first matrix cracking stress as a function of time at high temperatures. The ultimate strength drops significantly within the first hour of exposure leading to an insignificant change up to four hours of exposure at 600°C (1110°F) and 1000°C (1830°F). The ultimate strength does not change significantly from zero to four hours of exposure to air at 1400°C (2550°F). Although, it should be noted that only one specimen was tested at each temperature for the four hour tests.

The same phenomena are believed to be responsible for the changes in the ultimate strength of the SiC/RBSN composite as discussed in the section on the first matrix cracking stress. It is believed that the carbon interface between the fibers and the matrix oxidizes within the first hour of exposure. This results in the drop in strength within the first hour of exposure. At 1400°C (2550°F) it believed that the composite was quickly sealed by the formation of silica on the surface of the specimen. As a result, negligible changes were noted for the 1400°C (2550°F) tests up to four hours. Bhatt (1992) did show that at 1200°C (2200°F) and 1400°C (2550°F) oxidation of the RBSN matrix quickly seals the porosity in the matrix, reducing the rate of oxidation of the fiber/matrix interface.

7.1.5 Tensile Modulus of Toughness of SiC/RBSN

The modulus of toughness is determined by numerically integrating the stress/strain curve. The modulus of toughness values for SiC/RBSN are presented in Tables IX and X for oxidizing and inert environments, respectively. The data indicate a 56% drop in the modulus of toughness from 3.2 MJ/m^3 (460 $lb_f \cdot in/in^3$) at 600°C (1110°F) to 1.4 MJ/m^3 (200 $lb_f \cdot in/in^3$) at 800°C (1470°F) in air. A slight increase to 1.5 MJ/m^3 (220 $lb_f \cdot in/in^3$) is observed at 1000°C (1830°F). This is followed by a steady decrease to 1.1 MJ/m^3 (160 $lb_f \cdot in/in^3$) at 1550°C (2820°F). Results of tests conducted in air and nitrogen showed comparable magnitudes in the modulus of toughness indicating negligible environmental effects for these short term tests.

7.2 Enhanced SiC/SiC Composite System

The enhanced SiC/SiC specimens were tensile tested in air from room temperature to 1370°C (2500°F). The resulting mechanical properties are presented in Table XXVI. Stress/strain curves for individual specimens are presented in Figures 48 to 51 to show typical curves. As is the case with the SiC/RBSN composite system described earlier, all the enhanced SiC/SiC specimens exhibited graceful failure. The pseudo-tough behavior or the ability to sustain damage was observed for all the test temperatures from room temperature to 1370°C (2500°C). The extensometer slipped and the output

peaked during the test in Figure 50. The stress/strain curves do show a small linear elastic region that is followed by a relatively large nonlinear region. Most of the curves indicate a second linear region just before the ultimate strength of the composites.

7.2.1 Tensile Modulus of Enhanced SiC/SiC

Figure 52 and Table XXVI show the Young's modulus as a function of temperature in air for the enhanced SiC/SiC composite. The Young's moduli derived from the high temperature tensile tests show a steady degradation as the test temperature was increased from room temperature to 1090°C (2000°F). The experimentally derived modulus increased slightly at 1370°C (2500°F) but it should be noted that only one specimen was tested at that temperature. Figure 52 also shows theoretical values for the Young's modulus using the theories discussed in the last chapter. The theories utilize the moduli of the constituents which are presented in Table XXVII.

The Nicalon fiber moduli, as a function of temperature, were interpolated from data presented by Pysher, et al. (1989). The SiC moduli were interpolated from data presented in Engineering Property Data On Selected Ceramics Volume 2, Carbides (1979). It should be noted that properties for SiC are used to approximate the properties of the matrix in the enhanced SiC/SiC composite.

The volume fraction of the porosity is 10% with respect to the total volume of the enhanced SiC/SiC composite. Using equation 6.43, the porosity volume fraction with respect to the matrix volume, $V_{p,m}$, is determined to be 0.17. Finally, equation 6.42 is used to determine the modulus of the matrix, E_m, from the modulus of the SiC and the porosity in the matrix, $V_{p,m}$. The resulting matrix moduli, E_m, are presented in Table XXVII.

The shear moduli of the fiber and the matrix, G_f and G_m, respectively, are also presented in Table XXVII. These were calculated using equation 6.20 with the simplifying assumption that the constituents are isotropic. The Poisson's ratio, ν, for both constituents is considered to be 0.2 as reported by Hahn and Pandey (1992). The assumption for the Poisson's ratio is noted in Table XXVII also.

It was discussed in the previous chapter that the simplest technique for predicting the modulus of the triaxially woven fiber composite is by modeling it as a laminated composite with each lamina having unidirectional straight fibers. The enhanced SiC/SiC was modeled as a laminated composite using a $[\pm 60/\overline{0}]_S$ architecture. All the fibers in the 0° direction were placed into one ply as the middle ply of the model, with resulting fiber volume fraction $V_f=0.85$. The matrix with porosity makes up the rest of the ply at $V_m=0.15$. The off-axis fibers were divided equally for the ±60° plies resulting in a fiber volume fraction of $V_f=0.2875$ and a matrix volume fraction of $V_m=0.7125$ for

each ply. The information on the plies of the model is also presented in Table XXVIII.

The longitudinal modulus, E_L, of each ply is determined using the rule of mixtures, equation 6.8, and the constituent properties data presented in Table XXVII. The fiber/matrix interfacial shear strength is assumed to be sufficient for adequate load transfer such that both constituents contribute fully to the longitudinal Young's modulus of each ply. The results are presented in Table XXVIII.

The transverse modulus of each ply is determined using the generalized empirical equation of Halpin and Tsai (1969), equation 6.18, and the data presented in Table XXVII. Two limits are considered. As an upper limit a strong bond is assumed, and as a lower limit a frictional fiber/matrix interface is assumed. The fiber modulus is taken as zero with the assumption of the frictional fiber/matrix interface. The results are presented in Table XXVIII.

The longitudinal shear modulus, G_{LT}, of each ply is calculated from the generalized empirical equation of Halpin and Tsai (1969), equation 6.21, and the constituent properties presented in Table XXVII. The same limits, as with the transverse modulus, are considered. For an upper limit a strong fiber/matrix interfacial bond is considered and as a lower limit a frictional fiber/matrix interface is considered. Again, the fiber properties are assumed to be zero for the assumption of the frictional fiber/matrix interface. The results are presented in Table XXVIII.

The Poisson's ratio of each lamina, ν_{LT}, is determined using the rule of mixtures equation 6.24. Since the Poisson's ratio of each of the constituents is assumed to be the same at 0.2, as noted in Table XXVII, the resulting Poisson's ratio of each lamina is 0.2, also.

Lastly, the stiffness properties of each lamina, presented in Table XXIX, are transformed to the longitudinal direction or primary axis of the composite using equation 6.23. The resulting transformed moduli, E_x, for each ply and each limiting condition for the fiber/matrix interface are presented in Table XXIX. The laminae properties are combined, using equation 6.25, to produce a composite longitudinal modulus, E_{cx}, that is presented in Table XXIX and plotted in Figure 52.

It can be observed in Table XXIX and Figure 52 that the assumption of a strong fiber/matrix interface significantly overestimates the longitudinal Young's modulus of the composite. The assumption of a frictional fiber/matrix interface improves the predicted modulus, although, it still overestimates the modulus as observed experimentally. At room temperature the predicted value is almost within one standard deviation of the experimentally derived modulus. It is believed that the longitudinal modulus of each ply in the model contributes to the high magnitude of the calculated modulus, since it does not account for the fiber tow waviness.

In an attempt to improve the accuracy of predicting the modulus of the composite, the theory of Chou and Ishikawa (1989) expanded to triaxially

woven fiber architectures by Yang and Chou (1989) is employed. The composite architecture used in the previously mentioned model with the straight fibers is utilized again. The model consists of five plies with a $[\pm 60/\overline{0}]_S$ fiber architecture. Each ply is considered to be unidirectionally reinforced, but the fibers undulate in the plane defined by the fiber direction and the normal axis to the lamina. An illustration was provided in Figure 11 in the last chapter. The magnitudes of the geometric parameters used in the shape functions of equations 6.26 to 6.28 are noted in Table XXX. The geometic parameters are illustrated in Figures 12 and 13. Since the enhanced SiC/SiC composite specimens in this study consist of five plies, the height of the fiber tow undulations, H, is assumed to be one fifth of the overall composite thickness, or 610 μm (24 mils). The length of each fiber undulation, 2L, was measured using an optical microscope. The longitudinal fiber tow undulation length was measured to be $2L_{0°}$=1.57 mm (62 mils) and the off-axis (±60°) fiber tow undulation lengths were $2L_{+60°}=2L_{-60°}$=2.15 mm (85 mils).

Equations 6.26 to 6.41 with the above mentioned geometric parameters are used to solve for the longitudinal, transverse, and shear moduli of each of the plies. Equation 6.31 shows that the transverse modulus, E_T, of each ply is the same as the transverse modulus used with basic composite theory for modeling unidirectional straight fiber laminae. As with the previous model the limits presented by a strong bond and a frictional bond at the fiber/matrix interface are considered. Equation 6.18 is used to calculate the lamina

transverse modulus for the case of a strong fiber/matrix interfaces, whereas, equation 6.19 is used to calculate the lamina transverse modulus with a frictional fiber/matrix interface. The shear moduli in equation 6.33, $G_{TT'}$ and G_{LT}, are assumed to be equal for this study. As a result, equation 6.33 simplifies to the shear modulus used in basic composite theory for modeling unidirectional straight fiber laminae. Equation 6.21 is used to determine the shear stiffness of each laminate. The same assumptions are used as previously for the strong and frictional fiber/matrix interfaces. The integrals of equations 6.36 and 6.37 were solved numerically using the Romberg method. The resulting moduli are transformed to the longitudinal axis of the laminated composite, using equation 6.23. The stiffness of each ply, in the longitudinal direction of the laminated composite, is shown in Table XXX. Finally, equation 6.25 is used to calculate the net stiffness of the composite. The results are shown in Table XXX and Figure 52.

It can be observed in Figure 52 that the assumption of a strong fiber/matrix interface produces similar predictions for the model using straight fibers and the model accounting for the fiber tow undulations. This is due to the similar moduli of the fibers and the matrix. On the other hand, the model that accounts for the fiber undulations using a frictional fiber matrix interface produces values that are considerably closer to the experimentally derived values of the Young's modulus. At room temperature the model accounting for the fiber tow undulations and assuming a frictional fiber/matrix interface

predicts the Young's modulus within one standard deviation of the experimentally derived value. At temperatures above room temperature the model overestimates the Young's modulus relative to the experimentally derived values. Some of the discrepancy may be due to the fact that the matrix is assumed to be primarily SiC. The added proprietary materials in the enhanced SiC/SiC composite may reduce the actual matrix modulus relative to SiC. Variations in the actual total fiber volume fraction may be another possible source for the discrepancy. Dadkhah, et al. (1995) have suggested that variations of approximately 10% are commonplace for triaxially braided fiber reinforced composites.

It was noted at the beginning of this section that most of the stress/strain curves for the enhanced SiC/SiC exhibited a linear region just prior to the ultimate strength. This is the same behavior observed with the SiC/RBSN composite system in this study. The secondary linear region is attributed to the fibers carrying the load, with negligible support from the matrix material. The magnitudes of the secondary moduli are presented in Table XXXI. It is assumed that the secondary modulus is controlled by the longitudinal fibers with negligible influence from the off-axis ($\pm 60°$) fibers and the matrix. In addition, the longitudinal fibers are assumed to be straight. The rule of mixtures, equation 6.22, is applied in attempt to model the secondary modulus of the composite. The results are presented in Table XXXI. Similar to the analysis of the SiC/RBSN composite system, the rule of mixtures

significantly overestimates the secondary modulus of the enhanced SiC/SiC system. It is possible that a significant number of fibers may have failed prior to the ultimate strength of the composite due to damage inflicted during the braiding of the fibers and the processing of the composite. Other influences may be that the fibers are not completely straight and/or that not all the fibers may be loaded evenly due to poor load transfer from the extensively damaged matrix.

7.2.2 Ultimate Tensile Strength of Enhanced SiC/SiC

The experimentally derived mean ultimate tensile strengths with one standard deviation of the enhanced SiC/SiC composite are presented in Table XXXIII and Figure 53. The data indicate little change in the ultimate strength as a function of temperature between room temperature and approximately 1090°C (2000°F). A drop in strength occurred at 1370°C (2500°F).

The ultimate strength of the enhanced SiC/SiC is controlled by the fiber properties, as is the case with the SiC/RBSN used in this study. In particular, the fibers oriented in the longitudinal or primary direction of the composite carry the load near the ultimate strength of the composite. Dadkhah, et al. (1995) have concluded that the off-axis fibers contribute very little to the ultimate strength of a triaxially woven fiber reinforced composite. The fiber

orientation of the enhanced SiC/SiC in this study falls in the range studied by Dadkhah and associates (1995).

The strength properties of Nicalon fiber are presented in Table XXXII. The ultimate strengths of the Nicalon fibers are interpolated from the strength values presented by Pysher and associates (1989). The fibers tested by Pysher, et al. (1989) had a gage length, L_f, of 75 mm (3.0 in.) and an average diameter of 13 μm (0.51 mils). The Nicalon fiber Weibull modulus, m, is taken from the work of Prewo (1986) at 4.2 and, for this work, assumed to be constant for all temperatures.

The theoretical composite ultimate strengths for the enhanced SiC/SiC are presented in Table XXXIII and Figure 53. The theoretical ultimate strengths of the composite are calculated using the various theories presented in the previous chapter and used for analyzing the SiC/RBSN composite system in this study.

The rule of mixtures, equation 6.65, provides the simplest analysis for predicting the composite ultimate strength. The 0° fiber volume fraction of 0.17 is assumed to be the load bearing constituent as the applied stress approaches the ultimate strength of the composite. It is assumed that the off-axis fibers and the matrix do not bear any part of the applied load near the ultimate strength of the composite. The single value of the mean ultimate strength of the fiber is used for this theory. Unfortunately, the results indicate that the rule of mixtures significantly overestimates the ultimate strength of

the enhanced SiC/SiC composite just as it did with the SiC/RBSN composite system. The theory overestimates the composite ultimate strength by 129% at room temperature, but improves slightly at higher temperatures where it still overestimates the ultimate strength by 41% at 1370°C (2500°F). Dadkhah, et al. (1995) observed similar results of overestimating the composite ultimate strength. They concluded that the stress concentrations caused by the fiber architecture only causes an approximate drop of 10% in strength, whereas, the damage caused by the braiding process is the most likely cause for the significant drop in strength.

In an attempt to account for the brittle nature of the fibers and their corresponding variance in strength, Weibull statistics are incorporated into some theories for predicting the ultimate strength of ceramic composites. Curtin's (1993) theory, equation 6.66, incorporates the rule of mixtures and Weibull statistics of the fibers. It was noted above that the fiber Weibull modulus, m, is assumed to be constant at 4.2 with respect to temperature. The value for the Weibull modulus of Nicalon SiC fiber was taken from the work of Prewo (1986). An approximate value of 20 MPa (2.9 ksi) is assumed for the fiber/matrix interfacial shear stress, τ. The value for the fiber/matrix interfacial shear stress was taken from the work of Inghels and Lamon (1991) with Nicalon SiC fiber reinforced CVI SiC matrix composites. The mean ultimate strength of the fiber as a function of temperature, used for this theory, is presented in Table XXXII. Lastly, the fiber gage length, L_f, is 75 mm

(3.0 in.) and the fiber radius, R, is 7 μm (0.27 mils). With the given variables Curtin's theory overestimates the composite ultimate strength by a wide margin. The theory is highly dependent on the Weibull modulus. It is possible that the low value for the Weibull modulus of 4.2 indicates excessive scatter in the fiber strength making it difficult to predict the ultimate strength of the composite by this method. The ultimate strength of the fiber may be significantly lower in the composite than the fibers in an as-received condition. The damage may be due to the braiding process and the matrix processing conditions. It is possible that the fiber/matrix interfacial shear strength is lower than the assumed value of 20 MPa (2.9 ksi).

The fiber bundle theory by Evans, et al. (1995), Equation 6.67, is applied to predict the ultimate strength of the composite using the rule of mixtures, the fiber bundle strength with Weibull statistics, and with the assumption that influence from the matrix was insignificant. The results are shown in Figure 53 and Table XXXIII. The mean fiber strengths and the fiber Weibull modulus were taken from Table XXXII. The fiber gage length, L_f, is 75 mm (3.0 in.) from the work of Pysher and associates (1989) from whose work the fiber strength properties were derived. The composite gage length, L_c, is 25 mm (1.0 in.) for all high temperature tests and 140 mm (5.5 in.) for the room temperature tests. The theory overestimates the ultimate strength of the enhanced SiC/SiC at all temperatures. The theory overestimates the measured composite ultimate strength by 44% at room temperature. At 815°C (1500°F)

the estimate is 89% greater than the experimental value for the composite ultimate strength. At 1370°C (2500°F) the predicted magnitude for the composite ultimate strength is 44% greater than the experimentally derived value. Evans' theory produces nearly identical results to the results obtained using the rule of mixtures between 815°C (1500°F) and 1370°C (2500°F).

The theory of Cao and Thouless (1990) was also applied to the analysis of the enhanced SiC/SiC composite. It is based on two parameter Weibull statistics as described in the previous chapter. The results presented in Figure 53 and Table XXXIII. The scale parameters, σ_o, were calculated as described with the modified fiber bundle theory of Evans (1989). The scale parameter values and other intermediate variables are defined in Table XXXIV. The composite gage length, L_c, is set at 140 mm (5.5 in.) for room temperature and 25 mm (1.0 in.) for temperatures greater than room temperature. At room temperature and at 815°C (1500°F) the theory overestimated the composite ultimate strength by 22% and 16%, respectively. The theoretical predictions improve slightly as the temperature increases. At temperatures of 1090°C (2000°F) and 1370°C (2500°F) Cao's and Thouless' theory underestimates the ultimate strength of the composite by 7% and 14%, respectively. Nevertheless, this approach to calculating ultimate strengths lead to predictions closest to the measurements.

7.2.3 Tensile Modulus of Toughness of Enhanced SiC/SiC

The modulus of toughness values for enhanced SiC/SiC are presented in Table XXVI. The data indicate increases in the modulus of toughness from 0.3 MJ/m^3 (44 $lb_f \cdot in/in^3$) at room temperature to 0.9 MJ/m^3 (130 $lb_f \cdot in/in^3$) at 1090°C (2000°F) in air. A decrease to 0.7 MJ/m^3 (102 $lb_f \cdot in/in^3$) in the modulus of toughness is noted as the test temperature approaches 1370°C (2500°F).

Table IX: High Temperature Mechanical Tensile Properties of SiC/RBSN Composites in Air.

Specimen No.	T (°C)	E_c (GPa)	σ_y (MPa)	ε_y (%)	E_{c2} (GPa)	σ_{cu} (MPa)	ε_{cu} (%)	U_T (MJ/m^3)
572-2	22	205	229	0.12		637	0.92	
572-3	22					553		
572-4	22	191	153	0.08				
mean	**22**	**198**	**191**	**0.10**		**595**	**0.92**	
std. dev.								
884-1	600	165	210	0.13	85	594	1.07	3.5
884-2	600	166	229	0.14	83	620	1.07	3.2
884-3	600	160	216	0.14		486	1.07	2.8
mean	**600**	**163**	**218**	**0.14**	**84**	**567**	**1.07**	**3.2**
std. dev.		3	10	0.01		71	0.00	0.3
931-2	800	156	179	0.12	62	350	0.62	1.8
931-3	800	138	127	0.09	62	316	0.52	1.1
mean	**800**	**147**	**153**	**0.11**	**62**	**333**	**0.57**	**1.4**
std. dev.								
907-1	1000	151	173	0.11	79	431	0.65	1.3
907-2	1000	136	147	0.11	70	372	0.64	1.7
907-3	1000	148	165	0.11				
mean	**1000**	**145**	**161**	**0.11**	**74**	**401**	**0.65**	**1.5**
std. dev.		8	13	0.00				
854-1	1400	146	143	0.09	19	255	0.63	1.2
854-2	1400	148	179	0.11	17	246	0.62	1.2
854-3	1400	122	139	0.11	25	253	0.76	1.6
mean	**1400**	**138**	**154**	**0.10**	**20**	**251**	**0.67**	**1.3**
std. dev.		14	22	0.01	4	5	0.08	0.2
781-1	1550	87	165	0.19	17	230	0.68	1.1
781-2	1550	106	110	0.11	19	229	0.61	1.0
781-3	1550	68	57	0.08	17	221	0.71	1.1
mean	**1550**	**87**	**111**	**0.13**	**18**	**226**	**0.67**	**1.1**
std. dev.		19	54	0.06	1	5	0.05	0.1

T - test temperature
E_c - Young's modulus of composite
σ_y - first matrix cracking stress
ε_y - strain at first matrix cracking stress
E_{c2} - secondary modulus of composite near ultimate strength
σ_{cu} - ultimate strength of composite
ε_{cu} - strain at the ultimate strength of composite
U_T - modulus of toughness

Table X: High Temperature Mechanical Tensile Properties of SiC/RBSN Composites in Nitrogen.

Specimen No.	T (°C)	E_c (GPa)	σ_y (MPa)	ε_y (%)	E_{c2} (GPa)	σ_{cu} (MPa)	ε_{cu} (%)	U_T (MJ/m^3)
830-2	1000	163	149	0.09	52	381	0.95	1.5
837-2	1000	172	140	0.08		342	0.85	
mean	**1000**	**167**	**144**	**0.09**	**52**	**362**	**0.90**	**1.5**
std. dev.								
784-3	1400	117	88	0.08	27	241	0.59	1.0
830-3	1400	120	122	0.10	12	237	0.85	1.4
845-3	1400	134	112	0.08	15	234	0.72	1.4
mean	**1400**	**123**	**107**	**0.09**	**18**	**237**	**0.72**	**1.2**
std. dev.		9	17	0.01	8	3	0.13	0.2

Table XI: High Temperature Mechanical Tensile Properties of SiC/RBSN Composites in Air With One Hour Exposure Prior to Test Commencement.

Specimen No.	T (°C)	E_c (GPa)	σ_y (MPa)	ε_y (%)	E_{c2} (GPa)	σ_{cu} (MPa)	ε_{cu} (%)
851-1	600	152	201	0.13	66	438	1.05
851-2	600	143	180	0.12	84	511	0.95
851-3	600	183	158	0.09		381	0.92
mean	**600**	**159**	**180**	**0.11**	**75**	**443**	**0.97**
std. dev.		21	21	0.02		65	0.07
937-1	1000	156	205	0.12		422	1.07
937-2	1000	164	163	0.10		372	1.08
937-3	1000	150	74	0.05		268	0.48
mean	**1000**	**156**	**147**	**0.09**		**354**	**0.88**
std. dev.		7	67	0.04		79	0.34
826-1	1400	135	149	0.11	14	230	0.60
826-2	1400	88	135	0.15	24	222	0.55
826-3	1400	118	128	0.11			
mean	**1400**	**113**	**137**	**0.12**	**19**	**226**	**0.58**
std. dev.		24	10	0.02			
821-1	1550	98	87	0.08	142	189	0.25
821-2	1550	161	97	0.06		203	1.01
mean	**1550**	**130**	**92**	**0.07**	**142**	**196**	**0.63**
std. dev.						10	0.54

Table XII: High Temperature Mechanical Tensile Properties of SiC/RBSN Composites in Air With Four Hours Exposure Prior to Test Commencement.

Specimen No.	T (°C)	E_c (GPa)	σ_y (MPa)	ε_y (%)	E_{c2} (GPa)	σ_{cu} (MPa)	ε_{cu} (%)
837-1	600	180	175	0.10		389	+1.06
841-1	1400	141	136	0.05	27	275	0.12
845-1	1550	203	90	0.04	134	177	0.28

Table XIII: High Temperature Mechanical Tensile Properties of SiC/RBSN Composites Held Under Constant Load at 1400°C in Air Until Failure.

Specimen No.	E_c (GPa)	σ_y (MPa)	ε_y (%)	σ_{hold} (MPa)	ε_{hold} (%)	σ_{hold}/σ_y	Time to Failure (Hrs.)
849-1	130	165	0.12	175	0.16	1.06	0.4
849-2	128	173	0.14	186	0.15	1.08	0.1
849-3	144	161	0.11	181	0.15	1.12	0.7
mean	**134**	**166**	**0.12**	**180**	**0.15**	**1.09**	**0.4**
std. dev.	9	6	0.02	6	0.01	0.03	0.3
852-1	149			133	0.09	~0.80	0.6
852-2	127			136	0.11	~0.80	0.6
852-3	127			135	0.11	~0.80	4.0
mean	**134**			**135**	**0.10**		**1.7**
std. dev.	13			1	0.01		2.0

σ_{hold} - applied stress
ε_{hold} - strain at applied stress

Table XIV: Tensile Young's Modulus of SiC/RBSN as a Function of Temperature In Air and Nitrogen.

T (°C)	[1]Measured modulus (GPa)		Modulus by rule of mixtures (GPa)	
	environment: air	environment: nitrogen	environment: air	[2]environment: nitrogen
22	198±10		183	
600	163±3		171	
800	147±13		167	
1000	145±8	167±6	163	157
1400	138±14	124±9	155	155
1550	87±19		152	

1. mean and one standard deviation values from tensile tests
2. using fiber properties in air

Table XV: CVD SiC Fiber Moduli as a Function of Temperature in Air and Monolithic RBSN and RBSN Matrix Moduli as a Function of Temperature in Air and Nitrogen.

	Environment: air			Environment: nitrogen	
T (°C)	E_f (GPa)	E_{RBSN} (GPa)	E_m (GPa)	E_{RBSN} (GPa)	E_m (GPa)
22	391	110	112		
600	379	98*	100		
800	375	94*	96		
1000	371	90	92	82	83
1400	364	82*	83	82	83

E_f - fiber modulus
E_{RBSN} - monolithic RBSN modulus
E_m - calculated matrix modulus as a function of E_{RBSN} and porosity
* calculated values using linear interpolation or extrapolation

Table XVI: Porosity of Monolithic RBSN and SiC/RBSN Composites Determined Using ASTM Standard Designation C 20-74.

Results for monolithic RBSN

W (g)	W_b (g)	W_s (g)	v (cm^3)	v_{op} (cm^3)	v_{ip} (cm^3)	v_{cp} (cm^3)	V_p
1.4461	0.9733	1.6025	0.6292	0.1564	0.4728	0.0209	0.282
0.8773	0.6043	1.0092	0.4049	0.1319	0.2730	0.0000	0.326
0.8810	0.6006	1.0099	0.4093	0.1289	0.2804	0.0051	0.327
0.8737	0.6003	1.0089	0.4086	0.1352	0.2734	0.0004	0.332
0.8647	0.5894	0.9963	0.4069	0.1316	0.2753	0.0051	0.336
0.8392	0.5733	0.9780	0.4047	0.1388	0.2659	0.0036	0.352

panel no. 784 $^{1,2}V_p = 0.33 \pm 0.02$

Results for SiC/RBSN composite

W (g)	W_b (g)	W_s (g)	v (cm^3)	v_{op} (cm^3)	v_{ip} (cm^3)	V_f	v_{cp} (cm^3)	V_p
0.9646	0.6550	1.0355	0.3805	0.0709	0.3096	0.24	0.0025	0.193
0.4382	0.2970	0.4826	0.1856	0.0444	0.1412	0.24	0.0015	0.247
0.4428	0.2989	0.4871	0.1882	0.0443	0.1439	0.24	0.0027	0.250
0.4493	0.3020	0.4918	0.1898	0.0425	0.1473	0.24	0.0040	0.245
0.4351	0.2904	0.4823	0.1919	0.0472	0.1447	0.24	0.0059	0.276
0.4428	0.3003	0.4858	0.1855	0.0430	0.1425	0.24	0.0013	0.239

panel no. 949 $V_f = 0.24$ $^{1,2}V_p = 0.24 \pm 0.03$

W - dry weight
W_b - buoyant or suspended weight in water
W_s - saturated weight with water
v - total volume, including porosity
v_{op} - volume of open porosity
v_{ip} - volume of the impervious portion, includes closed porosity and ceramic material
V_f - fiber volume fraction
v_{cp} - volume of closed porosity
V_p - porosity volume fraction
1. mean value
2. variance is one standard deviation

Table XVII: SiC/RBSN Measured and Predicted Secondary Tensile Moduli Near the Composite Ultimate Strength as a Function of Temperature in Air and Nitrogen.

T(°C)	environment: air measured E_{c2} (GPa)	environment: nitrogen measured E_{c2} (GPa)	environment: air theoretical by rule of mixtures E_{c2} (GPa)
22			101
600	84		98
800	62		97
1000	74	52	96
1400	20	18	94

Table XVIII: Measured Secondary Moduli, Composite Stresses, Fiber Stresses, and Probability of Fiber Failure at Initiation of Secondary Modulus Near the SiC/RBSN Composite Ultimate Strength as a Function of Temperature in Air.

Specimen no.	T (°C)	E_{c2} (GPa)	σ_c (MPa) at beginning of E_{c2}	σ_f (GPa) at beginning of E_{c2}	$^1P_f(\sigma_f)$
884-1	600	85	287	1.11	
884-2	600	83	312	1.21	
mean	**600**	**84**	**300**	**1.16**	**7.6E-05**
931-2	800	62	246	0.95	
931-3	800	62	258	1.00	
mean	**800**	**62**	**252**	**0.97**	**1.5E-06**
907-1	1000	79	275	1.06	
907-2	1000	70	257	0.99	
mean	**1000**	**75**	**266**	**1.03**	**5.3E-04**
854-1	1400	19	207	0.80	
854-2	1400	17	211	0.82	
854-3	1400	25	198	0.76	
mean	**1400**	**20**	**205**	**0.79**	**2.0E-04**
781-1	1550	17	195	0.75	
781-2	1550	19	186	0.72	
781-3	1550	17	182	0.70	
mean	**1550**	**18**	**188**	**0.73**	**5.5E-04**

σ_c - composite stress
σ_f - calculated fiber stress as a function of composite stress
$P_f(\sigma_f)$ - probability of fiber failure under a stress of σ_f
1. based on Weibull statistics

Table XIX: Measured Secondary Moduli, Composite Stresses, Fiber Stresses, and Probability of Fiber Failure at Initiation of Secondary Modulus Near the SiC/RBSN Composite Ultimate Strength as a Function of Temperature in Nitrogen.

Specimen no.	T (°C)	E_{c2} (GPa)	σ_c (MPa) at beginning of E_{c2}	σ_f (GPa) at beginning of E_{c2}	$^{1,2}P_f(\sigma_f)$
830-2	**1000**	**52**	**339**	**1.31**	**4.0E-03**
784-3	1400	27	230	0.89	
830-3	1400	12	180	0.70	
845-3	1400	15	180	0.70	
mean	**1400**	**18**	**197**	**0.76**	**1.2E-04**

1. based on Weibull statistics
2. derived from fiber property data generated from high temperature tensile tests in air.

Table XX. Measured Matrix Crack Spacing and Resulting Interfacial Shear Stress for SiC/RBSN Composites as a Function of Temperature and Envirnment.

environment: air

T (°C)	x (mm)	τ (MPa)	τ_{cr} (MPa)
22	2.0±0.6	7.1	834
600	1.6±0.8	11.4	734
800	1.5±0.5	8.9	728
1000	1.6±0.9	8.4	540
1400	3.5±1.3	3.5	338
1550	2.2±1.0	6.2	241

environment: nitrogen

T (°C)	x (mm)	τ (MPa)	τ_{cr} (MPa)
1000	0.7±0.3	13.6	501
1400	1.0±0.5	9.6	338

x - mean matrix crack spacing and one standard deviation

τ - mean fiber/matrix interfacial shear strength as a function of the mean matrix crack spacing

τ_{cr} - critical fiber/matrix interfacial shear strength below which matrix toughening occurs

Table XXI. Experimentally Determined and Theoretically Predicted First Matrix Cracking Stress Values for SiC/RBSN Composites

environment: air

T (°C)	experimental (MPa)	ACK (MPa)	ACK, $G_{II}=\gamma_m$ (MPa)	MC+M (MPa)	ACK, f(CTE) (MPa)	MC+M, f(CTE) (MPa)
22	191±54	162	608	129	315	282
600	218±10	194	617	154	269	229
800	153±36	180	617	143	230	193
1000	161±13	178	619	142	203	166
1400	154±22	137	622	109	113	85
1550	111±55	166	627	132	124	90

environment: nitrogen

T (°C)	experimental (MPa)	ACK (MPa)	ACK, $G_{II}=\gamma_m$ (MPa)	MC+M (MPa)	ACK, f(CTE) (MPa)	MC+M, f(CTE) (MPa)
1000	144±6	217	642	172	242	197
1400	107±17	191	628	151	167	127

experimental - mean first matrix cracking stress and one standard deviation derived from tensile tests

ACK - theory from Aveston, Cooper, & Kelly with frictional fiber/matrix interface

ACK, $G_{II}=\gamma_m$ - theory from Aveston, Cooper, & Kelly with a weakly bonded interface

MC+M - theory of Marshall and Cox combined with theory of McCartney

ACK, f(CTE) - ACK theory incorporating residual stress due to fiber/matrix CTE mismatch

MC+M, f(CTE) - theory of MC+M incorporating residual stress due to fiber/matrix CTE mismatch

Table XXII: The Ultimate Strength, Mean Ultimate Strength, Weibull Modulus, and Weibull Characteristic Strength as a Function of Temperature of CVD SiC Fibers.

A. Condition: As Received

n	22°C, air L_f=25 mm σ_{fu} (GPa)	600°C, air L_f=25 mm σ_{fu} (GPa)	800°C, air L_f=25 mm σ_{fu} (GPa)	1000°C, air L_f=25 mm σ_{fu} (GPa)	1200°C, air L_f=25 mm σ_{fu} (GPa)	1400°C, air L_f=25 mm σ_{fu} (GPa)	1550°C, air L_f=25 mm σ_{fu} (GPa)
1	4.10	3.10	3.56	3.11	2.29	1.68	1.20
2	4.10	3.07	3.30	3.01	2.28	1.65	1.20
3	4.03	3.04	3.09	2.97	2.27	1.64	1.18
4	3.90	2.57	2.45	2.91	2.08	1.59	1.17
5	3.71	2.55	2.11	2.42	1.91	1.58	0.96
6	3.68					1.57	
7	3.66					1.57	
8	3.54					1.55	
9	3.40					1.55	
10	3.07					1.53	
mean σ_{fu} (GPa) =	**3.70**	**2.90**	**2.90**	**2.88**	**2.20**	**1.59**	**1.14**
standard deviation	0.33	0.28	0.60	0.27	0.17	0.05	0.10
*Weibull modulus, m =	12.6	10.4	4.6	13.0	14.4	28.7	15.2
5% bound for Weibull modulus	8.1	5.3	2.3	6.6	7.3	18.4	7.7
95% bound for Weibull modulus	19.9	22.0	9.7	27.5	30.4	45.5	32.2
*characteristic strength, σ_θ (GPa) =	3.84	2.96	3.1	2.96	2.22	1.61	1.17

B. Condition: Treated to processing conditions of SiC/RBSN

n	22°C, air L_f=25 mm σ_{fu} (GPa)	600°C, air L_f=25 mm σ_{fu} (GPa)	800°C, air L_f=25 mm σ_{fu} (GPa)	1000°C, air L_f=25 mm σ_{fu} (GPa)	1200°C, air L_f=25 mm σ_{fu} (GPa)	1400°C, air L_f=25 mm σ_{fu} (GPa)	1550°C, air L_f=25 mm σ_{fu} (GPa)
1	3.73	3.46	3.51	2.69	2.06	1.73	1.24
2	3.59	3.40	3.26	2.65	2.06	1.72	1.22
3	3.45	3.22	3.21	2.49	1.94	1.71	1.22
4	3.01	2.82	3.03	2.34	1.92	1.56	1.16
5	2.88	2.76	2.89	1.92	1.80	1.35	1.01
mean σ_{fu} (GPa) =	**3.33**	**3.13**	**3.18**	**2.42**	**1.96**	**1.61**	**1.17**
standard deviation	0.37	0.33	0.24	0.31	0.11	0.16	0.10
*Weibull modulus, m =	8.6	9.2	11.1	8.4	17.2	11.5	14.9
5% bound for Weibull modulus	4.3	4.7	5.6	4.2	8.7	5.8	7.5
95% bound for Weibull modulus	18.1	19.5	23.6	17.7	36.4	24.2	31.5
*characteristic strength, σ_θ (GPa) =	3.45	3.24	3.26	2.52	1.99	1.66	1.2

*Unbiased values derived by using maximum likelihood method with probability estimator $P=(n-0.5)/n_{tot}$ as per ASTM standard designation C 1239-94a

n - rank of the specimen data point

L_f - specimen gage length

Table XXIII: The Probability of Failure at a Given Stress for Treated CVD SiC Fibers as a Function of Temperature.

T (°C)	m	σ_θ (GPa)	$^1\sigma_f$ (GPa)	P_{fu}
22	8.6	3.45		
600	9.2	3.24	1.16	7.9E-05
800	11.1	3.26	0.97	1.4E-06
1000	8.4	2.52	1.03	5.4E-04
1400	11.5	1.66	0.79	2.0E-04
1550	14.9	1.20	0.73	6.1E-04

T (°C)	m	σ_θ (GPa)	$^2\sigma_f$ (GPa)	P_{fu}
1000	8.4	2.52	1.31	4.1E-03
1400	11.5	1.66	0.76	1.3E-04

m - Weibull modulus, by maximum likelihood method
σ_θ - Weibull characteristic strength
σ_f - fiber stress at initiation of secondary composite modulus, E_{c2} of SiC/RBSN
P_{fu} - probability of fiber failure at σ_f from the Weibull cumulative distribution function
1. fiber stress in composite tested in air
2. fiber stress in composite tested in nitrogen

Table XXIV. The Experimental and Theoretical Ultimate Tensile Strength of SiC/RBSN as a Function of Temperature in Air and Nitrogen.

envirnment: air

T (°C)	experimental (MPa)	ROM (MPa)	Curtin (MPa)	Evans 1995 (MPa)	Evans 1989 (MPa)	Cao & Thouless (MPa)
22	595±60	862	663	735	630	608
600	607±18	811	663	697	634	605
800	333±24	824	672	743	679	658
1000	372±59	627	506	517	466	445
1400	251±5	417	335	357	328	310
1550	226±5	303	265	266	252	233

envirnment: nitrogen*

T (°C)	experimental (MPa)	ROM (MPa)	Curtin (MPa)	Evans 1995 (MPa)	Evans 1989 (MPa)	Cao & Thouless (MPa)
1000	362±28	627	506	556	466	445
1400	237±4	417	335	382	328	310

experimental - mean and one standard deviation values from tensile tests
ROM - rule of mixtures
Curtin - Curtin's theory incorporating rule of mixtures and Weibull statistics with L_f=25 mm
Evans 1995 - Evans' theory using fiber bundle theory with no matrix material with L_f=L_c=25 mm except L_c=38 mm at room temperature
Evans 1989 - Evans' theory based on a modified fiber bundle theory
Cao & Thouless - Theory incorporating rule of mixtures and Weibull statistics
* Theoretical results using fiber properties in air

Table XXV. Theoretical Ultimate Strength of SiC/RBSN Using the Modified Fiber Bundle Theory of Evans (1989) with Intermediate Results as a Function of Temperature in Air.

T (°C)	σ_{cu} (MPa)	σ_{fub} (GPa)	σ_o (MPa)
22	625	2.70	934
600	631	2.70	955
800	655	2.76	1190
1000	478	2.07	658
1400	342	1.43	623
1550	263	1.08	563

σ_{cu} - composite ultimate strength based on Evans' theory using a modified fiber bundle theory
σ_{fub} - fiber bundle strength
σ_o - scale parameter
$L_f=L_c=25$ mm except $L_c=38$ mm at room temperature
$A_o=1$ m^2

Table XXVI: High Temperature Mechanical Tensile Properties of Enhanced SiC/SiC Composites in Air.

Specimen No.	T (°C)	E_c (GPa)	σ_y (MPa)	ε_y (%)	E_{c2} (GPa)	σ_{cu} (MPa)	ε_{cu} (%)
1	24	122	23	0.02	19	139	0.38
2	24		33			151	0.40
3	24	146	16	0.01	16	133	0.38
mean	**24**	**134**	**24**	**0.02**	**18**	**141**	**0.38**
std. dev.			9			9	0.01
4	815	76	50	0.07	13	156	0.59
5	815	90	41	0.04	15	176	0.52
6	815	88	22	0.02	18	155	0.43
mean	**815**	**84**	**38**	**0.04**	**15**	**162**	**0.52**
std. dev.		8	14	0.02	3	12	0.08
7	1090	51	22	0.05		180	1.08
8	1090	50	104	0.21		157	1.13
9	1090	44	122	0.29	13	171	0.63
mean	**1090**	**48**	**83**	**0.18**	**13**	**169**	**0.94**
std. dev.		4	54	0.12		12	0.28
11	**1370**	**88**	**46**	**0.06**	**5**	**121**	**0.70**

Table XXVII: Nicalon SiC Fiber, Monolithic SiC, and SiC Matrix Moduli as a Function of Temperature in Air.

T (°C)	E_f (GPa)	E_{SiC} (GPa)	E_m (GPa)	G_f (GPa)	G_m (GPa)
24	190	400	243	79.2	101.1
815	180	386	234	75	97.5
1090	170	381	231	70.8	96.3
1370	100	375	227	41.7	94.8

E_f - fiber modulus
E_{SiC} - monolithic SiC modulus
E_m - calculated matrix modulus as a function of E_{SiC} and porosity
G_f - calculated fiber sheer modulus assuming isotropy with ν_f=0.2
G_m - calculated matrix sheer modulus assuming isotropy with ν_m=0.2

Table XXVIII: Lamina Properties Using the Model with Straight Unidirectional Fibers and $[\pm 60/\bar{0}]_S$ Composite Architecture as a Function of Temperature in Air for Enhanced SiC/SiC.

0° ply, V_f=0.85, V_m=0.15, $V_{p,m}$=0.167

		Halpin-Tsai			
T (°C)	rule of mixtures E_L (GPa)	debonded interface E_T (GPa)	bonded interface E_T (GPa)	debonded interface G_{LT} (GPa)	bonded interface G_{LT} (GPa)
24	198	26	197	8	82
815	188	25	188	8	78
1090	179	24	179	8	74
1370	119	24	116	8	48

+60° ply, V_f=0.2875, V_m=0.7125, $V_{p,m}$=0.167

		Halpin-Tsai			
T (°C)	rule of mixtures E_L (GPa)	debonded interface E_T (GPa)	bonded interface E_T (GPa)	debonded interface G_{LT} (GPa)	bonded interface G_{LT} (GPa)
24	228	151	227	56	94
815	219	146	218	54	91
1090	214	144	212	53	88
1370	191	142	185	52	76

-60° ply, V_f=0.2875, V_m=0.7125, $V_{p,m}$=0.167

		Halpin-Tsai			
T (°C)	rule of mixtures E_L (GPa)	debonded interface E_T (GPa)	bonded interface E_T (GPa)	debonded interface G_{LT} (GPa)	bonded interface G_{LT} (GPa)
24	228	151	227	56	94
815	219	146	218	54	91
1090	214	144	212	53	88
1370	191	142	185	52	76

V_f - fiber volume fraction
V_m - matrix volume fraction (includes porosity)
$V_{p,m}$ - porosity volume fraction with respect to matrix volume
T - test temperature
E_L - longitudinal modulus
E_T - transverse modulus
G_{LT} - longitudinal sheer modulus

Table XXIX: Enhanced SiC/SiC Lamina and Composite Tensile Moduli in the Composite Longitudinal Direction Using the Model with Straight Unidirectional Fibers and $[\pm 60/\bar{0}]_S$ Composite Architecture as a Function of Temperature in Air.

	0° ply		+60° ply		-60° ply		composite	
	interface		interface		interface		interface	
	bonded	debonded	bonded	debonded	bonded	debonded	bonded	debonded
T (°C)	E_x (GPa)	E_x (GPa)	E_x (GPa)	E_x (GPa)	E_x (GPa)	E_x (GPa)	E_{cx} (GPa)	E_{cx} (GPa)
24	198	198	226	143	226	143	221	154
815	188	188	217	138	217	138	212	148
1090	179	179	212	136	212	136	206	144
1370	119	119	184	134	184	134	171	131

E_x - laminate tensile modulus in longitudinal direction of composite specimen
E_{cx} - composite longitudinal tensile modulus

Table XXX: Enhanced SiC/SiC Lamina and Composite Tensile Moduli in the Composite Longitudinal Direction Using the Model with Undulating Unidirectional Fibers and $[\pm 60/\bar{0}]_S$ Composite Architecture as a Function of Temperature in Air.

	0° ply		+60° ply		-60° ply		composite	
	interface		interface		interface		interface	
	bonded	debonded	bonded	debonded	bonded	debonded	bonded	debonded
T (°C)	E_x (GPa)	E_x (GPa)	E_x (GPa)	E_x (GPa)	E_x (GPa)	E_x (GPa)	E_{cx} (GPa)	E_{cx} (GPa)
24	198	31	227	143	227	143	221	121
815	188	30	217	138	217	138	212	117
1090	179	30	212	136	212	136	205	115
1370	116	28	183	134	184	134	170	113

E_x - laminate tensile modulus in longitudinal direction of composite specimen
E_{cx} - composite longitudinal tensile modulus
fiber tow undulation height H=610μm
longitudinal fiber tow undulation length $2L_{0°}$=1.57mm
off-axis (±60°) fiber tow undulation lengths $2L_{-60°}=2L_{+60°}$=2.15mm

Table XXXI: Enhanced SiC/SiC Measured and Predicted Secondary Tensile Moduli Near the Composite Ultimate Strength as a Function of Temperature in Air.

T (°C)	measured E_{c2} (GPa)	ROM E_{c2} (GPa)
24	18±2	32
815	15±3	31
1090	13	29
1370	5	17

measured - mean and one standard deviation values from tensile tests
ROM - rule of mixtures

Table XXXII: Nicalon Mean Ultimate Tensile Strengths as a Function of Temperature in Air.

T (°C)	σ_{fu} (GPa)
24	1.9
815	1.8
1090	1.5
1370	1.0

σ_{fu} - mean ultimate strength of Nicalon fiber
Weibull modulus m=4.2
mean fiber diameter D=13 μm

Table XXXIII: Enhanced SiC/SiC Theoretical and Experimental Ultimate Tensile Strengths as a Function of Temperature in Air.

T (°C)	experimental (MPa)	ROM (MPa)	Curtin (MPa)	Evans 1995 (MPa)	Cao & Thouless (MPa)
24	141±9	323	580	219	172
815	162±12	299	545	306	188
1090	169±12	253	477	259	158
1370	121	170	345	174	104

experimental - mean and one standard deviation values from tensile tests
ROM - rule of mixtures
Curtin - Curtin's theory incorporating rule of mixtures and Weibull statistics with L_f=75 mm
Evans 1995 - Evans' theory using fiber bundle theory with no matrix material with L_f=75 mm and L_c=25 mm except L_c=140 mm at room temperature
Cao & Thouless - Theory incorporating rule of mixtures and Weibull statistics

Table XXXIV. Intermediate Results for the Theory of Cao and Thouless for Predicting the Ultimate Strength of Enhanced SiC/SiC. The Variables are a Function of Temperature in Air.

T (°C)	σ_{fu} (GPa)	σ_o (MPa)
24	1.9	104
815	1.8	98
1090	1.5	82
1370	1.0	54

σ_{fu} - mean ultimate strength for Nicalon SiC fiber
σ_o - scale parameter
L_f = 75 mm
R = 7 μm
m = 4.2
A_o = 1 m^2

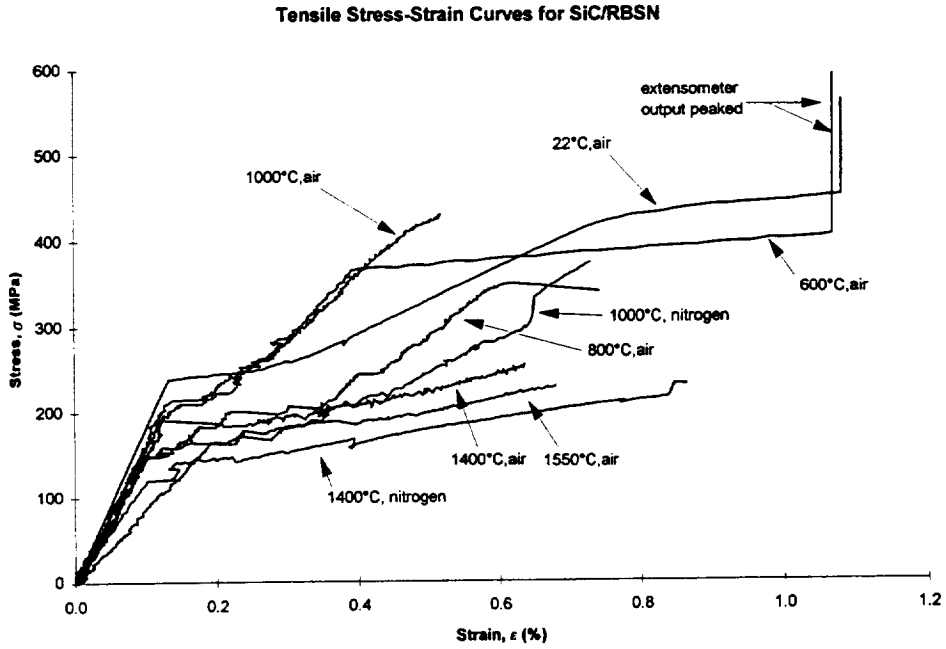

Figure 14. Tensile stress-strain curves for unidirectional SiC/RBSN composites tested from various temperatures in air and nitrogen and loaded in the fiber direction.

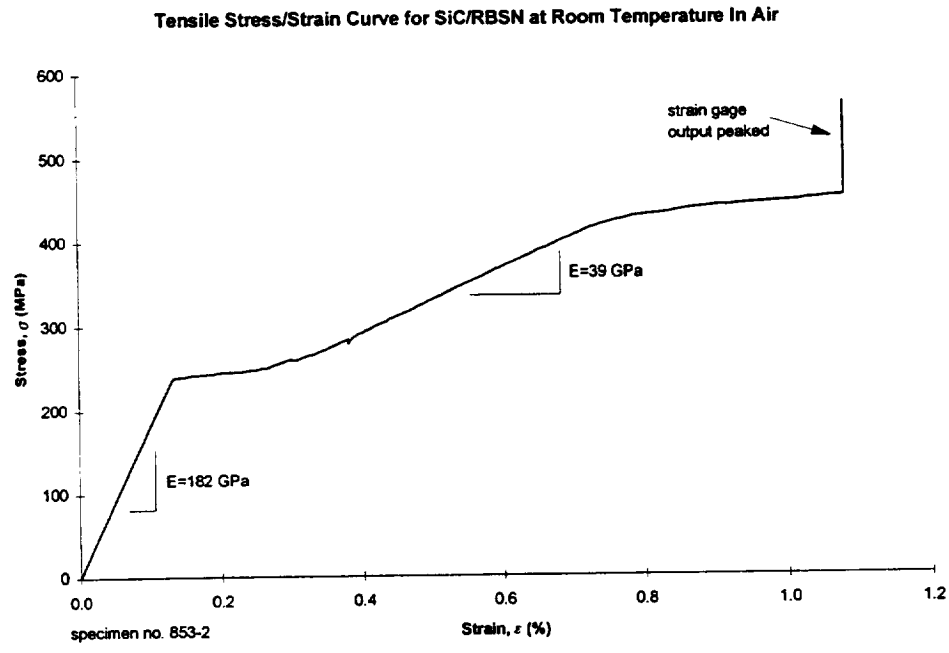

Figure 15. Tensile stress-strain curve for unidirectional SiC/RBSN composite tested at room temperature in air and loaded in the primary direction.

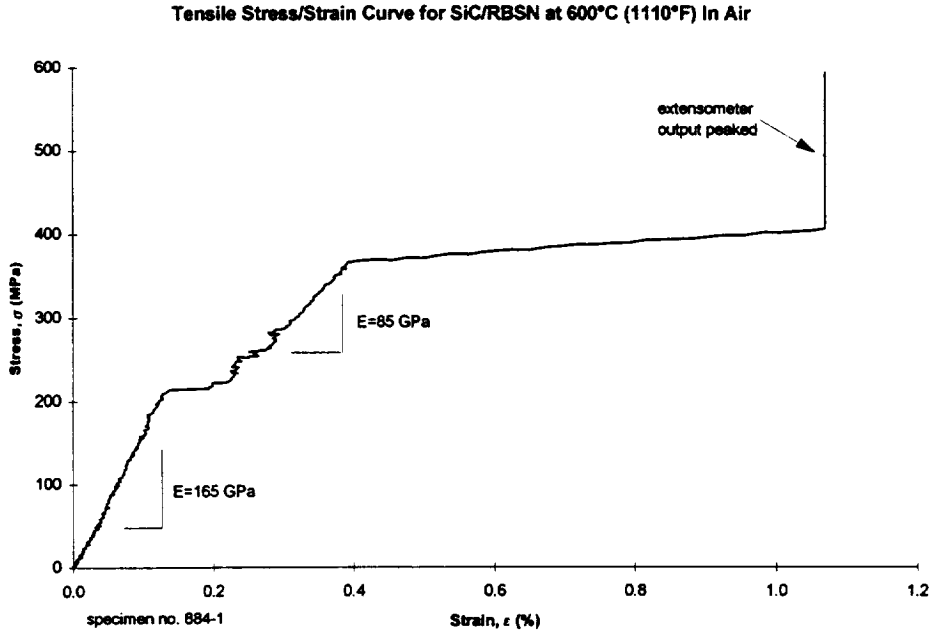

Figure 16. Tensile stress-strain curve for unidirectional SiC/RBSN composite tested at 600°C in air and loaded in the primary direction.

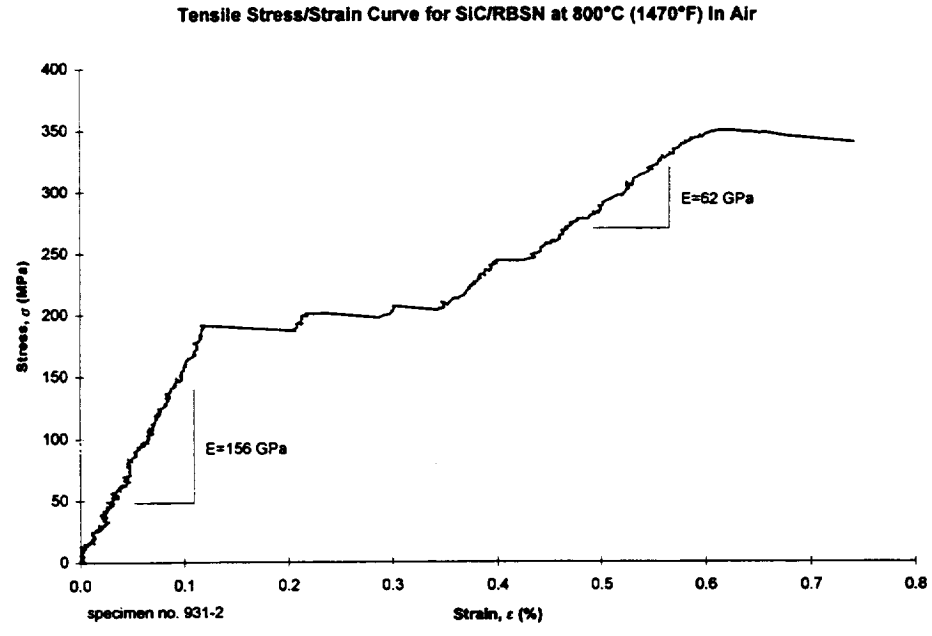

Figure 17. Tensile stress-strain curve for unidirectional SiC/RBSN composite tested at 800°C in air and loaded in the primary direction.

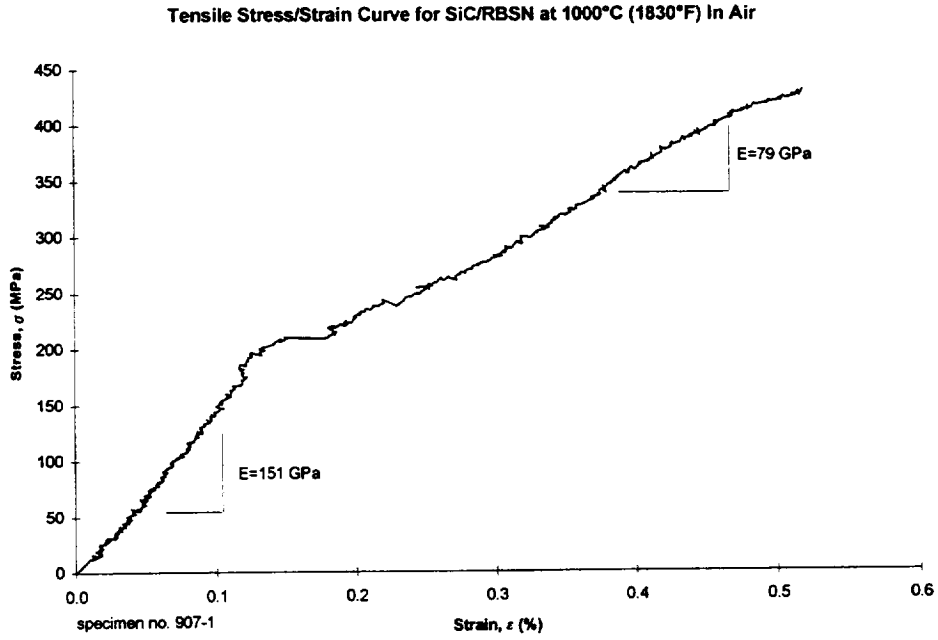

Figure 18. Tensile stress-strain curve for unidirectional SiC/RBSN composite tested at 1000°C in air and loaded in the primary direction.

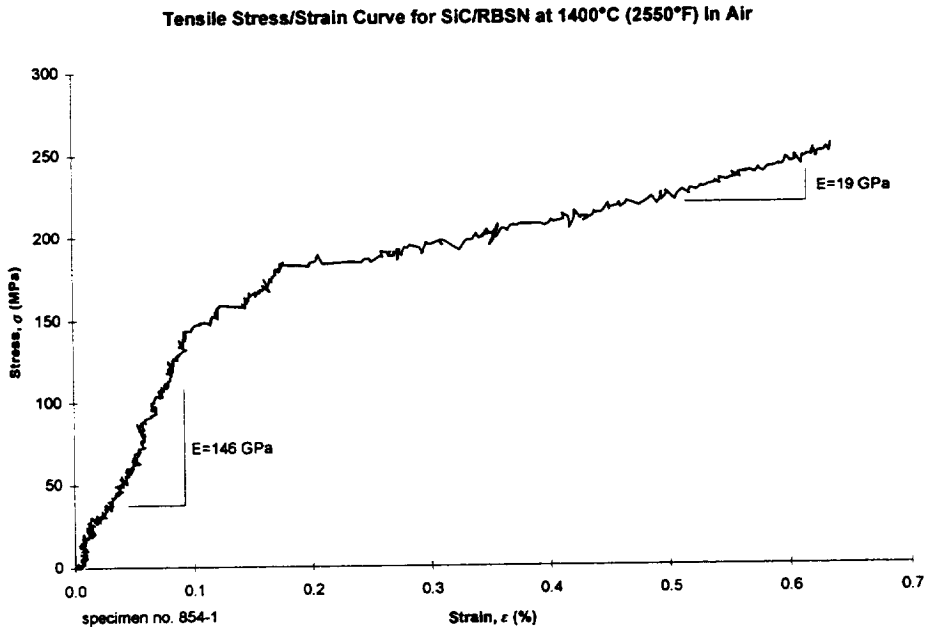

Figure 19. Tensile stress-strain curve for unidirectional SiC/RBSN composite tested at 1400°C in air and loaded in the primary direction.

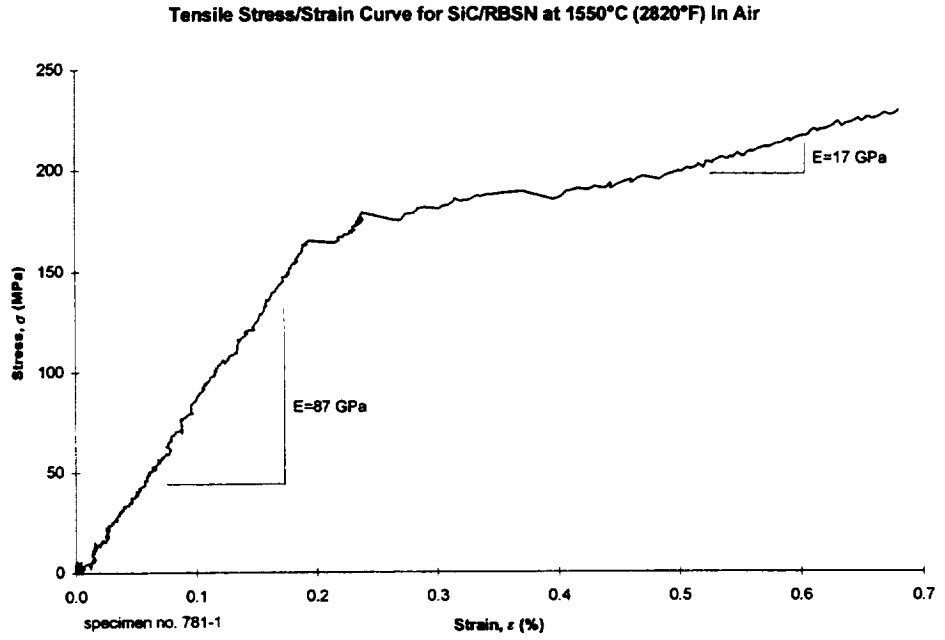

Figure 20. Tensile stress-strain curve for unidirectional SiC/RBSN composite tested at 1550°C in air and loaded in the primary direction.

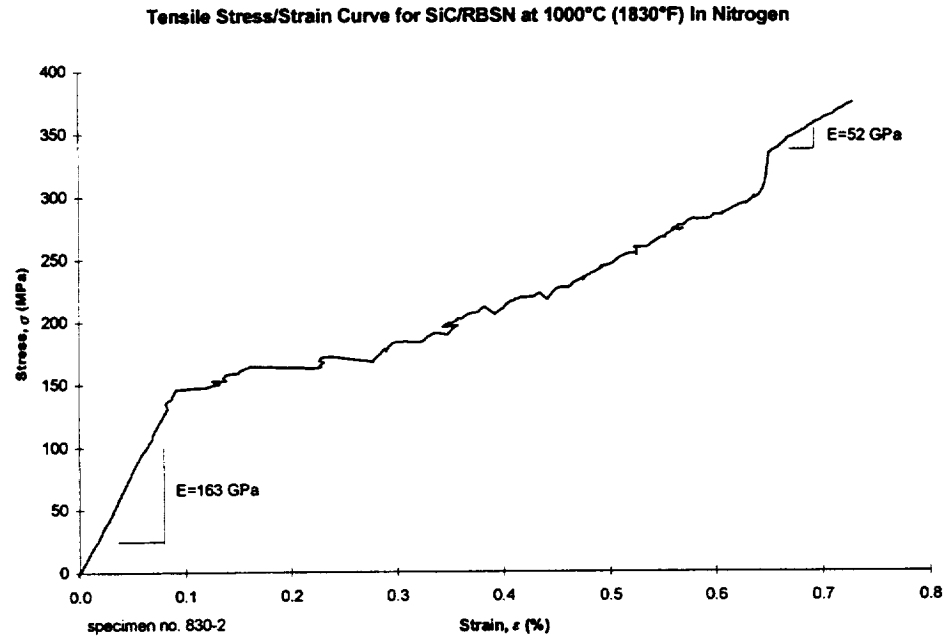

Figure 21. Tensile stress-strain curve for unidirectional SiC/RBSN composite tested at 1000°C in nitrogen and loaded in the primary direction.

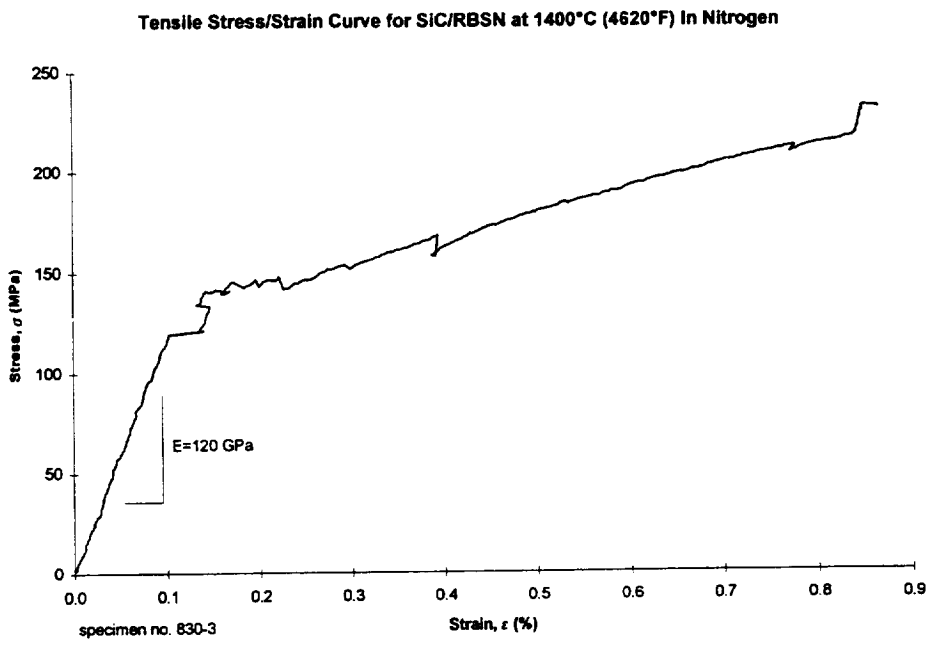

Figure 22. Tensile stress-strain curve for unidirectional SiC/RBSN composite tested at 1400°C in nitrogen and loaded in the primary direction.

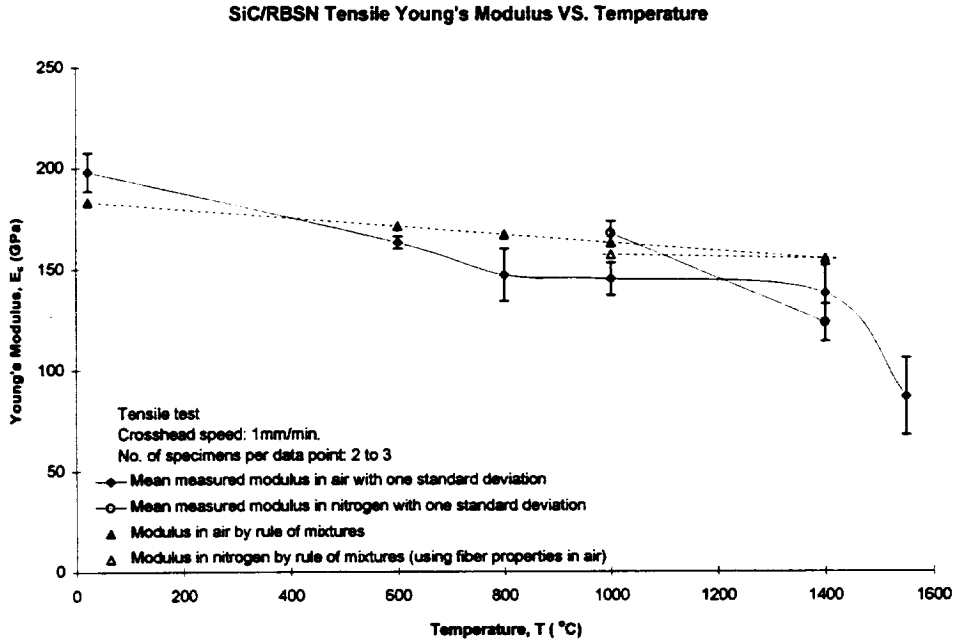

Figure 23. Tensile Young's modulus versus temperature in air and nitrogen for unidirectional SiC/RBSN composites when loaded in the primary direction.

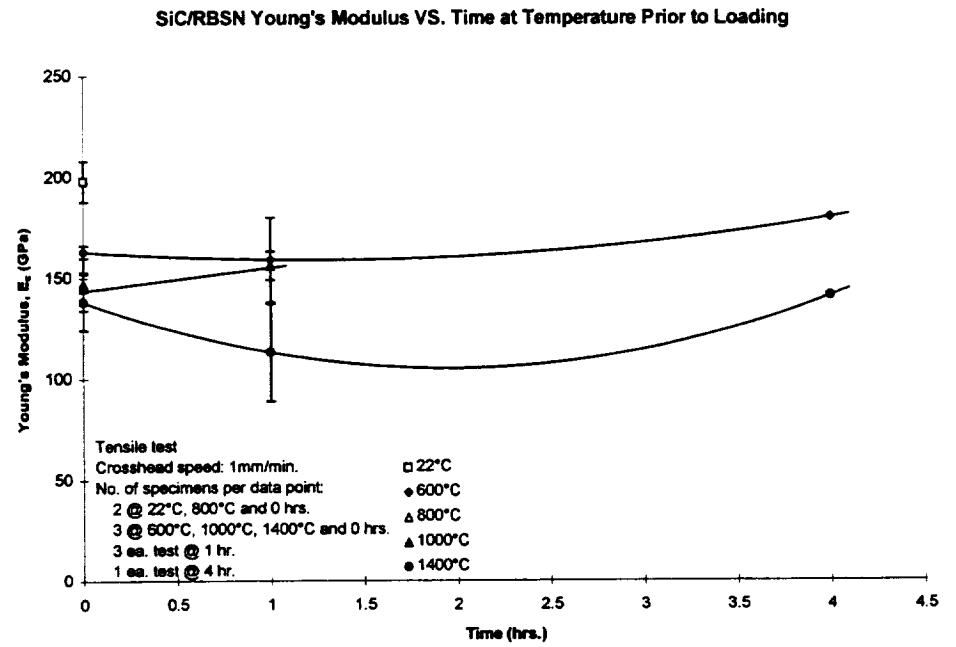

Figure 24. The mean tensile Young's modulus with one standard deviation as a function of time of exposure to high temperatures in air.

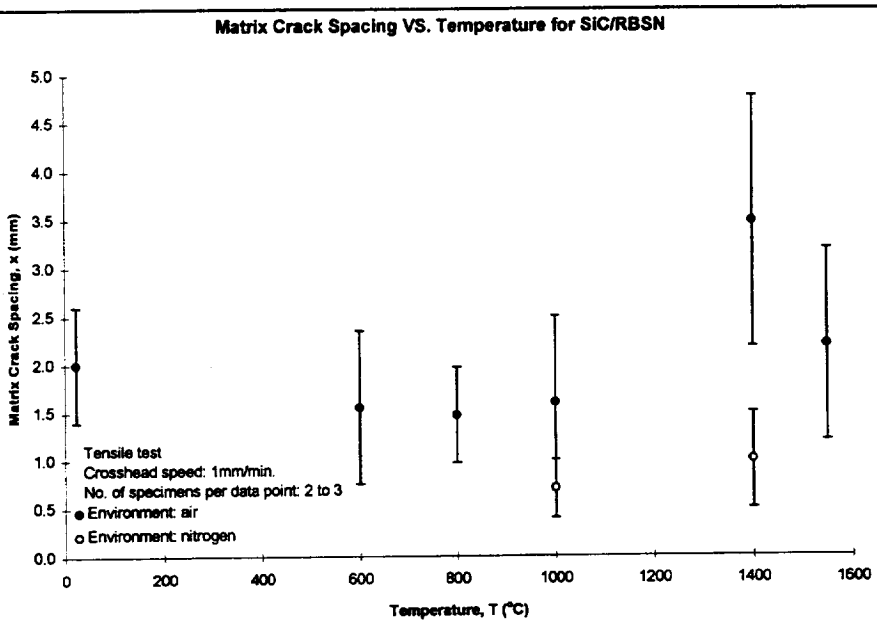

Figure 25. Mean matrix crack spacing with one standard deviation versus temperature in air and nitrogen for unidirectional SiC/RBSN composites when loaded in the primary direction.

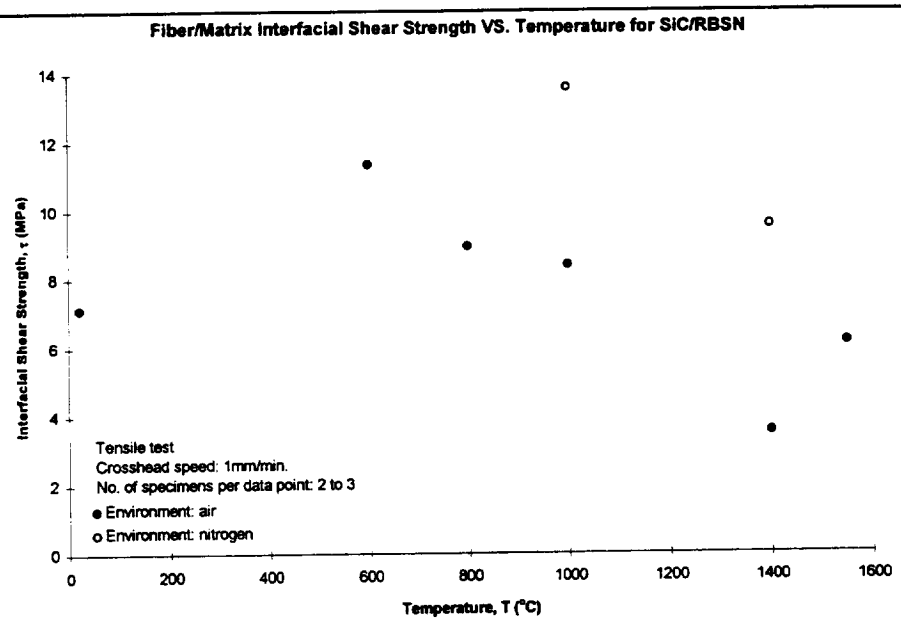

Figure 26. Calculated interfacial shear strength (from crack spacing measurements) versus temperature in air and nitrogen for SiC/RBSN composites.

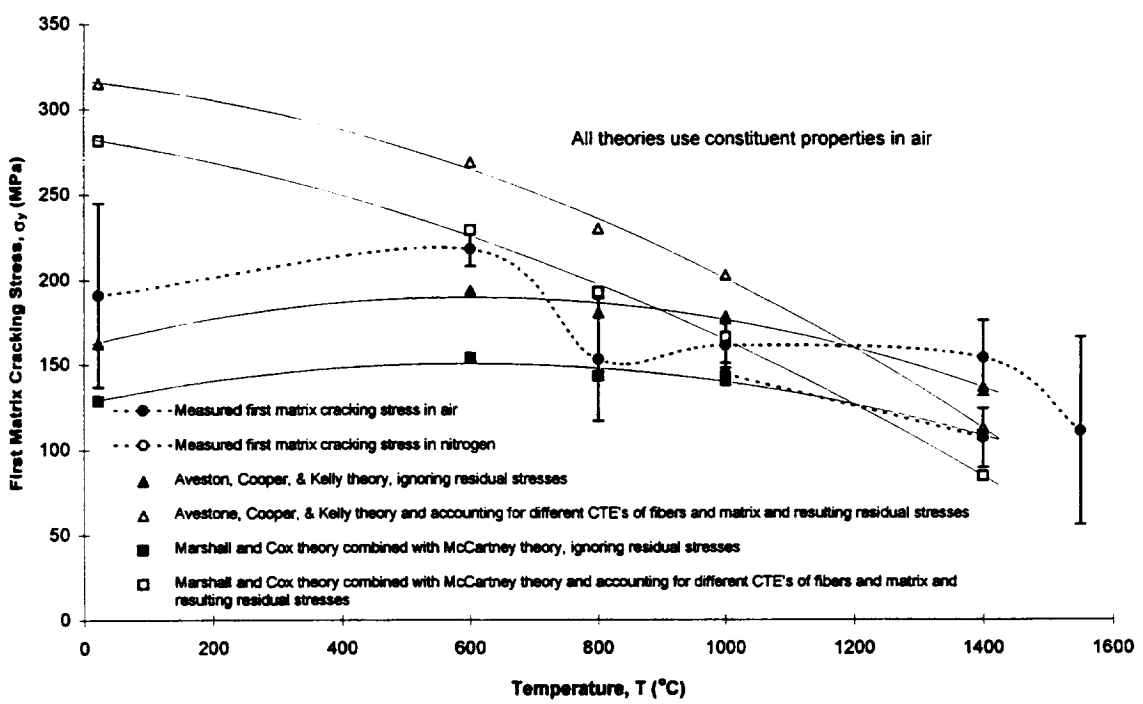

Figure 27. Average, with one standard deviation, measured and predicted unidirectional SiC/RBSN composite first matrix cracking stresses as a function of temperature. Predictions of the composite first matrix cracking stress use constituent properties. The environments were air and nitrogen and loading was along the primary direction.

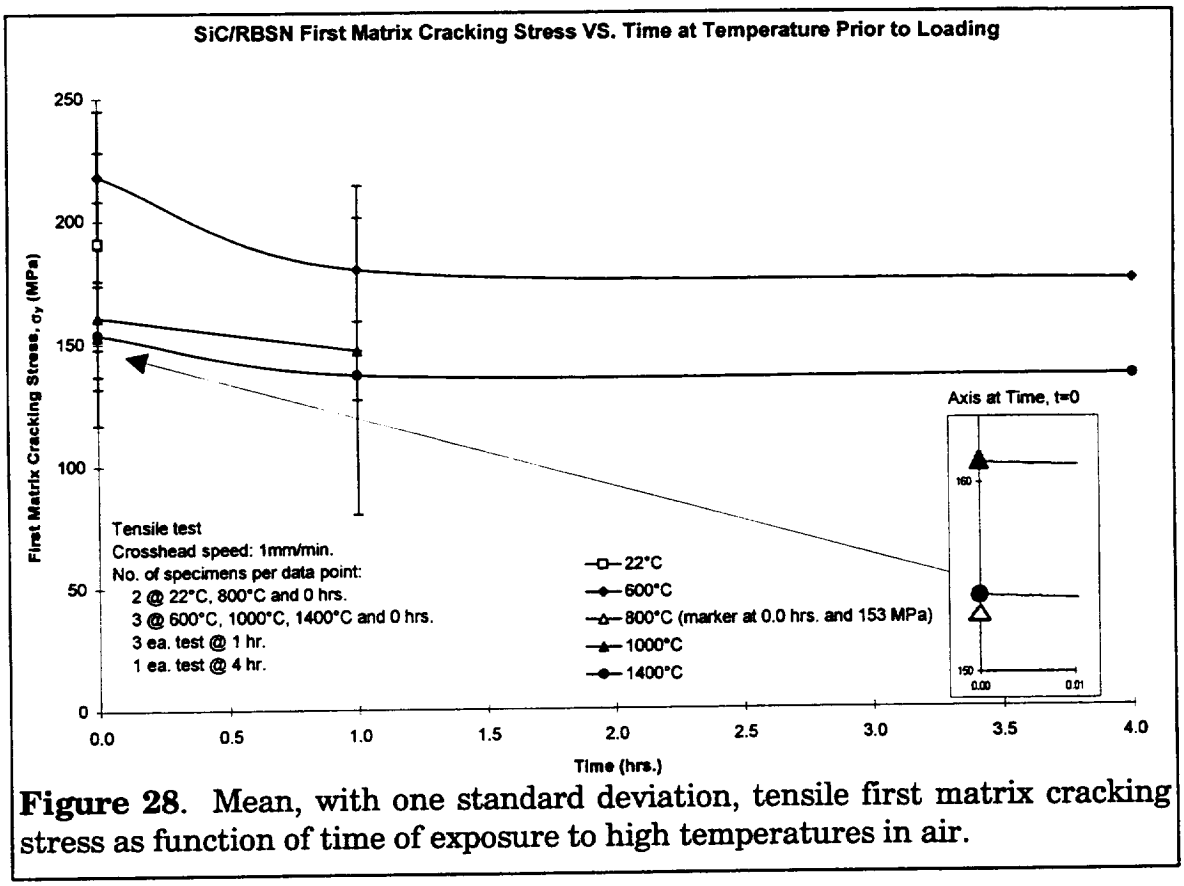

Figure 28. Mean, with one standard deviation, tensile first matrix cracking stress as function of time of exposure to high temperatures in air.

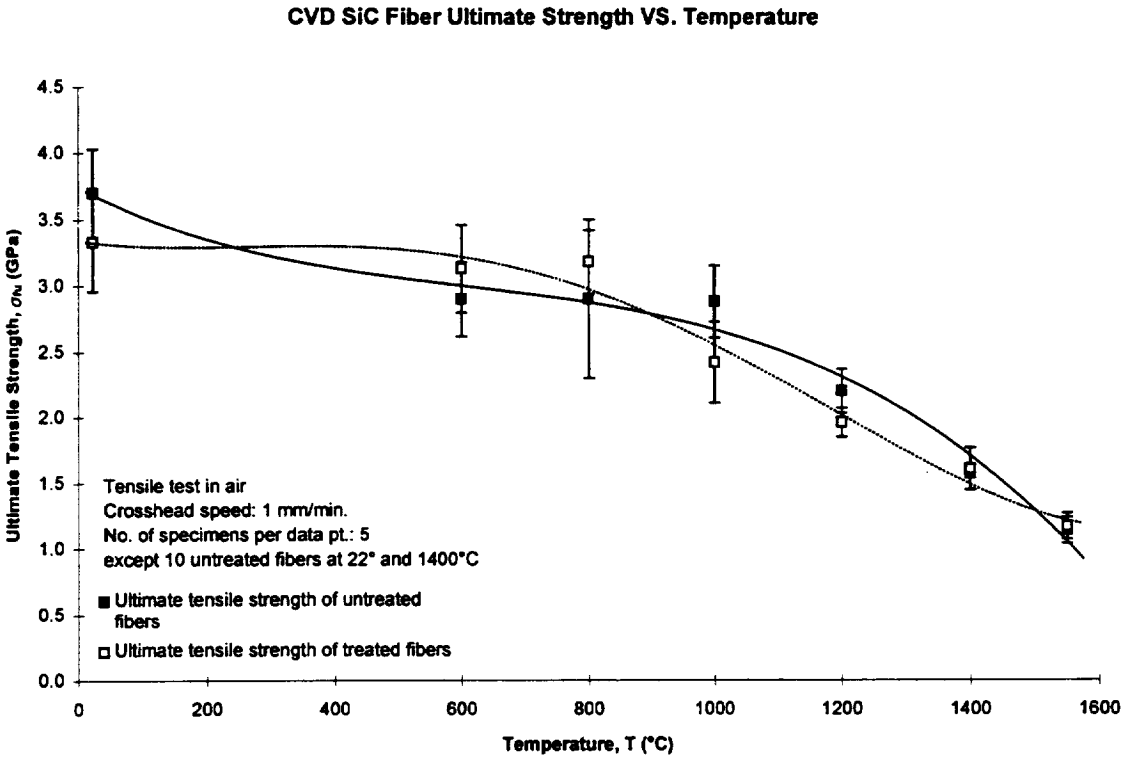

Figure 29. Mean ultimate tensile strength with one standard deviation of CVD type SiC fibers as a function of temperature in air. Untreated fibers were "as received" and treated fibers were put through the processing conditions of the SiC/RBSN composite.

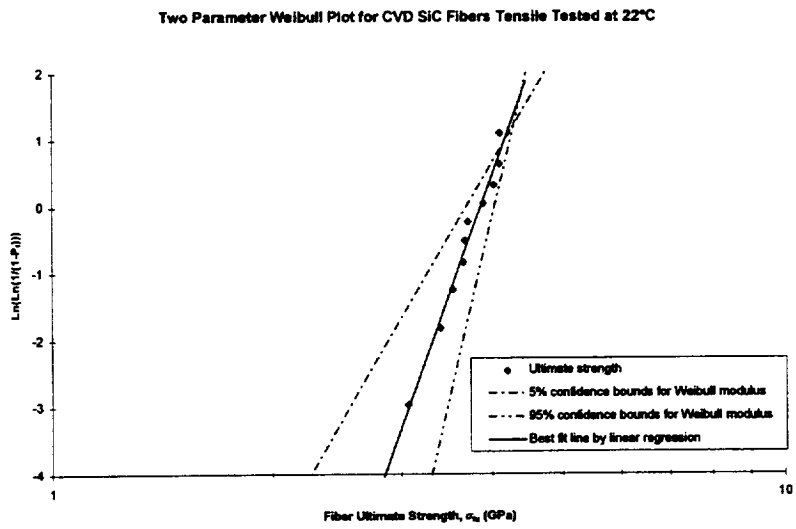

Figure 30. Ln(Ln(1/(1-P_f)) versus the ultimate strength of individual CVD SiC fibers tensile tested at room temperature. Ninety percent confidence bounds determined as per ASTM (1995) standard designation C 1239-94a.

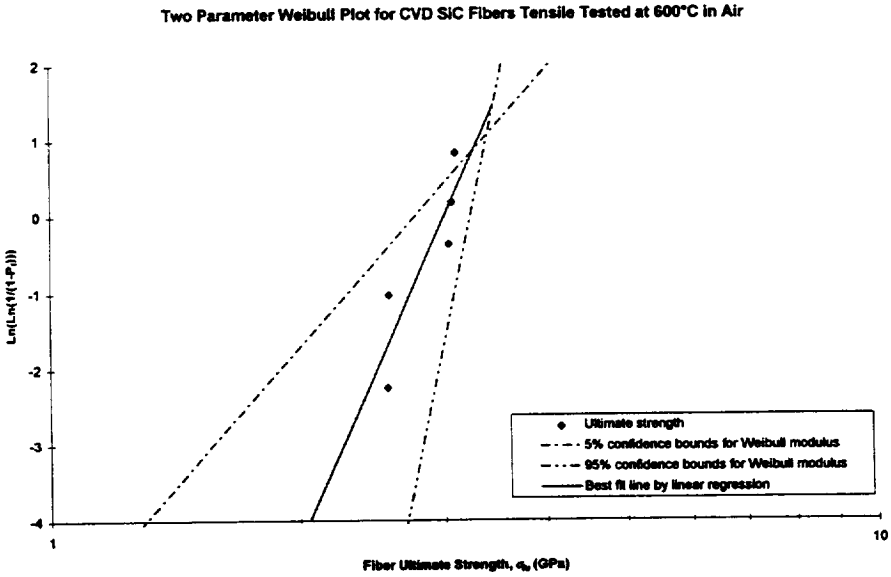

Figure 31. Ln(Ln(1/(1-P_f)) versus the ultimate strength of individual CVD SiC fibers tensile tested at 600°C in air. Ninety percent confidence bounds determined as per ASTM (1995) standard designation C 1239-94a.

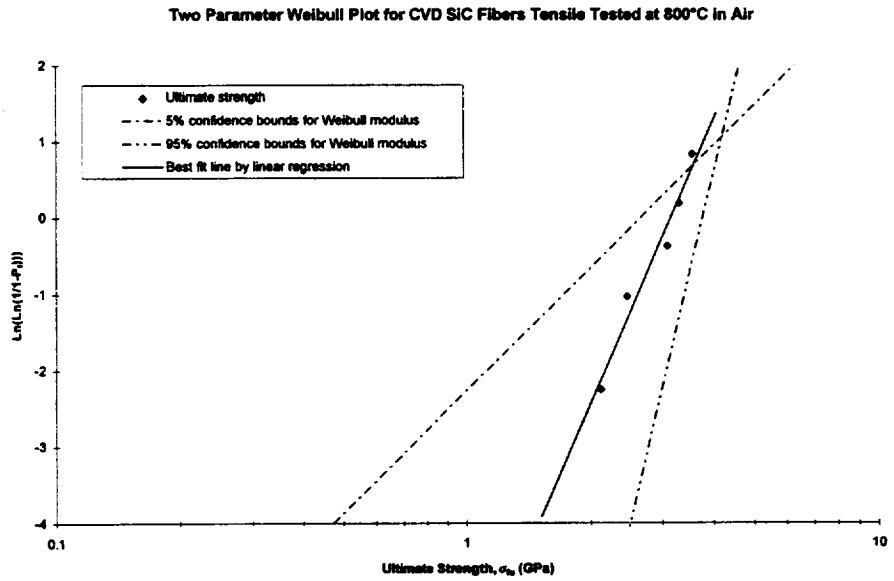

Figure 32. Ln(Ln(1/(1-P_f)) versus the ultimate strength of individual CVD SiC fibers tensile tested at 800°C in air. Ninety percent confidence bounds determined as per ASTM (1995) standard designation C 1239-94a.

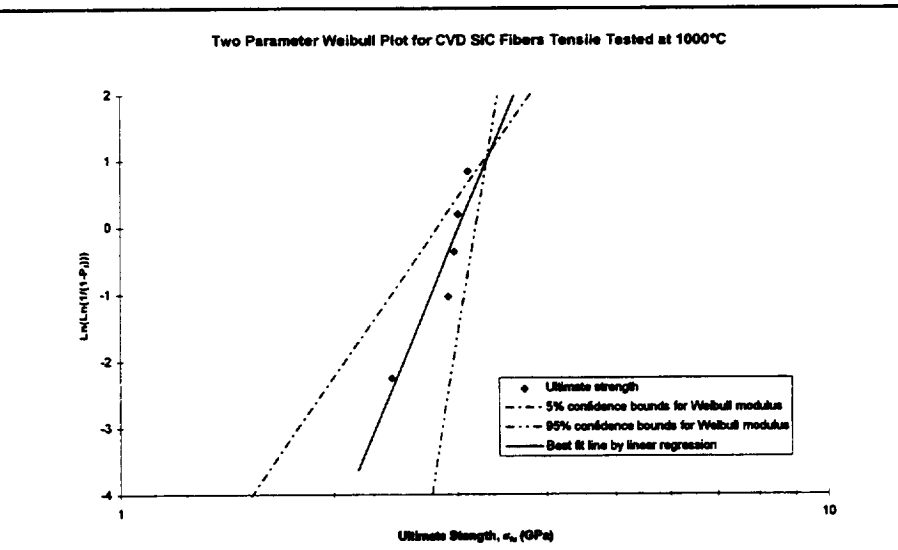

Figure 33. Ln(Ln(1/(1-P_f)) versus the ultimate strength of individual CVD SiC fibers tensile tested at 1000°C in air. Ninety percent confidence bounds determined as per ASTM (1995) standard designation C 1239-94a.

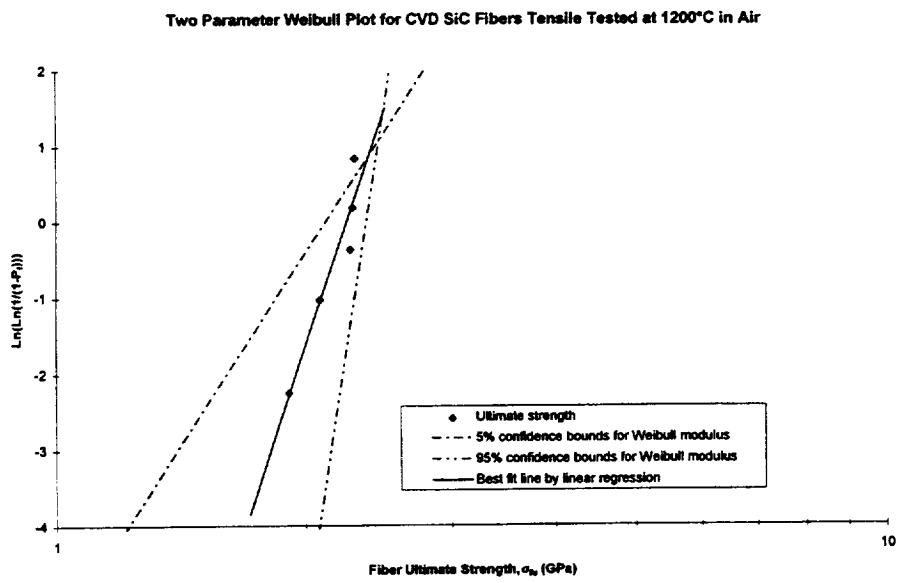

Figure 34. Ln(Ln(1/(1-P_f)) versus the ultimate strength of individual CVD SiC fibers tensile tested at 1200°C in air. Ninety percent confidence bounds determined as per ASTM (1995) standard designation C 1239-94a.

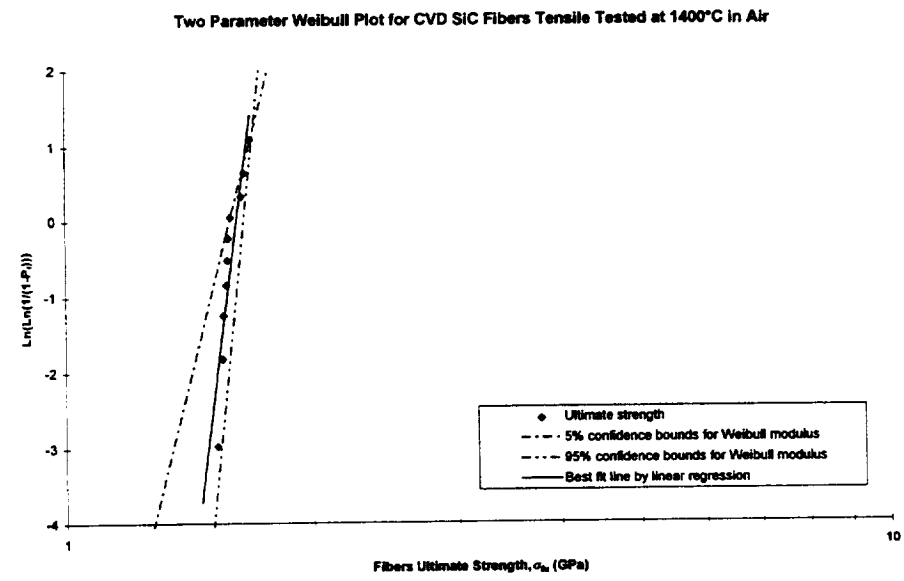

Figure 35. Ln(Ln(1/(1-P_f)) versus the ultimate strength of individual treated CVD SiC fibers tensile tested at 1400°C in air. Ninety percent confidence bounds determined as per ASTM (1995) standard designation C 1239-94a.

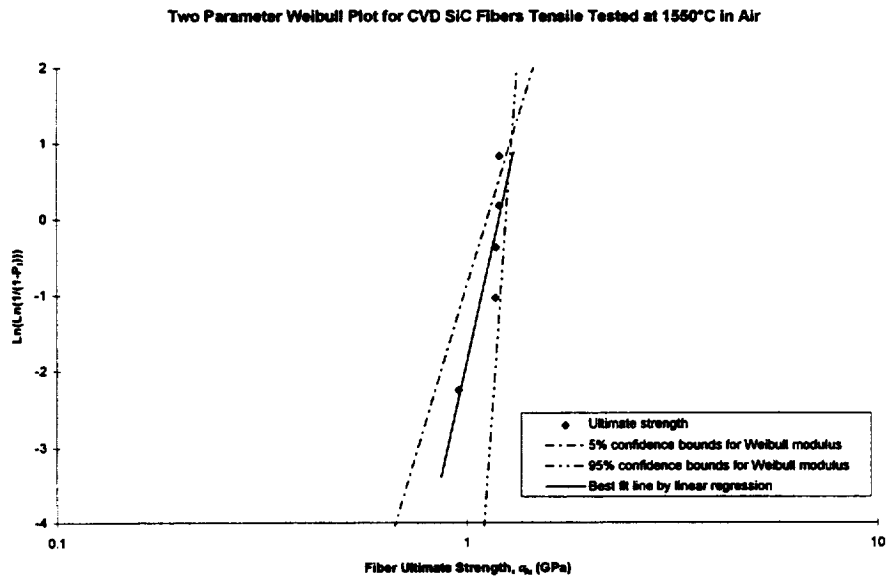

Figure 36. $Ln(Ln(1/(1-P_f))$ versus the ultimate strength of individual CVD SiC fibers tensile tested at 1550°C in air. Ninety percent confidence bounds determined as per ASTM (1995) standard designation C 1239-94a.

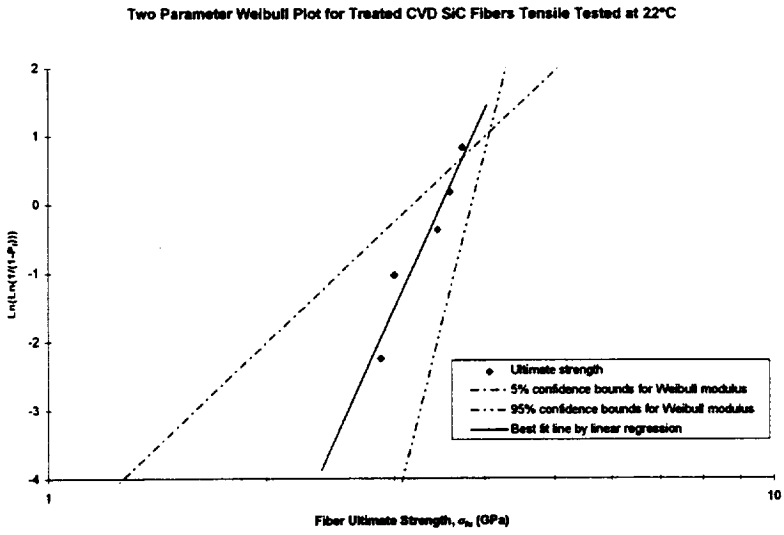

Figure 37. Ln(Ln(1/(1-P_f)) versus the ultimate strength of individual treated CVD SiC fibers tensile tested at room temperature. Ninety percent confidence bounds determined as per ASTM (1995) standard designation C 1239-94a.

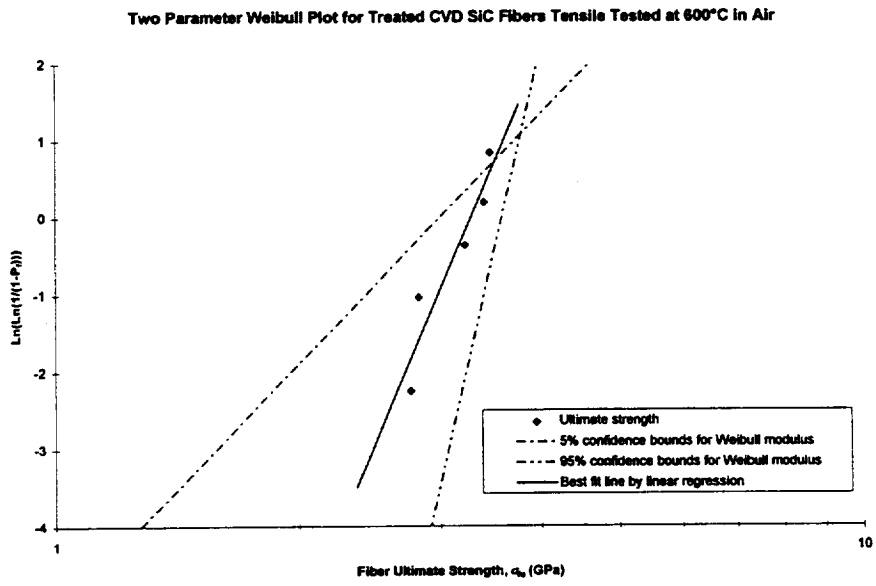

Figure 38. Ln(Ln(1/(1-P_f)) versus the ultimate strength of individual treated CVD SiC fibers tensile tested at 600°C in air. Ninety percent confidence bounds determined as per ASTM (1995) standard designation C 1239-94a.

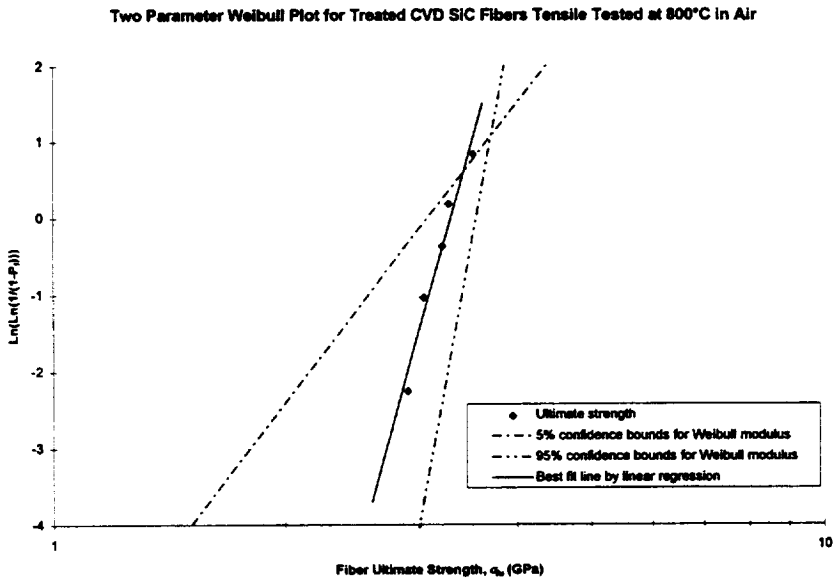

Figure 39. Ln(Ln(1/(1-P_f)) versus the ultimate strength of individual treated CVD SiC fibers tensile tested at 800°C in air. Ninety percent confidence bounds determined as per ASTM (1995) standard designation C 1239-94a.

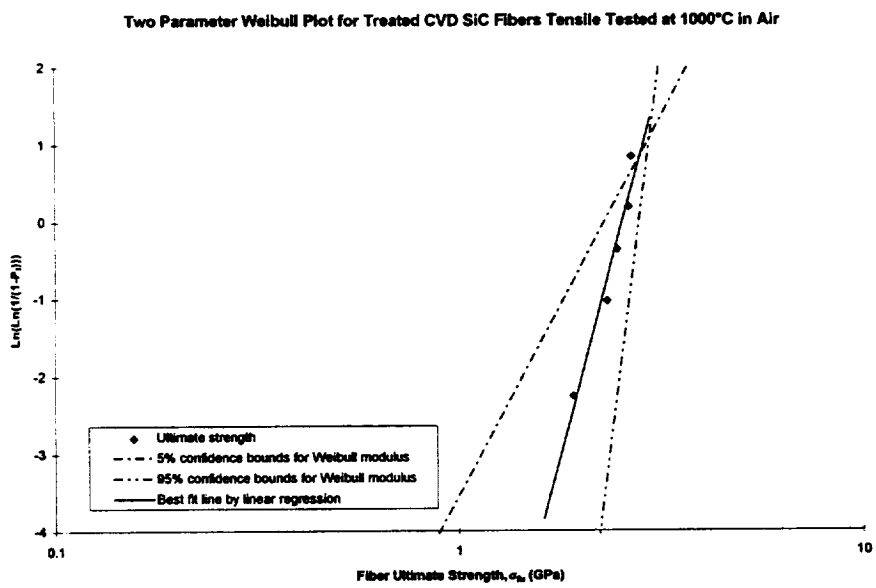

Figure 40. Ln(Ln(1/(1-P_f)) versus the ultimate strength of individual treated CVD SiC fibers tensile tested at 1000°C in air. Ninety percent confidence bounds determined as per ASTM (1995) standard designation C 1239-94a.

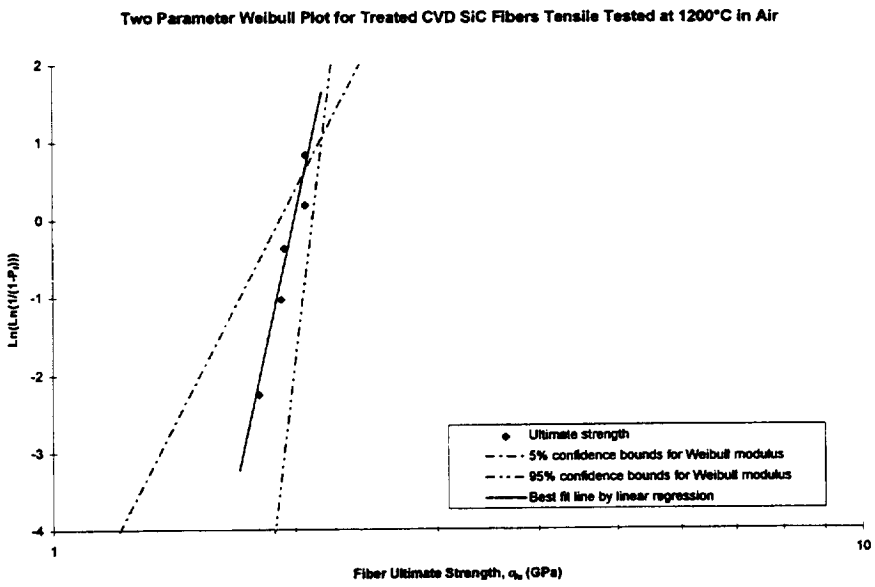

Figure 41. Ln(Ln(1/(1-P_f)) versus the ultimate strength of individual treated CVD SiC fibers tensile tested at 1200°C in air. Ninety percent confidence bounds determined as per ASTM (1995) standard designation C 1239-94a.

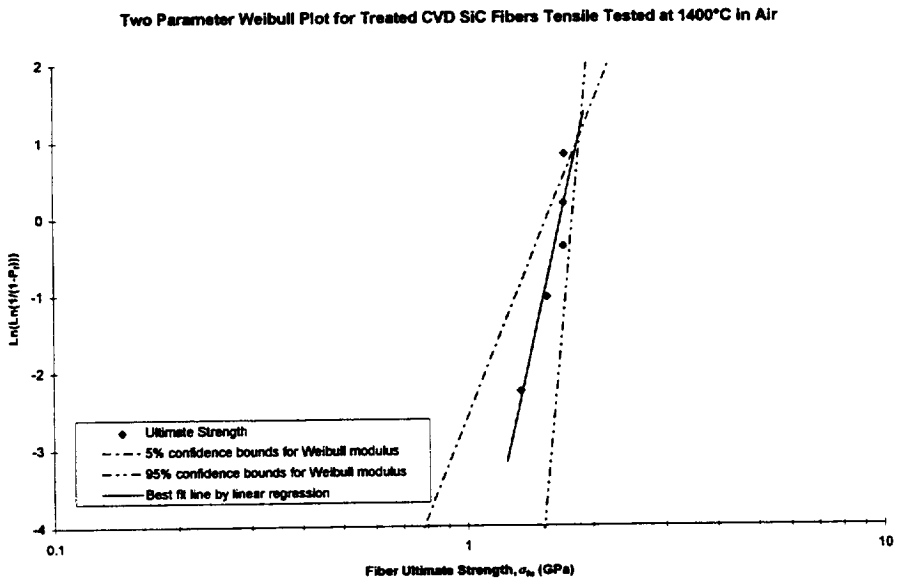

Figure 42. Ln(Ln(1/(1-P_f)) versus the ultimate strength of individual treated CVD SiC fibers tensile tested at 1400°C in air. Ninety percent confidence bounds determined as per ASTM (1995) standard designation C 1239-94a.

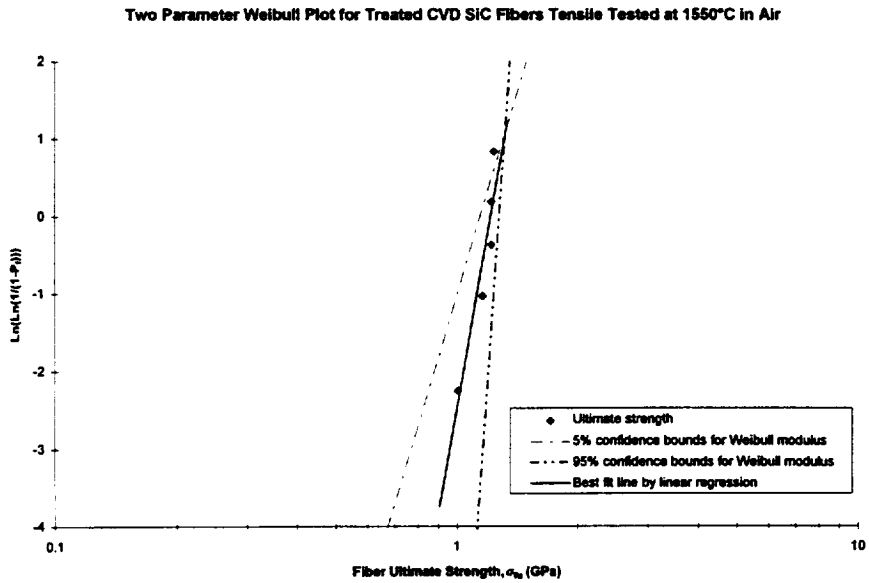

Figure 43. Ln(Ln(1/(1-P_f)) versus the ultimate strength of individual treated CVD SiC fibers tensile tested at 1550°C in air. Ninety percent confidence bounds determined as per ASTM (1995) standard designation C 1239-94a.

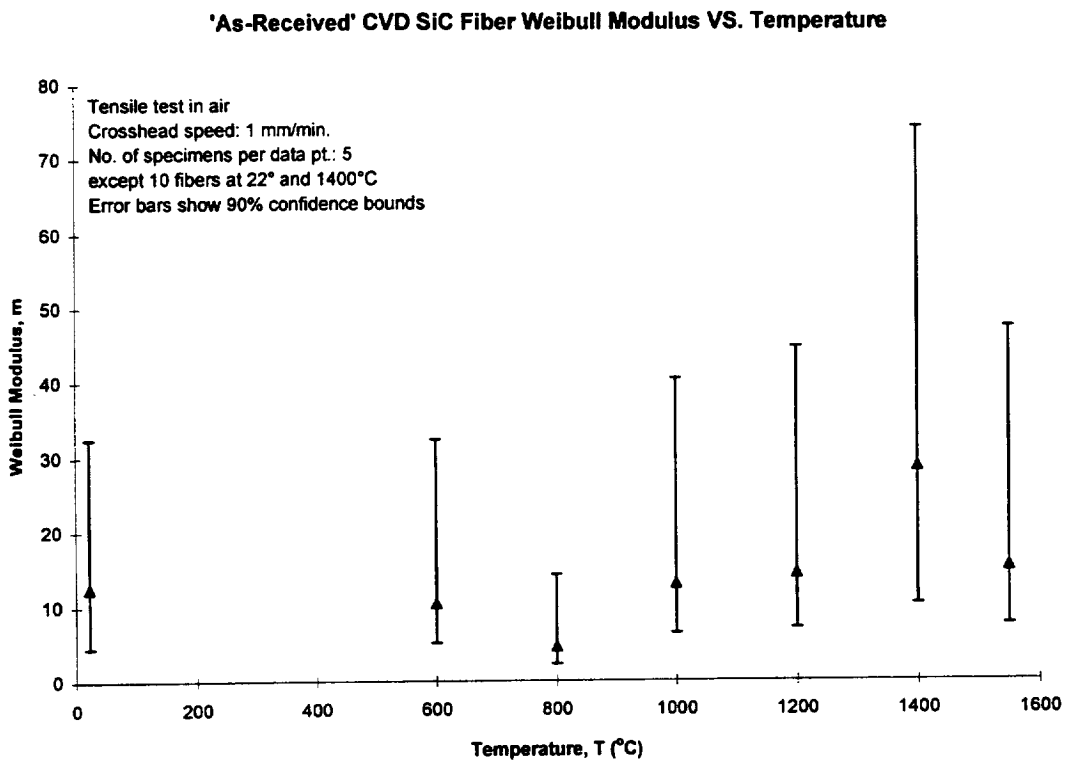

Figure 44. Weibull modulus of 'as-received' CVD type SiC fibers as a function of temperature in air.

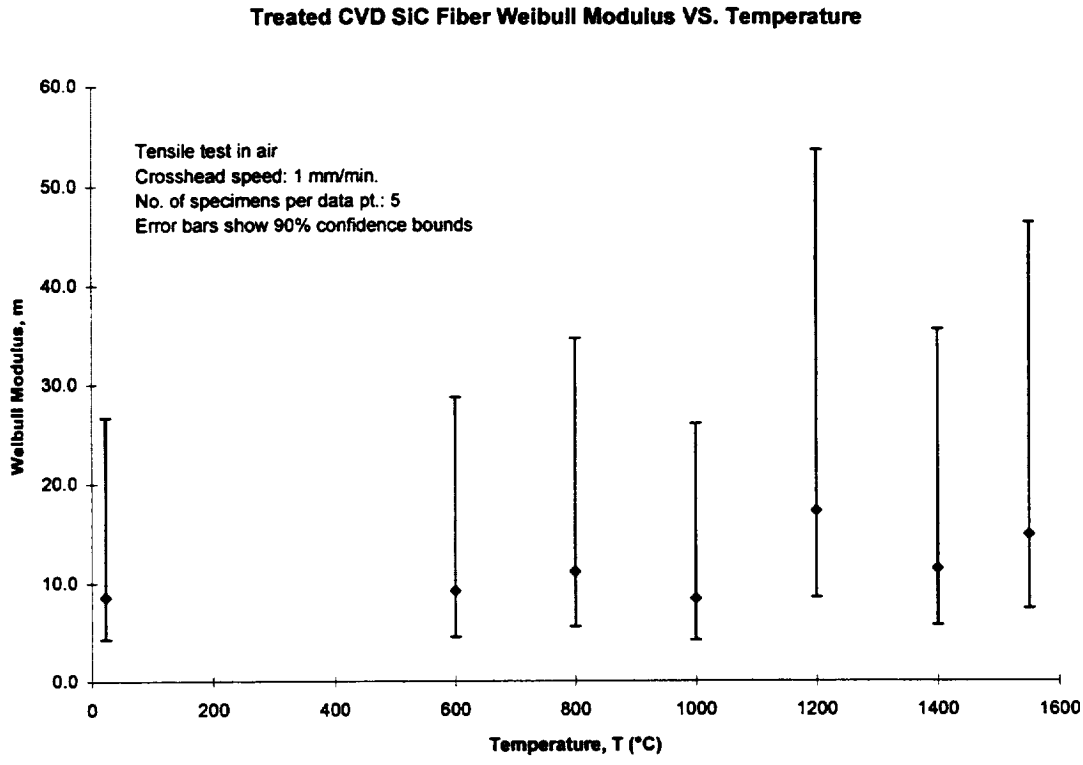

Figure 45. Weibull modulus of treated CVD type SiC fibers as a function of temperature in air. Treated fibers were put through the processing conditions of the SiC/RBSN composite.

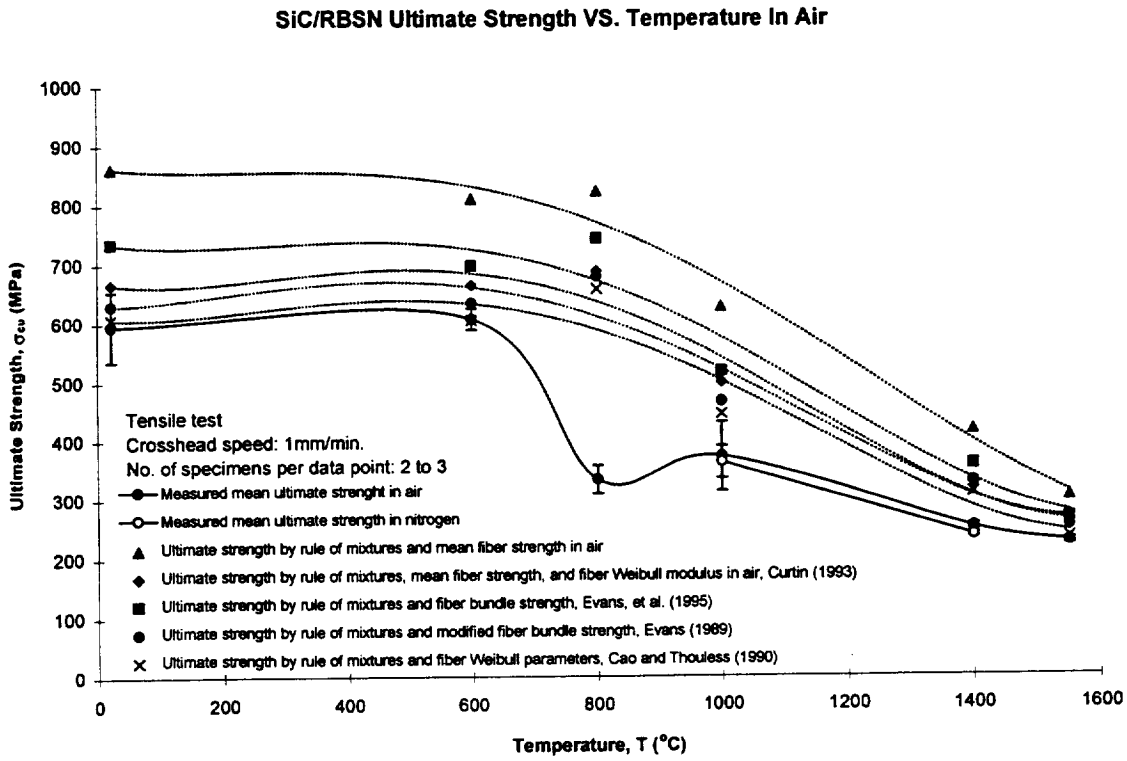

Figure 46. Average measured SiC/RBSN composite ultimate tensile strength with one standard deviation relative to predictions of the composite ultimate tensile strength using CVD SiC fiber properties as a function of temperature. The environments were air and nitrogen and loading was along the primary direction.

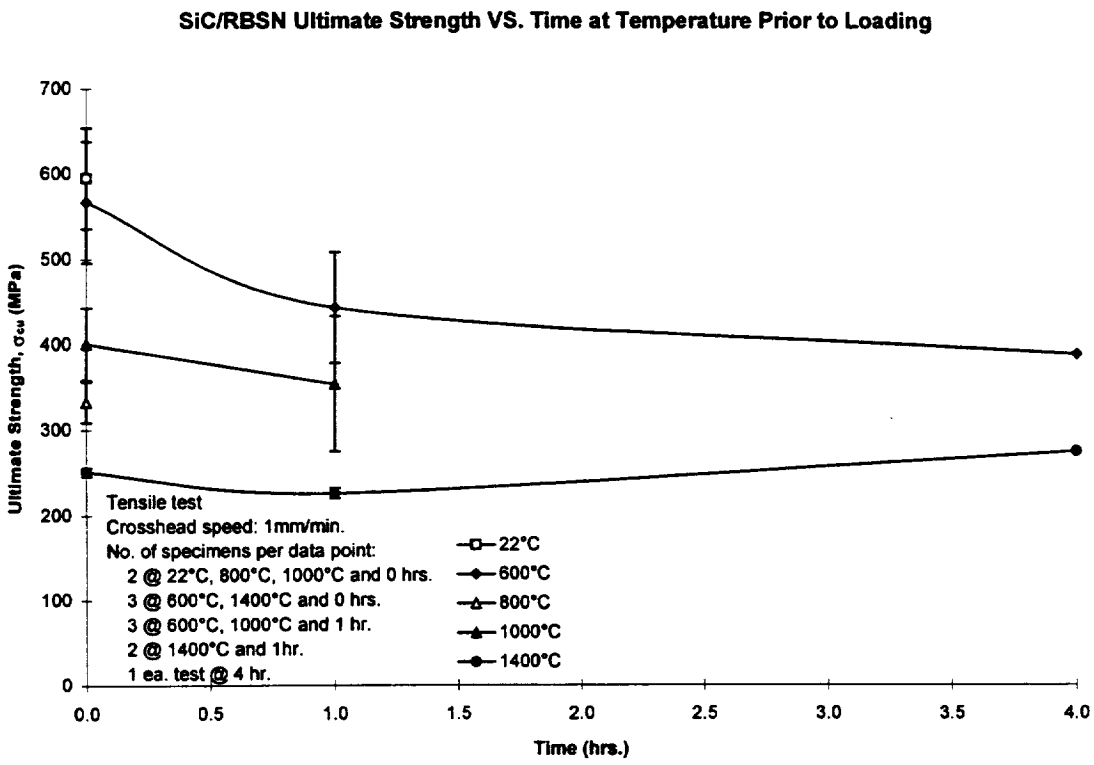

Figure 47. Composite mean ultimate tensile strength with one standard deviation as a function of time at high temperatures in air.

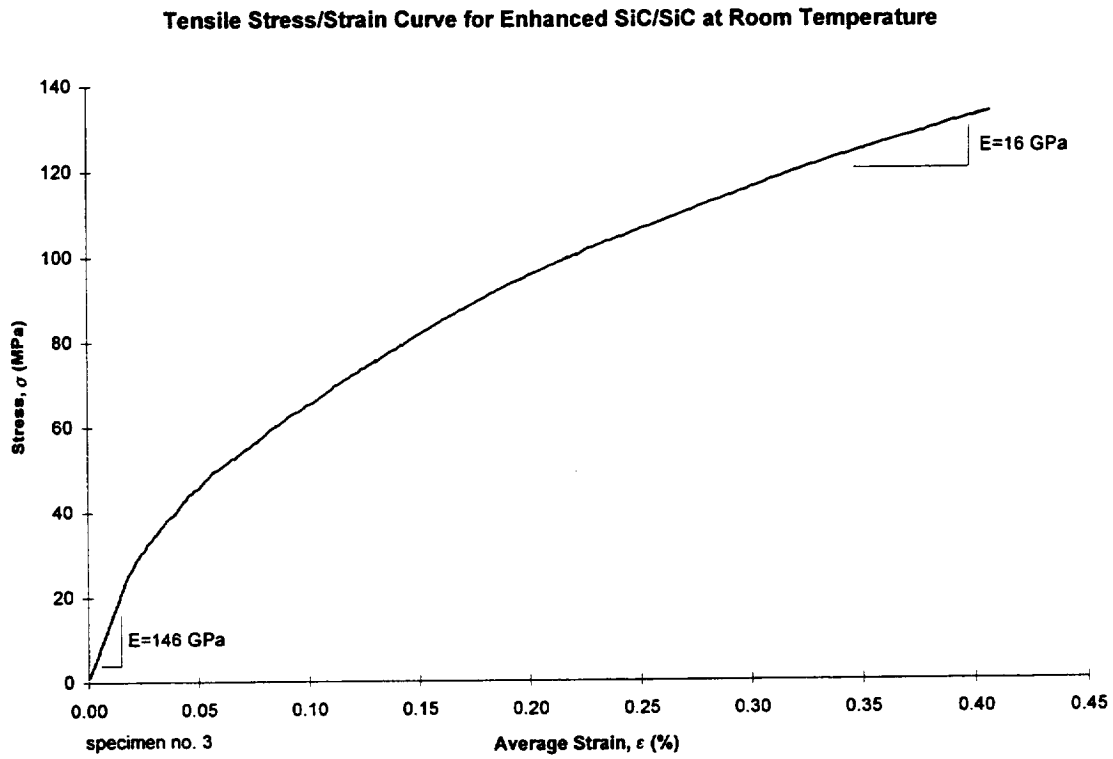

Figure 48. Tensile stress-strain curve for enhanced SiC/SiC composite tested at room temperature in air.

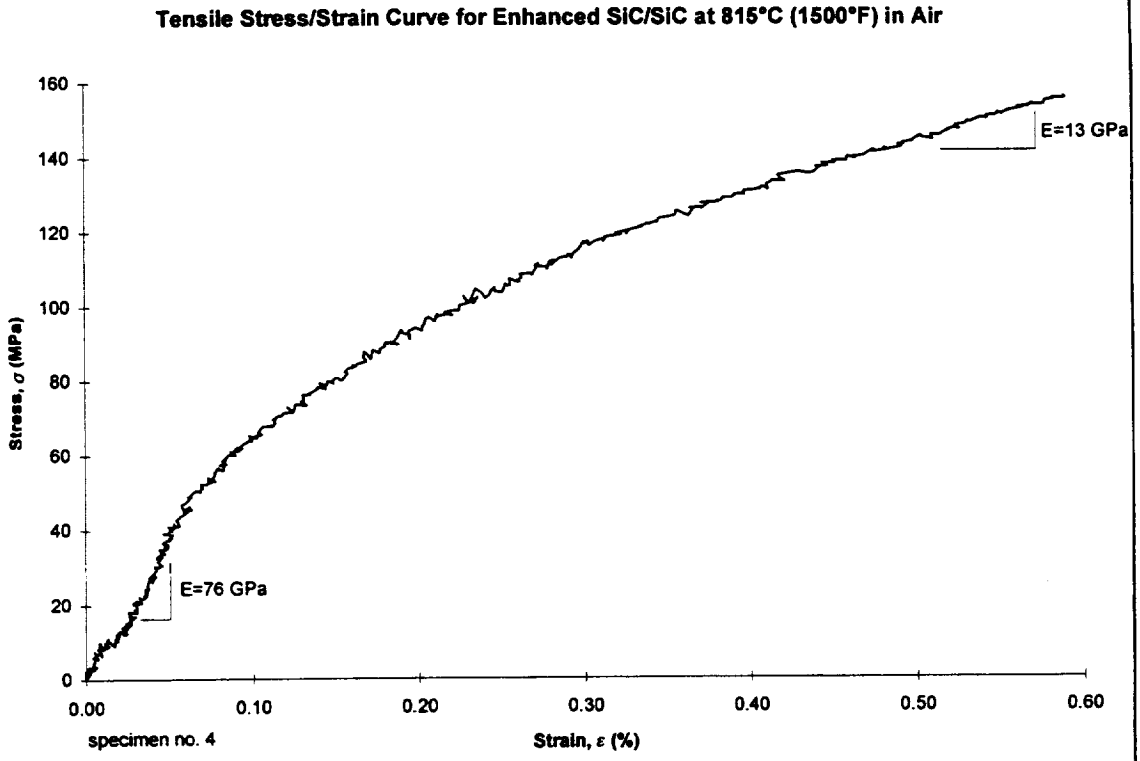

Figure 49. Tensile stress-strain curve for enhanced SiC/SiC composite tested at 815°C in air.

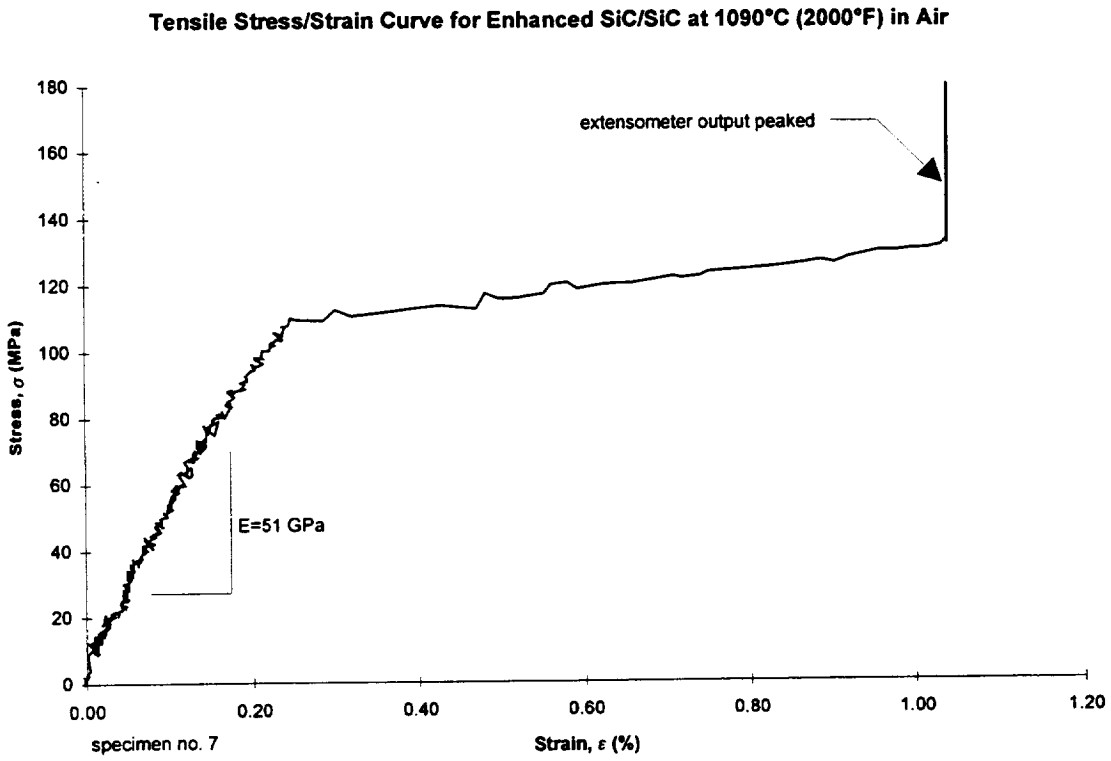

Figure 50. Tensile stress-strain curve for enhanced SiC/SiC composite tested at 1090°C in air.

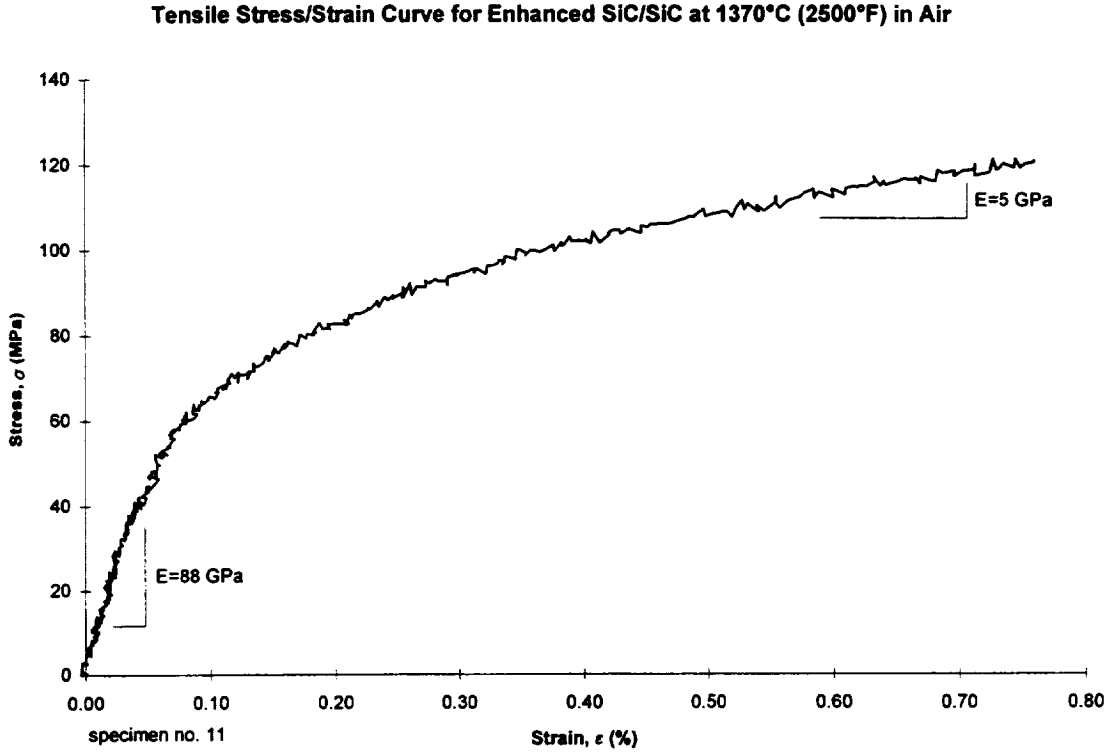

Figure 51. Tensile stress-strain curve for enhanced SiC/SiC composite tested at 1370°C in air.

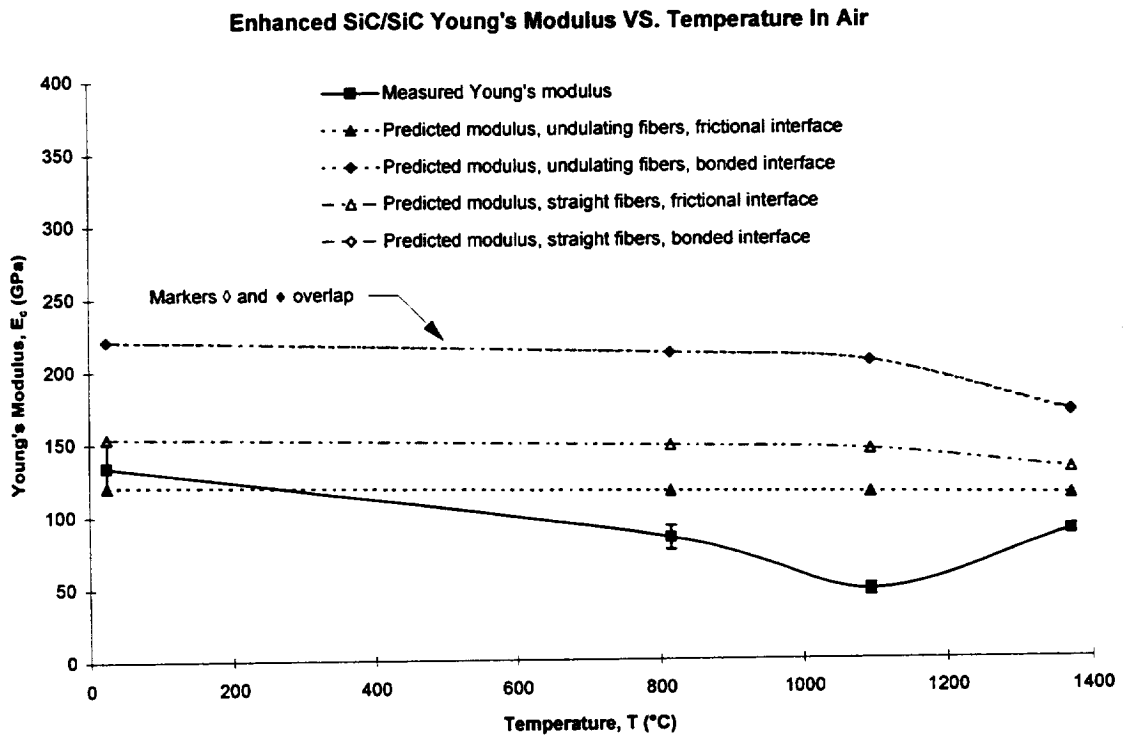

Figure 52. Measured and predicted Young's moduli versus temperature in air for enhanced SiC/SiC composites.

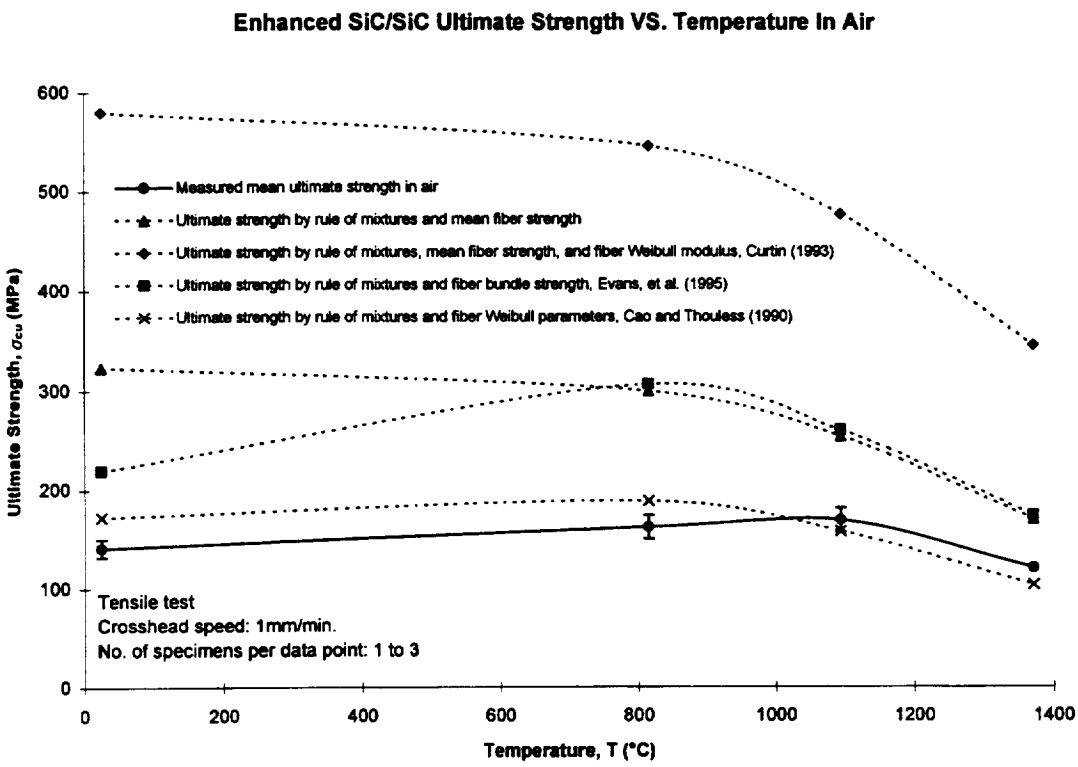

Figure 53. The average measured enhanced SiC/SiC composite ultimate tensile strength with one standard deviation relative to predictions of the composite ultimate tensile strength using Nicalon SiC fiber properties as a function of temperature. The environment was air.

CHAPTER VIII

SUMMARY AND CONCLUSION

A high temperature tensile testing facility for testing ceramic matrix composite coupons has been assembled and placed into operation at NASA Lewis Research Center. The system for testing in air is capable of operating at temperatures up to 1550°C (2820°F). The system for testing in an inert gas can test up to approximately 1700°C (3100°F) in nitrogen or argon gas. Both systems can be used for static tensile tests or low cycle fatigue tests. The temperature limits of these systems with the ability to measure strain, load, and temperature provide a materials testing capability to greater environmental extremes than previously in the research field for testing ceramic composites.

The composite systems studied include uniaxial silicon carbide fiber reinforced reaction bonded silicon nitride and an enhanced triaxially woven silicon carbide fiber reinforced silicon carbide. The SiC/RBSN composite was tensile tested at high temperatures in air from room temperature to 1550°C (2820°F) and nitrogen at 1000°C (1830°F) and 1400°C (2550°F). The enhanced SiC/SiC composite was tested from room temperature to 1370°C (2500°F) in air. In addition, a limited number of SiC/RBSN specimens were exposed to high temperatures in air for different durations with no load followed by loading until fracture. Another group of SiC/RBSN specimens were held under load at just over first matrix cracking stress and approximately at 80% of the first matrix cracking stress until complete fracture.

The SiC/RBSN composite exhibited progressive fracture at all the test temperatures of the short term static tensile tests. The Young's modulus shows an overall decrease as the test temperature was increased with minimal changes occurring between approximately 800°C (1470°F) and 1400°C (2550°F). The rule of mixtures gives a good approximation of the SiC/RBSN modulus as function of temperature using the constituent moduli. In addition, Moulson's theory (1979) gives good results for predicting the modulus of the RBSN as a function of porosity. Exposing the specimens to high temperatures in air for up to four hours showed negligible changes in the composite modulus. More information is required for predicting composite modulus above

1400°C (2550°F) and for determining the secondary modulus just prior to fracture at all temperatures.

The characterization of the fiber/matrix interfacial shear strength requires further study. The first matrix cracking stress decreases above 600°C (1110°F) followed by a negligible change from approximately 800°C (1470°F) to 1400°C (2550°F). At 1550°C (2820°F) there is a decrease in the first matrix cracking stress. The ACK theory (1971), with the assumption of a frictional fiber/matrix interface, produces a good approximation for the SiC/RBSN composite first matrix cracking stress, although, the predictions are slightly conservative in this case. Ignoring the residual stresses produces better agreement with experimental results, indicating that the residual stresses are small in the SiC/RBSN composite. Oxidation of the interface, before first matrix cracking stress, at approximately 800°C (1470°F) is a significant problem due to porosity in the matrix. It reduces the first matrix cracking stress and the ultimate strength of the composite.

The first matrix cracking stress decreases with respect to time of exposure to air at temperatures from 600°C (1110°F) to 1400°C (2550°F) up to one hour. Negligible changes in first matrix cracking stress were noted from one hour to four hours of exposure at the same temperatures. Oxidation of the fiber/matrix interface takes place in the first hour of exposure to an oxidizing environment for loads below the first matrix cracking stress.

The ultimate strength of the SiC/RBSN composite showed a small change from room temperature to 600°C (1110°F) followed by a drop in strength at 800°C (1470°F). The significant drop in the ultimate strength at 800°C (1470°F) is attributed to the initiation of the oxidation of the fiber/matrix interface prior to the first matrix cracking stress. The ultimate strength increased slightly by 1000°C (1830°F) which was followed by a steady decline up to 1550°C (2820°F). The theory of Cao and Thouless (1990) showed excellent correlation from room temperature to 600°C (1110°F). At 1000°C (1830°F) and 1400°C (2550°F) the theory produces optimistic results, whereas, by 1550°C (2820°F) the prediction agrees closely with the experimental data. More SiC/RBSN composites and CVD SiC fibers need to be tested at 800°C (1470°F) due to significant discrepancies between theoretical predictions and experimental measurements induced by the oxidation of the fiber/matrix interface prior to the first matrix cracking stress.

Exposing the composites to air at temperatures between 600°C (1110°F) and 1400°C (2550°F) up to one hour reduced the ultimate strength. Exposure times between one hour and four hours showed a negligible change in the composite ultimate strength.

Modulus of toughness or the ability to sustain damage decreased as the test temperature was increased. The exception was a slight increase in the modulus of toughness from 800°C (1470°F) to 1000°C (1830°F). The specimen environment did not show an effect for the short term tests.

The enhanced SiC/SiC exhibited nonlinear stress/strain behavior from room temperature to 1370°C (2500°F) in air. Young's modulus decreased with increasing temperature up to 1090°C (2000°F) followed by a slight increase at 1370°C (2500°F). The theory of Yang and Chou (1989) with the assumption of a frictional fiber/matrix interface provides the best estimate of the composite Young's modulus. Further studies of the constituent materials are needed to improve the accuracy of the predictions.

The ultimate strength of the enhanced SiC/SiC did not change significantly from room temperature to 1090°C (2000°F). A slight decrease in ultimate strength was noted at 1370°C (2500°F). The theory of Cao and Thouless (1990) provided the best estimate of the ultimate strength of the enhanced SiC/SiC composite. It was assumed that only the longitudinal fibers carried the applied load at fracture of the composite.

The modulus of toughness increased with increasing test temperatures up to 1090°C (2000°F). This was followed by a decrease in the modulus of toughness at 1370°C (2500°F).

CHAPTER IX

FUTURE WORK

Now that the systems are fully operational it is desirable to expand and improve our testing capabilities. In addition, we need to reduce the cost of specimens by reducing their overall length. With experience and the availability of new equipment and instrumentation, the systems are being modified to handle specimens as short as 150 mm (6 in.).

The system for testing in air is being upgraded with new water cooled hydraulic grips mounted to a rigid load train and an induction heating system with a silicon carbide susceptor. With the new heating system, the system will be capable of thermal cycling to enhance the testing capability. A similar system has been used before at Lewis Research Center by Worthem and Lewinsohn (1991). The rigidly mounted grips will prevent cocking of the load

train when a crack in the specimen initiates from one of the edges effectively shifting the neutral axis of the coupon. In addition, the rigid load train allows limited compressive loading of the specimen. The hydraulic grips will provide a greater range in clamping force relative to the pneumatic grips used for these tests.

The system for testing in inert environments is being upgraded with a new furnace only. The furnace consists of new graphite elements with a shorter furnace jacket allowing the grips to be moved closer. The other components are left unchanged from the description provided in the equipment chapter.

High temperature tensile testing of ceramic matrix composites will continue as new material systems are being developed. More complex fiber architectures such as two and three dimensional weaves will be investigated. Melt infiltrated SiC/SiC is one of the composite systems which will be studied. Increased efforts to study the mechanical behavior of oxide composites will also be conducted.

The effects of notches and holes on the mechanical properties of ceramic matrix composites will be investigated. In addition, shear properties will be examined through the use of double notched tensile specimens and iosipescu shear specimens.

REFERENCES

Agarwal, B. D., and Broutman, L. J., Analysis and Performance of Fiber Composites. New York: John Wiley and Sons, Inc., 1980.

American Ceramic Society, "Technical Data," Ceramic Source 1991-1992, Vol. 7, 1991.

American Society for Testing and Materials, "ASTM Designation: C 1239-94a: Standard Practice for Reporting Uniaxial Strength Data and Estimating Weibull Distribution Parameters for Advanced Ceramics," 1995 Annual Book of ASTM Standards, Refractories; Carbon and Graphite Products; Activated Carbon; Advanced Ceramics. Vol. 15.01. ASTM, Philadelphia, PA.

American Society for Testing and Materials, "ASTM Designation: D 3039-76: Standard Test Method for Tensile Properties of Fiber-Resin Composites," 1992 Annual Book of ASTM Standards, Space Simulation; Aerospace and Aircraft; High Modulus Fibers and Composites. Vol. 15.03. ASTM, Philadelphia, PA.

American Society for Testing and Materials, "ASTM Designation: E 1012-93a: Standard Practice for Verification of Specimen Alignment Under Tensile Loading," 1993 Annual Book of ASTM Standards, Metals Test Methods and Analytical Procedures. Vol. 03.01. ASTM, Philadelphia, PA.

American Society for Testing and Materials, "ASTM Designation: C 20-74: Standard Methods of Test for Apparent Porosity, Water Absorption, Apparent Specific Gravity, and Bulk Density of Burned Refractory Brick," 1974 Annual Book of ASTM Standards, Part 17. ASTM, Philadelphia, PA.

Aveston, J., Cooper, G. A., and Kelly, A., "Single and Multiple Fracture in the Properties of Fiber Composites," Conference Proceedings, National Physical Laboratory, Guilford. IPC Science and Technology Press Ltd., Surrey, England, 1971, pp. 15-26.

Bansal, N. P., "$SrO{\bullet}Al_2O_3{\bullet}2SiO_2$ (SAS) Glass-Ceramic Matrix for Fiber-Reinforced Composites," Presented at the 5th Annual HITEMP

Review, Cleveland, OH, Oct., 1992. NASA Conference Publication 10104.

Bashford, D. P. and Raynal, R., "Testing and Integrity of Thermostructural Ceramic Matrix Composites," Proceedings ESA Symposium: Space Applications of Advanced Structural Materials, ESA SP-303, Jun., 1990.

Bergman, B., "On the Estimation of the Weibull Modulus," Journal of the Materials Science Letters, Vol. 3, 1984.

Bhatt, R. T., "Heat Treatment Effects on the Tensile Properties and Microstructures of a SiC/RBSN Composite in Nitrogen," NASA Technical Memorandum 106621, 1994.

Bhatt, R. T. and Hull, D. R., "Strength Degrading Mechanisms for CVD SCS-6 SiC Fibers in Argon Environments," NASA Technical Memorandum 107169, 1993.

Bhatt, R. T., "Oxidation Effects on the Mechanical Properties of a SiC-Fiber-Reinforced Reaction-Bonded Si_3N_4 Matrix Composite," Journal of the American Ceramic Society, Vol. 75, No. 2, 1992, pp. 406-412.

Bhatt, R. T., "Status of SiC Si_3N_4 Composites," Presented at 5th Annual HITEMP Review, Cleveland, OH, Oct., 1992. NASA Conference Publication 10104.

Bhatt, R. T., "Oxidation Effects On the Mechanical Properties of a SiC-Fiber-Reinforced Reaction-Bonded Si_3N_4 Matrix Composite," Journal of the American Ceramic Society, Vol. 75, No. 2, 1992.

Bhatt, R. T. and Phillips, R. E., "Laminate Behavior for SiC Fiber-Reinforced Reaction-Bonded Silicon Nitride Composites," Journal of Composites Technology and Research, Vol. 12, No. 1, Spring, 1990.

Bhatt, R. T., "Effect of Fabrication Conditions On the Properties of SiC Fiber Reinforced Reaction Bonded Silicon Nitride Matrix Composites (SiC/RBSN)," NASA Technical Memorandum 88814, 1986.

Bhatt, R. T., "Mechanical Properties of SiC Fiber Reinforced Reaction Bonded Si_3N_4 Composites," NASA Technical Memorandum 87085, 1985.

Budiansky, B., Hutchinson, J. W., and Evans, A. G., "Matrix Fracture In Fiber Reinforced Ceramics," Journal of the Mechanics and Physics of Solids, Vol. 34, 1986, pp. 167-189.

Cao, H. and Thouless, M. D., "Tensile Tests of Ceramic-Matrix Composites: Theory and Experiment," Journal of the American Ceramic Society, Vol. 73, No. 7, 1990.

Caputo, A. J., Stinton, D. P., Lowden, R. A., and Besmann, T. M., "Fiber Reinforced SiC Composites with Improved Mechanical Properties," American Ceramic Society Bulletin, Vol. 66, No. 2, 1987.

Castelli, M. G. and Lei, J., "A Comparison Between High Temperature Extensometry and PdCr Based Resistance Strain Gages with Multiple Application Techniques," Presented at the 7th Annual HITEMP Review, Cleveland, OH, Oct., 1994. NASA Conference Publication 10146.

Chawla. K. K., Ceramic Matrix Composites. London: Chapman and Hall, 1993.

Cho, C., Holmes, J. W., and Barber, J. R., "Distribution of Matrix Cracks In a Uniaxial Ceramic Composite," Journal of the American Ceramic Society, Vol. 75, No. 2, 1992, pp. 316-324.

Chou, T. W. and Ishikawa, T., "Analysis and Modeling of Two-Dimensional Fabric Composites," Textile Structural Composites, Composite Material Series, Vol. 3, ed. Chou, T. W. and Ko, F. K., Amsterdam: Elsevier Science Publishers B. V., 1989, pp. 209-277.

Chu, Y. C., Lavrentyev, A. I., Rokhlin, S. I., Baaklini, G. Y., Bhatt, R. T., "Ultrasonic Evaluation of Initiation and Development of Oxidation Damage in Ceramic-Matrix Composites," Journal of the American Ceramic Society, Vol. 78, No. 7, 1995, pp. 1809-1817.

Chu, Y. C., Rokhlin, S. I., and Baaklini, G. Y., "Ultrasonic Assessment of Interfacial Oxidation Damage in Ceramic Matrix Composites," Journal of Engineering Materials and Technology, Vol. 115, Jul., 1993, pp. 237-243.

Chulya, A., Gyekenyesi, J. P., and Bhatt, R. T., "Mechanical Behavior of Fiber Reinforced SiC/RBSN Ceramic Matrix Composites: Theory and Experiment," NASA Technical Memorandum 103688, 1991.

Constance, J., "Industry Turns to Ceramic Composites," Aerospace America, Mar., 1990.

Cox, B. N., Marshall, D. B., and Thouless, M. D., "Influence of Statistical Fiber Strength Distribution on Matrix Cracking in Fiber Composites," Acta Metallurgica, Vol. 37, No. 7, 1989, pp. 1933-1943.

Curtin, W. A., Eldridge, J. I., and Srinivasan, G. V., "New Silicon Carbide/Reaction Bonded Silicon Carbide Ceramic Matrix Composite," Journal of the American Ceramic Society, Vol. 76, No. 9, 1993.

Curtin, W. A., "Ultimate Strengths of Fibre-Reinforced Ceramics and Metals," Composites, Vol. 24, No. 2, 1993.

Dadkhah, M. S., Flintoff, J. G., Kniveton, T., and Cox, B. N., "Simple Models for Triaxially Braided Composites," Composites, Vol. 26, No. 8, 1995.

Dally, J. W., "Statistical Analysis of Experimental Data," Handbook On Experimental Mechanics, ed. Kobayashi, A. S., Society for Experimental Mechanics, Inc., 1993, pp. 1031-1054.

Danchaivijit, S. and Shetty, D. K., "Matrix Cracking In Ceramic-Matrix Composites," Journal of the American Ceramic Society, Vol. 76, No. 10, 1993.

Daniel, I. M., "Mechanical Testing: New Challenges," Advanced Materials Processes, Nov., 1989.

Daniel, I. M., Anastassopoulos, G., and Lee, J.-W., "The Behavior of Ceramic Matrix Fiber Composites Under Longitudinal Loading," Composite Science and Technology, Vol. 46, 1993, pp. 105-113.

Dev, S. P., "Emerging Technologies for Gas Turbine Engines: U.A.V. Synergies," American Institute of Aeronautics and Astronautics report AIAA-92-3757, 1992.

DiCarlo, J. A., Goldsby, J. C., Yun H. M., and Morscher, G. N., "Creep Strength-Grain Size Relationships For Polycrystalline Ceramic Fibers," HITEMP Review 1997, NASA Conference Publication 10192.

DiCarlo, J. A., "High Temperature Structural Fibers - Status and Needs," NASA Technical Memorandum 105174, 1991.

DiCarlo, J. A., "CMCs For the Long Run," Advanced Materials & Processes, Jun., 1989.

DiCarlo, J. A., "High Temperature Properties of CVD Silicon Carbide Fibers," Presented at the International Conference of Whisker- and Fiber-Toughened Ceramics, Jun. 7-9, 1988, Oak Ridge, TN.

DiCarlo, J. A., "Creep of Chemically Vapour Deposited SiC Fibres," Journal of Materials Science, Vol. 21, 1986.

DiCarlo, J. A., "Fibers for Structurally Reliable Metal and Ceramic Composites," Journal of Metals, Jun., 1985.

Dix, D. M. and Petty, J. S., "Aircraft Technology Gets A Second Wind," Aerospace America, Jul., 1990.

Drascovich, B. S., "Fibers for Turbines," CFCC News, Summer, 1993.

Duffy, S. F., Chulya, A., and Gyekenyesi, J. P., "Structural Design Methodologies for Ceramic-Based Material Systems," NASA Technical Memorandum 103097, 1991.

Duffy, S. F. and Gyekenyesi, J. P., "Reliability and Life Prediction of Ceramic Composite Structures at Elevated Temperatures," in High Temperature Mechanical Behavior of Ceramic Composites, S.V. Nair and K. Jakus, eds., pp. 471-515, Butterworth-Heinemann, Boston, 1995.

Eldridge, J. I., "Elevated Temperature Fiber Push-Out Testing," Mat. Res. Soc. Symp. Proc., Vol. 365, 1995, pp. 283-290.

Eldridge, J. I. and Ebihara, B. T., "Fiber Push-Out Testing Apparatus For Elevated Temperatures," Journal of Materials Research, Vol. 9, No. 4, Apr., 1994.

Eldridge, J. I., Bhatt, R. T., and Kiser, J. D., "Investigation of Interfacial Shear Strength In SiC/Si_3N_4 Composites," NASA Technical Memorandum 103739, 1991.

Eldridge, J. I. and Honecy, F. S., "Characterization of Interfacial Failure In SiC Reinforced Si_3N_4 Matrix Composite Material By Fiber Push-Out Testing and Auger Electron Spectroscopy," Journal of Vacuum Science and Technology, Vol. 8, 1990.

El-Rahaiby, S. K. and Solomon, A. A., "Tensile and Creep Testing of Fiber-Reinforced Ceramic Composites," CIAC Newsletter, Jun., 1992.

"Engineering Property Data On Selected Ceramics Volume 2, Carbides," Metals and Ceramics Information Center Report MCIC-HB-07, Vol. 2., Batelle Columbus Laboratories, Columbus, OH, 1979.

Evans, A. G., "The Mechanical Performance of Fiber-Reinforced Ceramic Matrix Composites," Materials Science and Engineering, A107, 1989.

Evans, A. G. and Marshall, D. B., "The Mechanical Behavior of Ceramic Matrix Composites," Acta Metallurgica, Vol. 37, No. 10, 1989, pp. 2567-2583.

Evans, A. G., Zok, F. W., and Mackin, T. J., "The Structural Performance of Ceramic Matrix Composites," High Temperature Mechanical Behavior of Ceramic Composites, ed. Nair, S. V. and Jakus, K., Boston: Butterworth-Heinemann, 1995, pp. 3-84.

Geoghegan, P. J., "Chemical Vapor Infiltrated Composites," Flight-Vehicle Materials, Structures, and Dynamics, Vol. 3: Ceramics and Ceramic-Matrix Composites, series ed. Noor, A. K. and Venneri, S. L., vol. ed. Levine, S. R., New York: The American Society of Mechanical Engineers, 1992, pp. 113-137.

Grande, D. H., "Testing and Properties of High Temperature Glass-Ceramic Matrix Composites," Ph.D. Thesis, Massachusetts Institute of Technology, 1987.

Grathwohl, G., "Current Testing Methods - A Critical Assessment," Mechanical Testing of Engineering Ceramics At High Temperatures, ed. Dyson, B. F., Lohr, R. D., and Morrell, R., London and New York: Elsevier Applied Science, 1989, pp. 30-50.

Gregory, O. J., Cooke, J. D., Olsen, C. R., Bourgery, M. A., and Bienkiewicz, J. M., "A Thin Film Ceramic Strain Gage For Use at High Temperature," HITEMP Review 1997, NASA Conference Publication 10192.

Gyekenyesi, J. Z. and Bartolotta, P. A., "An Evaluation of Strain Measuring Devices for Ceramic Composites," Journal of Testing and Evaluation, Jul., 1992.

Gyekenyesi, J. Z. and Hemann, J. H., "Optical Strain Measuring Techniques for High Temperature Tensile Testing," NASA Contractor Report 179637, 1987.

Gyekenyesi, J. Z. and Hemann, J. H., "High Temperature Tensile Testing of Ceramic Composites," NASA Contractor Report 180888, 1988.

Hahn, H. T. and Pandey, R., "Micromechanics Models For Thermoelastic Properties of Woven Fabric Composites," Prepared for the Office of Industrial Technology, Oak Ridge National Laboratory, Contract No. 11XSF881C, Aug., 1992.

Halpin, J. C. and Tsai, S. W., "Effects of Environmental Factors On Composite Materials," AFML-TR 67-423, Jun., 1969.

Hartman, G. A., Zawada, L. P., and Russ, S. M., "Techniques for Elevated Temperature Testing of Advanced Ceramic Composite Materials," Proceedings of the 5th Annual Hostile Environments and High Temperature Measurements Conference, 1988.

Hercher, M., Wyntjes, G., and DeWeerd, H., "Non-Contact Laser Extensometer," Proceedings of SPIE - The International Society for Optical Engineering, Industrial Laser Interferometry, Jan., 1987

Hill, R. and Okoroafor, E. U., "Weibull Statistics Of Fibre Bundle Failure Using Mechanical and Acoustic Emission Testing: The Influence of Interfibre Friction," Composites, Vol. 26, No. 10, 1995.

Hilmas, G. E., Holmes, J. W., Bhatt, R. T., and DiCarlo, J. A., "Tensile Creep and Creep Recovery Behavior of Unidirectional Reinforced SCS-6 SiC_f/RBSN Composites," HITEMP Review 1993, NASA Conference Publication 19117.

Hirano, K., "Some Problems of Technology Advanced Structural Materials Testing, Evaluation of Ultrahigh Temperature," Science & Technology, Japan, JPRS report JPRS-JST-92-023, 1992.

Holmes, J. W. and Chermant, J. L., "Creep Behavior of Fiber-Reinforced Ceramic Matrix Composites," High Temperature Ceramic Matrix Composites, Woodhead Publishing Limited, England, 1993.

Holmes, J. W., Jones, J. W., and Bhatt, R. T., "Tensile Creep Behavior of SCS-6 SiC-Fiber Si3N4-Matrix Composites," Presented at 5th Annual HITEMP Review, Cleveland, OH, Oct., 1992. NASA Conference Publication 10104.

Holmes, J. W. and Cho, C., "Experimental Observations of Frictional Heating in Fiber-Reinforced Ceramics," Journal of the American Ceramic Society, Vol. 75, No. 4, 1992.

Holmes, J.W. and Wu, X., "Elevated Temperature Creep Behavior of Continuous Fiber-Reinforced Ceramics," in High Temperature Mechanical Behavior of Ceramic Composites, ed. Nair, S. V. and Jakus, K., pp. 193-259, Butterworth-Heinemann, Boston, 1995.

Hosford, W. F. "Overview of Tensile Testing," Tensile Testing. ed. Han, P., ASM International, 1992.

Hsueh, C. H., "Toughening Behavior and Interfacial Properties of Fiber-Reinforced Ceramic Composites," Composite Material Technology 1990; Proceedings of the Symposium, 13th ASME Annual Energy-Sources Technology Conference and Exhibition, New Orleans, LA, Jan. 14-18,1990. New York, American Society of Mechanical Engineers, 1990, pp. 119-126.

Hsueh, C. H., "Elastic Load Transfer from Partially Embedded Axially Loaded Fiber to Matrix," Journal of Materials Science Letters, Vol. 7, No. 5, 1988, pp. 497-500.

Huddleston, R., "Oak Ridge Presentation," High Temperature Testing of Carbon-Carbon and Ceramic Matrix Composites. ed. Kearns, T. F., Institute for Defense Analyses, IDA Memorandum Report M-278, Dec., 1986.

Hurwitz, F. I., "Polymeric Approaches to SiC and Silicon Oxycarbide Ceramic Matrix Composites: An Update," Presented at the 3rd Annual HITEMP Review, Cleveland, OH, Oct., 1990. NASA Conference Publication 10051.

Inghels, E. and Lamon, J., "An Approach to the Mechanical Behavior of SiC/SiC and C/SiC Ceramic Matrix Composites," Journal of Materials Science, Vol. 26, 1991, pp. 5403-5410.

Jablonski, D. A. and Bhatt, R. T., "High Temperature Tensile Properties of Fiber Reinforced Reaction Bonded Silicon Nitride," Journal of Composites Technology & Research, Vol. 12, No. 3, Fall, 1990, pp. 139-146.

Jamet. J. F., "State of the Art and Future Prospects for High Temperature Composites," European Conference on Composite Materials Proceedings. London. Elsevier Applied Science, 1989, pp. 5-13.

Jaskowiak, M. J. and Setlock, J. A., "Processing and Mechanical Properties of Sapphire Reinforced Alumina Matrix Composites," Presented at the 7th Annual HITEMP Review, Cleveland, OH, Oct., 1994. NASA Conference Publication 10146.

Jenkins, M. G., "Long-Term Testing of Advanced Ceramics: Concerns, Insights, and Recommendations," Presented at the International Gas Turbine and Aeroengine Congress and Exposition, Houston, TX Jun. 5-8, 1995.

Jenkins, M. G., "Ceramic Crack Growth Resistance Determination Utilizing Laser Interferometry," Ph.D. Thesis, The University of Washington, 1987.

Jones, M. H. and Brown Jr., W. F., "An Axial Loading Creep Machine," ASTM Bulletin, No. 211, Jan. 1956.

Kerans, R. J., Hay, R. S., Pagano, N. J., Parthasarathy, T. A., "The Role of the Fiber-Matrix Interface in Ceramic Composites," Ceramic Bulletin, Vol. 68, No. 2, 1989.

Kimber, A. C. and Keer, J. G., "On the Theoretical Average Crack Spacing In Brittle Matrix Composites Containing Continuous Aligned Fibers," Journal of Materials Science Letters, Vol. 1, 1982.

King, J. E., "Failure In Composite Materials," Metals and Materials, Dec., 1989.

Kotil, T., "Ceramic Composites: Experimental and Analytical Study of Silicon Nitride Composites," Ann Arbor, Michigan: University Microfilms International, 1992.

Larsen, C. G., Johnson, L. E., and Mosiman, L. G., "Gripping Techniques and Concerns for Mechanical Testing of Ultra-High Temperature Materials," MTS Systems Corporation, Eden Prairie, MN, 1993.

Levine, S. R., "Ceramics and Ceramic Matrix Composites - Aerospace Potential and Status," American Institute of Aeronautics and Astronautics report AIAA-92-2445-CP, 1992.

Lewis III, D., "Tensile Testing of Ceramics and Ceramic-Matrix Composites," Tensile Testing, ed. Patricia Han. Ohio: ASM International, 1992.

Mah, T., Mendiratta, M. G., Katz, A. P., Ruh, R., and Mazdiyasni, K. S., "High-Temperature Mechanical Behavior of Fiber-Reinforced Glass-Ceramic-Matrix Composites," Journal of the American Ceramic Society, Vol. 68, No. 9, 1985.

Mandell, J. F. and Grande, D. H., "Structural Characterization of High Temperature Composites," NASA Contractor Report 187220, 1991.

Martin, J. F. and Schultz, B. E., "Closed-Loop Strain Controlled Testing at Elevated Temperatures with a Non-Contacting Gage," Instrumentation In the Aerospace Industry, Vol. 29, Instrument Society of America, 1983, pp. 237-240.

Marshall, D. B. and Cox, B. N., "A J-Integral Method for Calculating Steady-State Matrix Cracking Stresses In Composites," Mechanics of Materials, Vol. 7, 1988, pp. 127-133.

Masters, J. E., Foye, R. L., Pastore, C. M., and Gowayed, Y. A., "Mechanical Properties Of Triaxially Braided Composites: Experimental and Analytical Results," NASA Contractor Report 189572, Jan., 1992.

"Materials Selector 1988," Materials Engineering, Dec. 1987.

McCartney, L. N., "Mechanics of Matrix Cracking in Brittle-Matrix Fiber-Reinforced Composites," Royal Society of London, Proceedings, Series A, Vol. 409, 1987, pp. 329-350.

Mettler Instruments AG, "Density Determination Kit," Mettler ME-40290, 1981.

Mital, S. K., Murthy, P. L. N., and Chamis, C. C., "Simplified Micromechanics of Plain Weave Composites," NASA Technical Memorandum 107165, Mar., 1996.

Morscher, G. N., Lewinsohn, C. A., Bakis, C. E., Tressler, R. E., and Wagner, T., "Comparison of Bend Stress Relaxation and Tensile Creep of CVD SiC Fibers," Journal of the American Ceramic Society, Vol. 78, No. 12, 1995, pp. 3244-3252.

Morscher, G. N., Martinez-Fernandez, J., and Purdy, M. J., "Determination of Interfacial Properties Using a Single Fiber Microcomposite Test,"

Presented at the 96th Annual American Ceramic Society Meeting, Apr. 24-27, 1994, Indianapolis, IN.

Morscher, G. N. and DiCarlo, J. A., "A Simple Test for Thermomechanical Evaluation of Ceramic Fibers," NASA Technical Memorandum 103767, 1991.

Moschler, J. W., "Investigation of Failure Modes In Fiber Reinforced Ceramic Matrix Composites," Master's Thesis, Air Force Institute of Technology, Air University, 1988.

Moulson, A. J., "Review Reaction-Bonded Silicon Nitride: Its Formation and Properties," Journal of Materials Science, Vol. 14, 1979.

Nair, S. V., Gwo, T., Narbut, N. M., Kohl, J. G., and Sundberg, G. J., "Mechanical Behavior of a Continuous-SiC-Fiber-Reinforced RBSN-Matrix Composite," Journal of the American Ceramic Society, Vol. 74, No. 10., 1991.

Ng, D., Fralik, G., and Lei, J., "Temperature Measurement of Ceramic Materials and Thermal Barrier Coatings Using a Multiwavelength Pyrometer," HITEMP Review 1997, NASA Conference Publication 10192.

Ning, X. J., and Pirouz, P., "The Microstructure of SCS-6 SiC Fiber," Journal of Materials Research, Vol. 6, No. 10, Oct., 1991.

Pagano, N. J. and Dharani, L. R., "Failure Modes in Unidirectional Brittle Matrix Composites (BMC)," Ceramic Engineering and Science Proceedings, Vol. 8, Nos. 7-8, 1987, pp. 626-629.

Pai, S. S. and Gyekenyesi, J. P., "Calculation of Weibull Strength Parameters and Batdorf Flaw-Density Constants for Volume- and Surface-Flaw-Induced Fracture in Ceramics," NASA Technical Memorandum 100890, 1988.

Prewo, K. M., "Tension and Flexural Strength of Silicon Carbide Fibre-Reinforced Glass Ceramics," Journal of Materials Science, Vol. 21, 1986, pp. 3590-3600.

Pysher, D. J., Goretta, K. C., Hodder Jr., R. S., and Tressler, R. E., "Strengths of Ceramic Fibers at Elevated Temperatures," Journal of the American Ceramic Society, Vol. 72, No. 2, 1989, pp. 284-288.

Quin, G., "ASTM Committee C-28, Advanced Ceramics - A Progress Report," American Ceramic Society Bulletin, Vol. 71, No. 10, Oct., 1992.

Sayir, A., "Growth and Characterization of Directionally Solidified $Al_2O_3/Y_3Al_5O_{12}$ (YAG) Eutectic Fibers," Presented at the 4th Annual HITEMP Review, Cleveland, OH, Oct., 1991. NASA Conference Publication 10082.

Sayir, A., Dickerson, R. M., Yun, H., Heidger, S., and Matson, L. E., "High Temperature Mechanical Properties of Directionally Solidified $Al_2O_3/Y_3Al_5O_{12}$ (YAG) Eutectic Fibers," Presented at the 7th Annual HITEMP Review, Cleveland, OH, Oct., 1994. NASA Conference Publication 10146.

Sayir, A., Greer III, L. C., Goldsby, J. C., Oberle, L. G., "Laser Speckle Micro-Strain Measurements On Small Diameter Fibers," Ceramic Engineering and Science Proceedings, Jul.-Aug., 1994.

Shapiro, S. S., "Selection, Fitting, and Testing Statistical Models," Statistical Methods for Engineers and Scientists, ed. H. M. Wadsworth, pp.6.1-6.34, McGraw-Hill Publishing Co., New York, 1990.

Sheppard, L. M., "Enhancing Performance of Ceramic Composites," Ceramic Bulletin, Vol. 71, No. 4, 1992.

Shimansky, R. A., "Effect of Interfaces On Continuous Fiber-Reinforced Brittle Matrix Composites," Ann Arbor, Michigan: University Microfilms International, 1989.

Sims, C. T., "Non Metallic Materials for Gas Turbine Engines: Are They Real?" Advanced Materials and Processes, Jun., 1991.

Singh, M. and Levine, S. R., "Low Cost Fabrication of Silicon Carbide Based Ceramics and Fiber Reinforced Composites," NASA Technical Memorandum 107001, 1994.

Starrett, S., "A Test Method for Tensile Testing Coated Carbon-Carbon and Ceramic Matrix Composites at Elevated Temperature in Air," Ceramic Engineering and Science Proceedings, Sep.-Oct., 1990.

Starrett, H. S., "High Temperature Test Methods," Presented at Composites Testing Methodology Workshop, Feb. 8, 1990, National Institute of Standards and Technology, Gaithersburg, Maryland.

Starrett, H. S., "High Temperature Tensile Testing in Air," Inter Agency Planning Group Meeting at the Institute for Defense Analysis, Alexandria, Virginia, Nov. 12, 1986.

Steen, M. and Bressers, J., "A Facility For Uniaxial Testing of CMCs At High Temperatures," High Temperature Chemical Processes. Vol. 3, 1994.

Studt, T., "Breaking Down Barriers for Ceramic Matrix Composites," R&D Magazine, Aug., 1991.

Sumner, G., "Heating Methods and Grips," Techniques for High Temperature Fatigue Testing. London and New York: Elsevier Applied Science Publishers, 1985, pp. 71-96.

Swanson, S. R. and Smith, L. V., "Comparison of the Biaxial Strength Properties of Braided and Laminated Carbon Fiber Composites," Composites Part B, Vol. 27B, No. 1, 1996.

Takeda, M., Imai, Y., Ichikawa, H., Ishikawa, T., Kasai, N., Suguchi, T., and Okamura, K., "Thermal Stability of the Low Oxygen Silicon Carbide Fibers Derived From Polycarbosilane," Ceramic Engineering and Science Proceedings, Vol. 13, Nos. 7-8, 1992.

Tarnopol'skii, Yu. M. and Kincis, T., "State of the Art In Mechanical Testing of Composites," International Conference On Composite Materials Proceedings, Vol. 1. London and New York, Elsevier Applied Science, 1987, pp. 1.260-1.268.

Taylor, R., "Ceramic Fiber/Ceramic Matrix Composites - Why and How?" SAMPE Journal, Vol. 27, No. 4, Jul./Aug., 1991.

Tripp, D. E., Hemann, J. H., and Gyekenyesi, J. P., "A Review of Failure Models for Unidirectional Ceramic Matrix Composites Under Monotonic Loads," NASA Technical Memorandum 101421, 1989.

Tuma, M., Krasowski, M., Greer, L., Oberle, L., Elam, K., Spina, D., "Tow-Color Laser Speckle Shift Strain Measurement System," HITEMP Review 1997, NASA Conference Publication 10192.

Verrilli, M. J., Calamino, A. M., and Brewer, D. N., "Creep-Rupture Behavior of a SiC/SiC Composite," Thermal and Mechanical Test Methods and Behavior of Continuous Fiber Ceramic Composites, ASTM STP 1309, M. G. Jenkins, S. T. Gonczy, E. Lara-Curzio, N. E. Ashbaugh, and L. P. Zawada, eds, American Society for Testing and Materials, 1996.

Wang, S., "Processing and Characterization of Continuous Fiber-Reinforced Glass-Ceramic Matrix Composites," Ph.D. Dissertation, University of Delaware, 1990.

Warren, R., "Overview," Ceramic-Matrix Composites. ed. R. Warren. New York: Chapman and Hall, 1992. p.5

Weibull, W., "The Phenomenon of Rupture in Solids," Ingeniors Ventenskaps Akademien Handlinger, No. 153, 1939, pp. 5-55.

Wiederhorn, S. M., Carroll, D. F., Chuang, T. -J., and Roberts, D. E., "Standard Tensile Test Development," Ceramic Technology for Advanced Heat Engines Project Semiannual Progress Report for April Through September 1988. Oak Ridge National Laboratory report ORNL/TM-11116.

Woodford, D. A., Van Steele, D. R., Brehm, J. A., Timms, L. A., and Palko, J. E., "Testing the Tensile Properties of Ceramic-Matrix Composites," JOM, May, 1993.

Worthem, D. W., "Improved Flat Specimens for Tensile and Fatigue Testing of Composites," NASA Tech Briefs, Vol. 18, No.11, Nov., 1994.

Worthem, D. W., "Thermomechanical Fatigue Behavior of Coated and Uncoated Enhanced SiC/SiC," Presented at the 7th Annual HITEMP Review, Cleveland, OH, Oct., 1994. NASA Conference Publication 10146.

Worthem, D. W. and Lewinsohn, "Effect of Specimen Design on the Tensile Properties of Ceramic Matrix Composites," Presented at the 4th Annual HITEMP Review, Cleveland, OH, Oct., 1991. NASA Conference Publication 10082.

Worthem, D. W., "Flat Tensile Specimen Design for Advanced Composites," NASA Contractor Report 185261, 1990.

Yang, T. and Chou, T., "Thermo-Elastic Analysis of Triaxial Woven Fabric Composites," Textile Structural Composites, ed. Chou, T. and Ko, F. K., New York: Elsevier Science Publishing Company Inc., 1989, pp. 265-277.

Yang, X. F. and Knowles, K. M., "The One-Dimensional Car Parking Problem and Its Application to the Distribution of Spacings Between Matrix

Cracks In Unidirectional Fiber-Reinforced Brittle Materials," Journal of the American Ceramic Society, Vol. 75, No. 1, 1992, pp. 141 147.

Yoshida, M. and Kokaji, A., "Firing Up the Future with Ceramic Engine Parts," Machine Design, Oct. 26, 1989.

APPENDIX

APPENDIX A

DERIVATION OF THE EQUATION FOR DETERMINING INTERFACIAL SHEAR STRENGTH

In this section the equation for calculating the interfacial shear stress from the periodic matrix crack spacing is derived. Figure 54a shows a fiber within a matrix with a load applied to the fiber. The fiber transfers a portion of the load to the matrix through the interfacial shear stress. First, it is assumed that the fiber failure stress and strain are greater than the matrix failure stress and strain, respectively. Another condition that must be met, to get multiple matrix cracks, is that the fibers must be able to carry the applied load once the matrix has a through crack. These conditions are shown by the following inequalities:

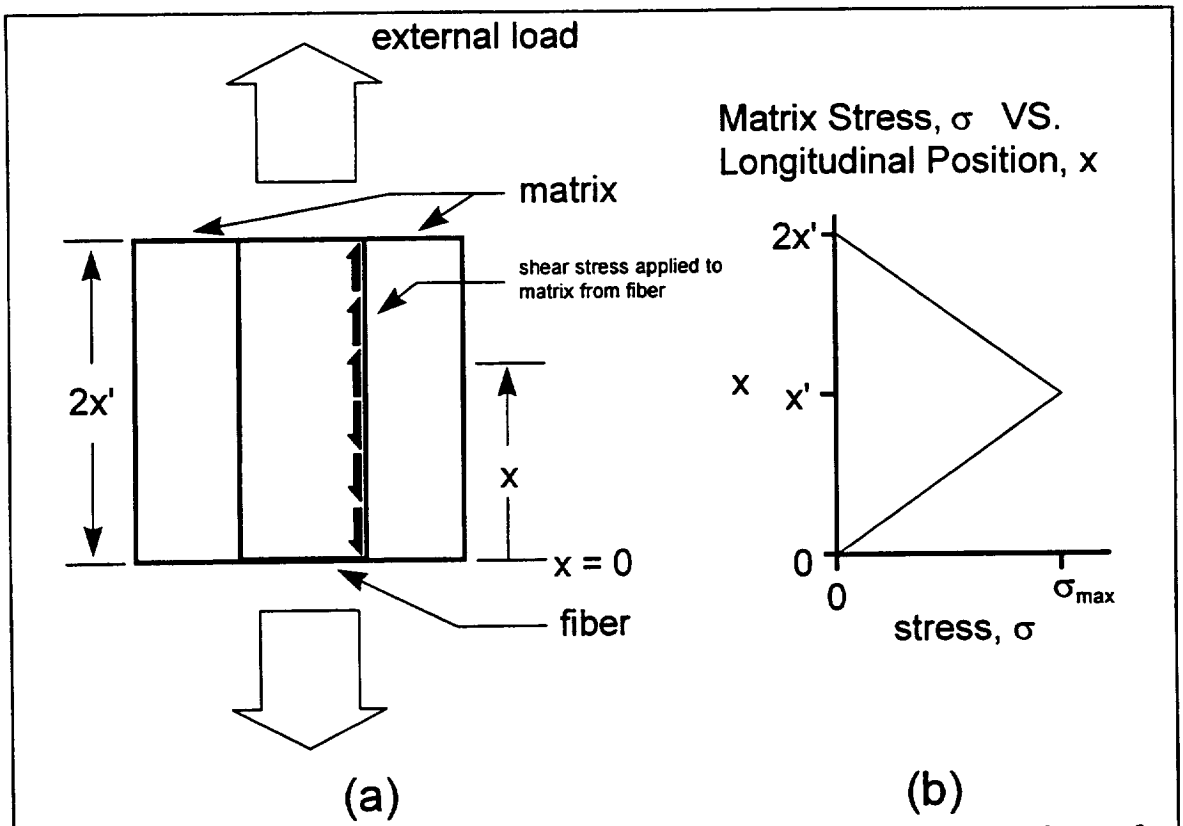

Figure 54. a) Schematic of fiber in matrix showing load transfer from the fiber to the matrix. b) Matrix stress as a function of longitudinal displacement.

$$\sigma_{fu} > \sigma_{mu} \tag{A.1}$$

$$\varepsilon_{fu} > \varepsilon_{mu} \tag{A.2}$$

$$\sigma'_f V_f + \sigma_{mu} V_m < \sigma_{fu} V_f \tag{A.3}$$

where

σ_{fu} - fiber ultimate strength

σ_{mu} - matrix ultimate strength

ε_{fu} - strain in fiber at fiber ultimate strength

ε_{mu} - strain in matrix at matrix ultimate strength

σ'_f - fiber stress just before matrix cracking

V_f - fiber volume fraction

V_m - matrix volume fraction

The above conditions will result in multiple matrix cracking as the composite is loaded to the ultimate strength. The matrix will be fractured into lengths between x' and 2x'. It should be noted that the SiC fibers have a round cross section with a radius, R. A constant interfacial shear stress is assumed which results in a linear matrix stress distribution as a function of longitudinal position. This is illustrated in Figure 54b. A constant value for the ultimate strength of the matrix is assumed also.

Summing forces within the matrix, we have:

$$\Sigma F = 0 = N\tau(2\pi R)x' - \sigma_{mu}V_m \qquad (A.4)$$

where:

N = number of fibers per unit area = $\frac{V_f}{\pi R^2}$

τ = interfacial shear stress

R = fiber radius

Solving for the distance between matrix cracks, we have:

$$x' = \frac{V_m \sigma_{mu}}{N(2\pi R)\tau} \tag{A.5}$$

$$x' = \frac{V_m \sigma_{mu} R}{V_f 2\tau} \tag{A.6}$$

The above equation was first presented in Aveston, et al. (1971). Kimber and Keer (1982) have shown analytically that the average matrix crack spacing was closer to 1.337x'. So, the equation for calculating the matrix crack spacing is:

$$x' = \frac{\beta V_m \sigma_{mu} R}{V_f 2\,\tau} \tag{A.7}$$

where: $\beta = 1.337$

Solving for the interfacial shear stress, we have:

$$\tau = \frac{\beta V_m \sigma_{mu} R}{V_f 2x'} \tag{A.8}$$

Equation A.8 can be reformulated in terms of the composite stress, σ_y. It is assumed that the strain in the constituents is the same as the strain in the composite, that is

$$\varepsilon_f = \varepsilon_m = \varepsilon_c \tag{A.9}$$

Substituting Hooke's law into equation A.9 for the matrix and composite strains, we have

$$\frac{\sigma_m}{E_m} = \frac{\sigma_c}{E_c} \tag{A.10}$$

$$\sigma_m = \frac{E_m}{E_c}\sigma_c \tag{A.11}$$

The composite first matrix cracking stress, σ_y, is assumed to take place when the matrix stress, σ_m, reaches the ultimate strength of the matrix material, σ_{mu}, that is

$$\sigma_m = \sigma_{mu} \text{ and } \sigma_c = \sigma_y$$

As a result, we have

$$\tau = \frac{\beta V_m E_m \sigma_y R}{2 V_f E_c x'} \qquad \text{(A.12)}$$

APPENDIX B

DERIVATION OF THE ACK THEORY

Aveston, Cooper, and Kelly (1971) derived an equation for predicting the first matrix cracking stress in a brittle matrix composite. This is commonly referred to as the ACK theory. It was derived using an energy balance approach. They calculated the change in energy states within the composite, which occurred upon matrix cracking leaving only the bridging fibers to carry the total load.

Following is a detailed derivation which includes the assumptions made that also describe the SiC/RBSN composite. A weak fiber/matrix interface with a constant shear stress is assumed to exist. An isostrain condition is enforced within the composite, that is, the strain in the fiber and the matrix is assumed to be the same, before the first matrix crack initiates. A slip zone at the

fiber/matrix interface is introduced near the crack face once the first matrix crack occurs. This results in a linear stress distribution within the matrix and the fibers near the crack face. Outside of the slip zone the isostrain condition remains. In addition, a fixed value is assumed for the matrix ultimate strain. The following inequalities have to be satisfied:

$$\sigma_{fu} > \sigma_{mu} \tag{B.1}$$

$$\varepsilon_{fu} > \varepsilon_{mu} \tag{B.2}$$

$$\sigma'_f V_f + \sigma_{mu} V_m < \sigma_{fu} V_f \tag{B.3}$$

where:

σ_{fu} - fiber ultimate strength

σ_{mu} - matrix ultimate strength

ε_{fu} - strain in fiber at fiber ultimate strength

ε_{mu} - strain in matrix at matrix ultimate strength

σ'_f - fiber stress just before matrix cracking

V_f - fiber volume fraction

V_m - matrix volume fraction

These conditions will allow the fibers to carry the load in the composite once matrix cracking has initiated. The fibers bridge the matrix cracks.

First, the change in stress state within the fiber and the matrix upon matrix cracking will be determined. Initially, the stresses within the composite are carried by the fibers and the matrix as shown by equation B.4 which is the rule of mixtures.

$$\sigma_c = \sigma_m V_m + \sigma_f V_f \tag{B.4}$$

where:

σ_c - the composite stress

σ_f - the stress in the fiber

σ_m - the stress in the matrix

From equation B.4 the additional stress imposed on the fibers upon matrix cracking at the matrix crack plane can be determined. Solving for σ_f then differentiating yields:

$$\sigma_f = \frac{1}{V_f}\left[\sigma_c - V_m \sigma_m\right]$$

$$d\sigma_f = -\frac{V_m}{V_f} d\sigma_m \tag{B.5}$$

The composite stress, σ_c, is taken to be constant as cracking occurs. At the crack face the stress in the matrix changes from σ_{mu} just prior to matrix cracking to zero just after matrix cracking. As a result, the change in the matrix stress, $d\sigma_m$, is:

$$d\sigma_m = -\sigma_{mu} \tag{B.6}$$

Equation B.6 is substituted into equation B.5 to find the change in fiber stress.

$$d\sigma_f = \frac{V_m}{V_f} \sigma_{mu} \tag{B.7}$$

Figure 55 shows a section of the composite with the cracked matrix. A plot of the stress within the fiber with respect to the distance from the crack plane is illustrated also. The distance x' is derived in Appendix A, using a shear-lag model, and is given by equation A.6 and repeated here.

$$x' = \frac{V_m \sigma_{mu} R}{V_f 2\tau} \tag{B.8}$$

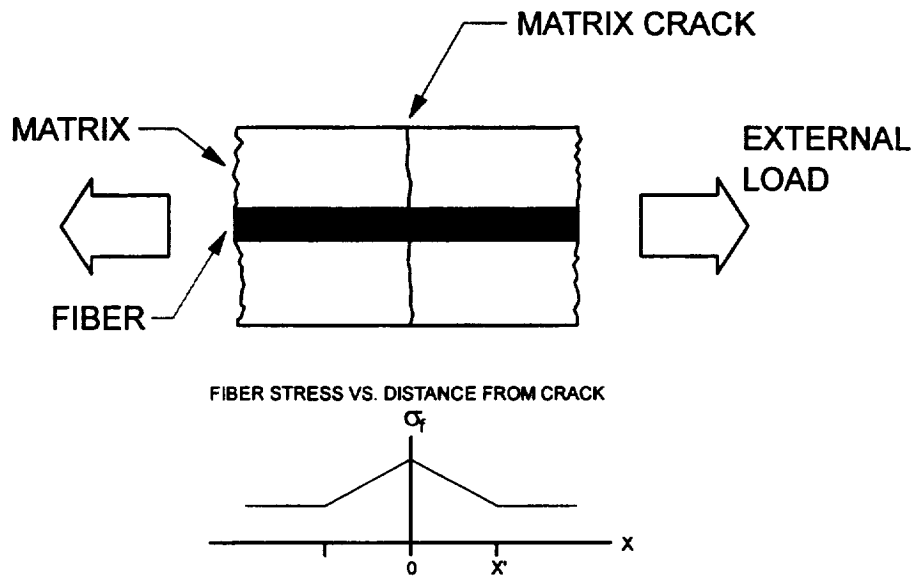

Figure 55. A section of the composite with a crack in the matrix and the corresponding stress distribution within the fiber is illustrated.

where:

R - fiber radius

τ - interfacial shear stress

The following material constant, a, will be used to simplify the equations throughout the rest of this section:

$$a = \frac{E_m V_m}{E_f V_f} \tag{B.9}$$

where:

E_f - Young's modulus of the fiber

E_m - Young's modulus of the matrix

Looking at Figure 55 the boundary conditions upon matrix cracking are:

at x=0 one has,

$$\Delta\sigma_f = \sigma_{mu}\frac{V_m}{V_f} \text{ and } \Delta\varepsilon_f = \frac{1}{E_f}\Delta\sigma_f = \frac{1}{E_f}\frac{V_m}{V_f}\sigma_{mu} = \frac{E_m V_m}{E_f V_f}\varepsilon_{mu} = a\varepsilon_{mu}$$

at x=x' one has,

$\Delta\sigma_f = 0$ and $\Delta\varepsilon_f = 0$

The additional mean strain, upon matrix cracking, in the fiber between x=0 and x=x' is

$$\Delta\varepsilon_{f_{mean}} = \frac{1}{2}a\varepsilon_{mu} \qquad \text{(B.10)}$$

The Young's modulus of the composite is determined by the rule of mixtures, that is

$$E_c = E_m V_m + E_f V_f = E_f V_f(1+a) \qquad \text{(B.11)}$$

where

E_c - Young's modulus of the composite

Next, the work done per unit area by the applied load upon matrix cracking is determined. The increase in composite length occurs over the length, 2x'. The coordinates are defined in Figure 55.

$$\Delta W = 2\int_0^{x'} \sigma_c \Delta\varepsilon_{f_{mean}} dx$$

$$\Delta W = 2\sigma_c \Delta\varepsilon_{f_{mean}} x'$$

$$\Delta W = 2\sigma_c \left(\frac{1}{2} a\varepsilon_{mu}\right)\left(\frac{V_m \sigma_{mu} R}{V_f 2\tau}\right)$$

$$\Delta W = 2(E_c \varepsilon_c)\left(\frac{1}{2} a\varepsilon_{mu}\right)\left(\frac{V_m E_m \varepsilon_{mu} R}{V_f 2\tau}\right)$$

Using the isostrain condition at matrix cracking, that is $\varepsilon_c = \varepsilon_{mu}$, we obtain

$$\Delta W = 2\left[E_f V_f (1+a)\,\varepsilon_{mu}\right]\left(\frac{1}{2} a\varepsilon_{mu}\right)\left(\frac{V_m E_m \varepsilon_{mu} R}{V_f 2\tau}\right)$$

$$\Delta W = \frac{E_f E_m V_f}{2\tau} \varepsilon_{mu}^3 Ra(1+a) \qquad \text{(B.12)}$$

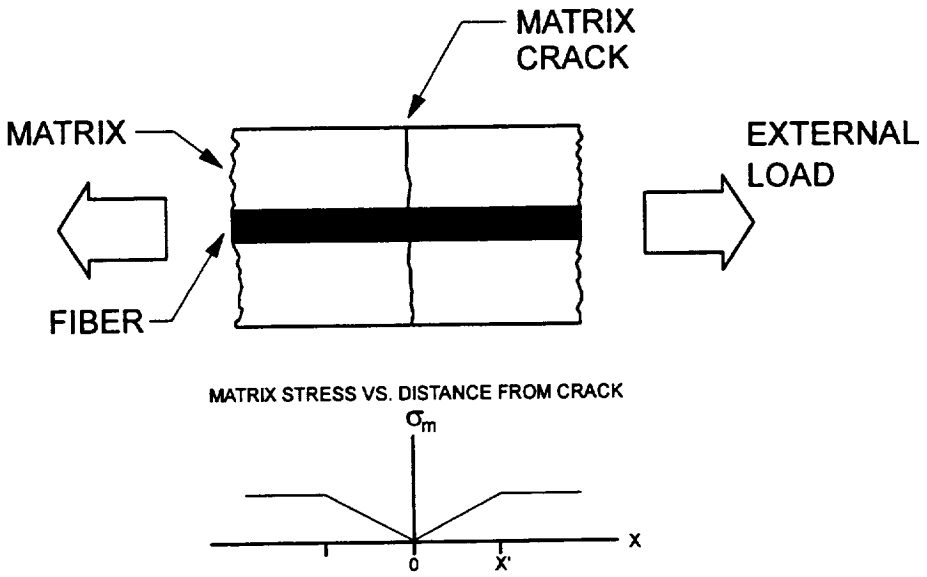

Figure 56. A section of the composite with a crack in the matrix with the corresponding stress distribution within the matrix is illustrated.

The change in energy per unit area within the matrix, due to the unloading at the crack face, is determined. Figure 56 shows the stress distribution within the matrix relative to the crack plane.

Looking at Figure 56 one has the following boundary conditions:

at $x=0$ one has, $\sigma_m=0$ and $\varepsilon_m=0$

at $x=x'$ one has, $\sigma_m=\sigma_{mu}$ and $\varepsilon_m=\varepsilon_{mu}$

The change in energy per unit area, upon matrix cracking, within the matrix is:

$$\Delta U_m = 2\int_0^{x'}\left[\frac{1}{2}\left(V_m\sigma_{mu}\frac{x}{x'}\right)(\varepsilon_{mu}) - \frac{1}{2}(V_m\sigma_{mu})\,\varepsilon_{mu}\right]dx$$

$$\Delta U_m = 2\int_0^{x'}\left[\frac{1}{2}V_mE_m\left(\varepsilon_{mu}\frac{x}{x'}\right)^2 - \frac{1}{2}V_mE_m\varepsilon_{mu}^2\right]dx$$

$$\Delta U_m = 2\left[\frac{1}{6}V_mE_m\varepsilon_{mu}^2\frac{x^3}{(x')^2} - \frac{1}{2}V_mE_m\varepsilon_{mu}^2x\right]_0^{x'}$$

$$\Delta U_m = 2\left[\frac{1}{6}V_mE_m\varepsilon_{mu}^2x' - \frac{1}{2}V_mE_m\varepsilon_{mu}^2x'\right]$$

$$\Delta U_m = -\frac{2}{3}V_mE_m\varepsilon_{mu}^2x'$$

$$\Delta U_m = -\frac{2}{3}V_mE_m\varepsilon_{mu}^2\left(\frac{V_mE_m\varepsilon_{mu}R}{V_f2\tau}\right)$$

$$\Delta U_m = -\frac{E_mV_mE_f}{3\tau}a\varepsilon_{mu}^3R$$

$$\Delta U_m = -\frac{E_fE_mV_m}{3\tau}\varepsilon_{mu}^3aR \qquad \text{(B.13)}$$

Next, the change in energy per unit area, upon matrix cracking, within the fibers is determined. Observing Figure 55, one has the following boundary conditions:

at x=0 one has,

$$\Delta\sigma_f = \sigma_{mu}\frac{V_m}{V_f} \text{ and } \Delta\varepsilon_f = a\varepsilon_{mu}$$

at x=x' one has,

$\Delta\sigma_f=0$ and $\Delta\varepsilon_f=0$

The change in energy per unit area within the fiber is:

$$\Delta U_f = 2\int_0^{x'}\left\{\frac{1}{2}V_f\left[\sigma_f+\Delta\sigma_f(x)\right]\left[\varepsilon_f+\Delta\varepsilon_f(x)\right] - \frac{1}{2}V_f\sigma_f\varepsilon_f\right\}dx$$

$$\Delta U_f = 2\int_0^{x'}\left\{\frac{1}{2}V_f\left[\sigma_f+\sigma_{mu}\frac{V_m}{V_f}\left(1-\frac{x}{x'}\right)\right]\left[\varepsilon_f+a\varepsilon_{mu}\left(1-\frac{x}{x'}\right)\right] - \frac{1}{2}V_fE_f\varepsilon_{mu}^2\right\}dx$$

$$\Delta U_f = 2\int_0^{x'}\left\{\frac{1}{2}V_f\varepsilon_{mu}^2E_f\left[1+\frac{E_mV_m}{E_fV_f}\left(1-\frac{x}{x'}\right)\right]\left[1+a\left(1-\frac{x}{x'}\right)\right] - \frac{1}{2}V_fE_f\varepsilon_{mu}^2\right\}dx$$

$$\Delta U_f = 2\int_0^{x'}\left\{\frac{1}{2}V_f\varepsilon_{mu}^2E_f\left[1+a\left(1-\frac{x}{x'}\right)\right]^2 - \frac{1}{2}V_fE_f\varepsilon_{mu}^2\right\}dx$$

$$\Delta U_f = V_fE_f\varepsilon_{mu}^2\int_0^{x'}\left\{\left[1+a\left(1-\frac{x}{x'}\right)\right]^2 - 1\right\}dx$$

$$\Delta U_f = V_fE_f\varepsilon_{mu}^2\int_0^{x'}\left\{1+2a\left(1-\frac{x}{x'}\right) + a^2\left(1-2\frac{x}{x'}+\frac{x^2}{(x')^2}\right)-1\right\}dx$$

$$\Delta U_f = V_fE_f\varepsilon_{mu}^2\int_0^{x'}\left\{2a\left(1-\frac{x}{x'}\right) + a^2\left(1-2\frac{x}{x'}+\frac{x^2}{(x')^2}\right)\right\}dx$$

$$\Delta U_f = V_fE_f\varepsilon_{mu}^2\left\{2a\left(x' - \frac{1}{2}x'\right) + a^2\left(x' - x' + \frac{1}{3}x'\right)\right\}$$

$$\Delta U_f = V_fE_f\varepsilon_{mu}^2\left(ax' + \frac{1}{3}a^2x'\right)$$

$$\Delta U_f = V_fE_f\varepsilon_{mu}^2x'a\left(1+\frac{1}{3}a\right)$$

$$\Delta U_f = V_fE_f\varepsilon_{mu}^2\frac{V_m\sigma_{mu}R}{V_f2\tau}a\left(1+\frac{1}{3}a\right)$$

$$\Delta U_f = \frac{E_f E_m V_m}{2\tau} \varepsilon_{mu}^3 Ra\left(1+\frac{1}{3}a\right) \tag{B.14}$$

Next, the work done per unit area by the interfacial shear stress due to the relative displacement between the fibers and the matrix upon matrix cracking is calculated. The work done per unit area is the product of the interfacial shear stress due to friction, the relative displacement between the fiber and the matrix, Δv, and the total surface area over which the displacement occurs.

$$U_s = 2\frac{V_f}{\pi R^2}\int_0^{x'} \tau \Delta v (2\pi R) dx$$

$$U_s = 2\frac{V_f}{\pi R^2}\int_0^{x'} \tau \left[\left(-x\varepsilon_{mu} + \frac{x}{x'}\frac{x}{2}\varepsilon_{mu} + \frac{x'}{2}\varepsilon_{mu}\right) - \left(ax\varepsilon_{mu} - \frac{x}{x'}a\frac{x}{2}\varepsilon_{mu} - \frac{x'}{2}a\varepsilon_{mu}\right)\right](2\pi R)dx$$

$$U_s = \frac{4V_f\tau}{R}\varepsilon_{mu}\int_0^{x'}\left[-(1+a)x + (1+a)\frac{x^2}{2x'} + (1+a)\frac{x'}{2}\right]dx$$

$$U_s = \frac{4V_f\tau}{R}\varepsilon_{mu}\left[-\frac{1}{2}(1+a)(x')^2 + \frac{1}{3}(1+a)\frac{(x')^2}{2} + (1+a)\frac{(x')^2}{2}\right]$$

$$U_s = \frac{4V_f\tau}{R}\varepsilon_{mu}(1+a)(x')^2\left[-\frac{1}{2}+\frac{1}{6}+\frac{1}{2}\right]$$

$$U_s = \frac{2V_f\tau}{3R}\varepsilon_{mu}(1+a)(x')^2$$

$$U_s = \frac{2V_f\tau}{3R}\varepsilon_{mu}(1+a)\left(\frac{V_m\varepsilon_{mu}E_mR}{V_f 2\tau}\right)^2$$

$$U_s = \frac{V_m^2E_m^2}{6V_f\tau}\varepsilon_{mu}^3R(1+a)$$

$$U_s = \frac{V_m^2\,E_m^2\,E_f}{6\,V_f\,E_f\,\tau}\varepsilon_{mu}^3\,R(1+a)$$

$$U_s = \frac{V_mE_mE_f}{6\tau}\varepsilon_{mu}^3Ra(1+a) \qquad \text{(B.15)}$$

The energy per unit area of the composite required to form new crack faces within the matrix is:

$$G = 2V_m\gamma_m \qquad \text{(B.16)}$$

where γ_m is the energy per unit area required to form new crack faces within the matrix material.

Finally, the energy changes per unit area are summed. A frictional interfacial bond between the fibers and the matrix is assumed.

$$G + U_s + \Delta U_f + \Delta U_m = \Delta W \tag{B.17}$$

Equations B.12-16 are substituted into equation B.17.

$$2V_m\gamma_m + \frac{V_m E_m E_f}{6\tau}\varepsilon_{mu}^3 Ra(1+a) + \frac{V_m E_m E_f}{2\tau}\varepsilon_{mu}^3 Ra\left(1+\frac{1}{3}a\right) - \frac{V_m E_m E_f}{3\tau}\varepsilon_{mu}^3 Ra$$
$$= \frac{V_m E_m E_f}{2\tau}\varepsilon_{mu}^3 Ra(1+a)$$

Solving for the matrix ultimate strain, we obtain

$$\varepsilon_{mu} = \left[\frac{12\tau\gamma_m E_f V_f^2}{E_c E_m^2 V_m R}\right]^{\frac{1}{2}} \tag{B.18}$$

The composite stress where first matrix cracking occurs is

$$\sigma_y = E_c\left[\frac{12\tau\gamma_m E_f V_f^2}{E_c E_m^2 V_m R}\right]^{\frac{1}{3}}$$

$$\sigma_y = \left[\frac{12\tau\gamma_m E_c^2 E_f V_f^2}{E_m^2 V_m R}\right]^{\frac{1}{3}} \qquad \text{(B.19)}$$

APPENDIX C

TEST SPECIMEN POROSITY

The reaction bonding process produces specimens with a significant amount of porosity. It is important to know the amount of porosity to accurately determine the material's mechanical properties.

The technique described in ASTM standard C 20-74 (1974) was used to determine the volumes of open porosity and the impervious portions of the specimens. The impervious portion of the specimen consists of the ceramic material and the closed porosity. This ASTM standard was developed to determine the apparent porosity of burned refractory brick. The standard uses the Archimedean Principle which states that a solid body immersed in a liquid loses as much of its own weight as the weight of the liquid it has displaced. It is assumed that the buoyancy in air is negligible. The liquid used for the tests

was distilled water with a density of 1.0 g/cm^3. Following are the variables and definitions used with this ASTM standard:

W = dry weight, g where g is grams

W_b = suspended weight mass in water, g

W_s = saturated weight, g

v = total volume, including porosity, cm^3

v_{op} = volume of open porosity, cm^3

v_{ip} = volume of the impervious portion, cm^3

ρ_w = density of water, g/cm^3

As stated in the Density Determination Kit by Mettler Instruments AG (1981) according to the German Engineering Standard (DIN) 1305 the term 'weight' can be used instead of 'mass.' The Archimedean Principle results in the following equation:

$$W_b = W - \rho_w v_{ip} \qquad (C.1)$$

The volume of the impervious portion of the composite can be determined by rearranging equation C.1 resulting in the following equation:

$$v_{ip} = \frac{W - W_b}{\rho_w} \tag{C.3}$$

Next, the volume of the open porosity is determined by the weight gained by the specimen after immersion and removal from the liquid. The weight gain is due to the liquid infiltrating the open porosity of the solid. This is presented in equation C.4:

$$v_{op} = \frac{W_s - W}{\rho_w} \tag{C.4}$$

Finally, the total volume of the specimen is the sum of the volumes of the open porosity and the impervious portions of the solid specimen. The result is presented by equation C.5.

$$v = \frac{W_s - W_b}{\rho_w} \tag{C.5}$$

The total porosity content of a monolithic material can be determined by knowing the density of the material with no porosity. It is assumed that the weight of the gas in the pores of the material is negligible relative to the refractory material. As a result the total weight of the specimen is due to the refractory material only. Knowing the total volume, volume of open porosity,

the density of a fully dense refractory material and its dry weight the volume of the closed porosity can be determined. One has,

$$v_{cp} = v - v_{op} - W\frac{1}{\rho_m} \tag{C.6}$$

where: v_{cp} = volume of closed porosity, cm^3

ρ_m = density of matrix or refractory material, g/cm^3

Now the volume fraction of the porosity, V_p, can be determined from the following equation:

$$V_p = \frac{v_{cp} + v_{op}}{v} \tag{C.7}$$

Finding the porosity of a SiC/RBSN composite involves a few more variables due to the addition of fibers. In this composite system all the porosity is in the matrix. As with the monolithic material, the content of the pores is assumed to have a negligible weight. The total weight of the specimen is due to the matrix and the fibers. This is shown in the following equations where W is the weight, ρ is the density, V is the volume fraction, v is the volume, and the subscripts f and m refer to the fiber and the matrix, respectively:

$$W = W_f + W_m \tag{C.8}$$

$$W = \rho_f v_f + \rho_m v_m \tag{C.9}$$

$$W = \rho_f V_f v + \rho_m v_m \tag{C.10}$$

The matrix volume can be determined from equation C.10 above.

$$v_m = \frac{1}{\rho_m}(W - \rho_f V_f v) \tag{C.11}$$

The total volume is a sum of the volumes of the matrix, fibers, open porosity, and closed porosity. This is shown by the following equation:

$$v = v_{op} + v_{cp} + v_m + v_f \tag{C.12}$$

Next, equation C.11 is substituted into C.12 and the resulting equation is solved for the volume of closed porosity.

$$v = v_{op} + v_{cp} + v_m + V_f v \tag{C.13}$$

$$v_{cp} = (1 - V_f)v - v_{op} - v_m \tag{C.14}$$

$$v_{cp} = (1 - V_f)v - v_{op} - \frac{1}{\rho_m}(W - \rho_f V_f v) \tag{C.15}$$

Equation C.7 is used again to determine the volume fraction of the porosity within the composite. The porosity volume fraction with respect to the matrix, $V_{p,m}$, can be determined from the following equations:

$$V_{p,m} = \frac{v_p}{v_m + v_p} \tag{C.16}$$

$$V_{p,m} = \frac{V_p}{V_m + V_p} \tag{C.17}$$

The following section presents an example using the above equations. The density of a nonporous silicon nitride from the Materials Selector 1988 (1987) and the average density of a CVD type silicon carbide fiber from the American Ceramic Society (1991) are

$\rho_m = 3.2$ g/cm^3

$\rho_f = 3.0$ g/cm^3

First, the porosity in a monolithic RBSN specimen is determined. Using the procedures described in the ASTM standard the following weights are measured:

$W = 1.446$ g

$W_b = 0.973$ g

$W_s = 1.603$ g

The volumes are derived from the measured weights using equations C.3-5.

$$v_{ip} = \frac{W - W_b}{\rho_w} = \frac{1.446 - 0.973}{1.0} = 0.473 \text{ cm}^3$$

$$v_{op} = \frac{W_s - W}{\rho_w} = \frac{1.603 - 1.446}{1.0} = 0.157 \text{ cm}^3$$

$$v = \frac{W_s - W_b}{\rho_w} = \frac{1.603 - 0.973}{1.0} = 0.630 \text{ cm}^3$$

Using equation C.6 the volume of the closed porosity is calculated.

$$v_{cp} = v - v_{op} - W\frac{1}{\rho_m}v_{cp} = 0.630 - 0.157 - (1.446)\frac{1}{3.2} = 0.021\ cm^3$$

Finally, equation C.7 gives the volume fraction of the porosity of the RBSN specimen.

$$V_p = \frac{v_{cp} + v_{op}}{v} = \frac{0.021 + 0.157}{0.630} = 0.28$$

Next, the SiC/RBSN composite is analyzed. Equation C.15 is used to calculate the volume of the closed porosity of the composite specimen. The following weights were measured for a SiC/RBSN specimen:

$W = 0.965$ g

$W_b = 0.655$ g

$W_s = 1.036$ g

In addition, the fiber volume fraction, V_f, was determined using optical microscopy. A photograph of the composite cross-section was taken through the microscope. The fiber volume fraction was determined by manually measuring the fiber cross-sectional area within a measured area of the composite on the photograph. The result is

$V_f = 0.24$

The volumes are determined using equations C.3-5.

$$v_{ip} = \frac{W - W_b}{\rho_w} = \frac{0.965 - 0.655}{1.0} = 0.310\ cm^3$$

$$v_{op} = \frac{W_s - W}{\rho_w} = \frac{1.036 - 0.965}{1.0} = 0.071\ cm^3$$

$$v = \frac{W_s - W_b}{\rho_w} = \frac{1.036 - 0.655}{1.0} = 0.381\ cm^3$$

The volume of closed porosity is calculated using equation C.15.

$$v_{cp} = (1 - V_f)v - v_{op} - \frac{1}{\rho_m}(W - \rho_f V_f v)$$

$$= (1 - 0.24)0.381 - 0.071 - \frac{1}{3.2}[0.965 - (3.0)(0.24)(0.381)] = 0.003\ cm^3$$

Equation C.7 gives the volume fraction of the porosity of the SiC/RBSN specimen.

$$V_p = \frac{v_{cp} + v_{op}}{v} = \frac{0.003 + 0.071}{0.381} = 0.19$$

Finally, using equation C.17 the porosity volume fraction with respect to the matrix is determined.

$$V_{p,m} = \frac{V_p}{V_m + V_p} = \frac{0.19}{0.57 + 0.19} = 0.25$$

APPENDIX D

NUMERICAL EXAMPLES

This appendix contains numerical examples of the various theories used throughout this work. Selected topics are covered in the same order as in the Results and Discussion chapter. The first section will address the SiC/RBSN composite system which will be followed by the section on the enhanced SiC/SiC composite. All examples use data from room temperature tensile tests in air unless noted otherwise.

D.1 SiC/RBSN Composite System

This section addresses the SiC/RBSN composite system. Numerical examples are provided for predicting the Young's modulus, secondary modulus near the ultimate strength, first matrix cracking stress, and ultimate strength.

D.1.1 Tensile Modulus of SiC/RBSN

The Young's modulus of the SiC/RBSN composite system is determined first. The modulus is a function of the moduli of the constituents. The following variables are used:

E_{RBSN}=110 GPa, Young's modulus of monolithic RBSN

P=0.33, porosity of the monolithic RBSN

Using equation 6.42 to determine the modulus, E_o, of fully dense RBSN we have

$$E = E_o e^{-3P}$$

$$110 = E_o e^{-3(0.33)}$$

$$E_o = 296 \text{ GPa}$$

The porosity of the RBSN as the matrix in the SiC/RBSN composite is

P=0.32

Equation 6.42 is used again to determine the Young's modulus of the RBSN as the matrix in the SiC/RBSN composite.

$E_m=296e^{-3(0.32)}=112$ MPa

The SiC/RBSN composite modulus is determined using the rule of mixtures with the following variables:

$E_f=391$ GPa, Young's modulus of the fiber

$V_f=0.259$, fiber volume fraction

$V_m=0.741$, matrix volume fraction (includes porosity)

$E_c=V_fE_f + V_mE_m=(0.259)(391)+(0.741)(112)=183$ GPa

The calculated secondary modulus was determined using the rule of mixtures. Matrix effects were ignored. The calculation was as follows:

$E_{c2}=V_fE_f=(0.259)(391)=101$ GPa

D.1.2 Matrix Cracking and Interfacial Shear Properties for SiC/RBSN

This section presents examples for determining the first matrix cracking stress for the SiC/RBSN composite system. The following variables are used:

$R=70\ \mu$m, fiber radius

$x=2.0$ mm

$\beta=1.337$, constant

$\sigma_y=191$ MPa

Equation 6.44 is used to calculate the interfacial shear strength. The measured composite Young's modulus is used here.

$$\tau = \frac{\beta\, RV_m E_m \sigma_y}{2V_f E_c x} = \frac{(1.337)(70x10^{-6})(0.741)(112x10^{9})(191)}{2(0.259)(198x10^{9})(2x10^{-3})} = 7.2\ \text{MPa}$$

The theoretical maximum shear strength that allows cracks to propagate through the matrix without passing through the fibers is calculated from equation 6.45.

$$\tau_{cr} = \frac{(1 - V_f)E_m \sigma_{fu}}{\left\{2(1 + \nu_m)E_f\left[V_f E_f + (1 - V_f)E_m\right]\left[V_f - 1 - \ln(V_f)\right]\right\}^{\frac{1}{2}}}$$

$$\tau_{cr} = \frac{(1 - V_f)E_m \sigma_{fu}}{\left\{2(1 + \nu_m)E_f E_c\left[V_f - 1 - \ln(V_f)\right]\right\}^{\frac{1}{2}}}$$

$$\tau_{cr} = \frac{(1-0.259)(110x10^{9})(3.33x10^{9})}{\left\{2(1+0.22)(391x10^{9})(183x10^{9})\left[0.259-1-\ln(0.259)\right]\right\}^{\frac{1}{2}}}$$

τ_{cr} = 834 MPa

Next, we calculate the axial residual stress within the matrix of the composite due to the CTE mismatch between the fibers and the matrix.

T=22°C, test temperature

T_{proc}=1200°C, processing temperature

α_f=4.4x10^{-6} °C^{-1}, coefficient of thermal expansion of fiber

α_m=3.3x10^{-6} °C^{-1}, coefficient of thermal expansion of matrix

$\Delta T = T - T_{proc} = 22 - 1200 = -1178$°C

$$\varepsilon_T = (\alpha_f - \alpha_m)\Delta T = (4.4x10^{-6} - 3.3x10^{-6})(-1178) = -1.3x10^{-3}$$

$$\phi_1 = 1 - 0.5\left[\frac{1-2\nu}{1-\nu}\right]\left[1-\frac{E_c}{E_f}\right] = 1 - 0.5\left[\frac{1-2(0.22)}{1-0.22}\right]\left[1-\frac{183x10^9}{391x10^9}\right] = 0.809$$

$$\phi_2 = 0.5\left[1+\frac{E_c}{E_f}\right] = 0.5\left[1+\frac{183x10^9}{391x10^9}\right] = 0.734$$

$$\sigma_{m\alpha} = \left[E_m\frac{\phi_2}{\phi_1}\right]\left[\frac{E_f}{E_c}\right]\left[\frac{V_f}{1-\nu_m}\right]\varepsilon_T = \left[(110x10^9)\frac{0.734}{0.809}\right]\left[\frac{391x10^9}{183x10^9}\right]\left[\frac{0.259}{1-(0.22)}\right](-1.3x10^{-3})$$

$\sigma_{m\alpha}$ = -92x10^6 Pa = -92 MPa (matrix is in residual compression)

The ACK theory, equation 6.51, is used to predict the first matrix cracking stress. Using the appropriate material parameters, the equation below shows the calculations.

γ_m=36 J/m^2, matrix fracture surface energy

$$\sigma_y = \left[\frac{12\tau\gamma_m E_c^2 E_f V_f^2}{E_m^2 V_m R}\right]^{\frac{1}{3}} = \left[\frac{12(7.1x10^6)(36)(183x10^9)^2(391x10^9)(0.259)^2}{(110x10^9)^2(0.741)(70x10^{-6})}\right]^{\frac{1}{3}}$$

σ_y=162x10^6 Pa = 162 MPa

The ACK theory is used here with a weakly bonded fiber/matrix interface. Another equation, attributed to Aveston, Cooper, and Kelly, can also be used to calculate the first matrix cracking stress. The fiber/matrix interfacial debonding energy is assumed to equal the matrix fracture energy in this model. Consequently,

$G_{II}=\gamma_m$=36 J/m^2

Equation 6.52 is

$$\varepsilon_{mu}^3 - \frac{12\gamma_m E_f V_f^2}{E_m V_m E_c R}\varepsilon_{mu} - \frac{12\gamma_m \tau E_f V_f^2}{E_m^2 V_m E_c R} = 0$$

$$\varepsilon_{mu}^3 - \frac{12(36)(391x10^9)(0.259)^2}{(110x10^9)(0.741)(183x10^9)(70x10^{-6})}\varepsilon_{mu} - \frac{12(36)(7.1x10^6)(391x10^9)(0.259)^2}{(110x10^9)^2(0.741)(183x10^9)(70x10^{-6})} = 0$$

$$\varepsilon_{mu}^3 - (1.082x10^{-5})\varepsilon_{mu} - (6.982x10^{-10}) = 0$$

The polynomial equation is solved numerically using the secant method. Following are the starting estimates, ε_o, the roots of the polynomial, ε_{mu}, and the resulting stress from Hooke's law.

ε_o=-1000, ε_{mu}=-3.26x10^{-3},

$\sigma_y=\varepsilon_{mu}E_c$=(-3.26x10^{-3})(183x10^9)=-596x10^6 Pa=-596 MPa

ε_o=0, ε_{mu}=-6.45x10^{-5}

$\sigma_y=\varepsilon_{mu}E_c$=(-6.45x10^{-5})(183x10^9)=-12x10^6 Pa=-12 MPa

ε_o=1000, ε_{mu}=3.32x10^{-3}

$\sigma_y=\varepsilon_{mu}E_c$=(3.32x10^{-3})(183x10^9)=608x10^6 Pa=608 MPa

The first matrix cracking stress is 608 MPa and the corresponding strain is 3.32x10^{-3} mm/mm.

Equation 6.54 accounts for the residual stresses due to the different coefficients of thermal expansion of the constituents. The correction is applied to the ACK theory in the following example.

$$\sigma_{y\alpha} = \sigma_y - \sigma_{m\alpha}\frac{E_c}{E_m}$$

$$\sigma_{y\alpha} = (162) - (-92)\frac{183}{110}$$

$\sigma_{y\alpha}$=315 MPa

D.1.3 CVD SiC Fiber Properties

The estimate for the Weibull modulus is determined first by using equation 6.62 from the maximum likelihood method. A closed-form solution for m is not possible. As a result, the equation is solved numerically. Strength data for the treated fibers tested 600°C (1110°F) in air will be used here. From Table XXII the ultimate strengths are

σ_1 = 3.46 GPa

σ_2 = 3.40 GPa

σ_3 = 3.22 GPa

σ_4 = 2.82 GPa

σ_5 = 2.76 GPa

$$\frac{\sum_{n=1}^{n_{tot}} \sigma_n^m \ln(\sigma_n)}{\sum_{n=1}^{n_{tot}} \sigma_n^m} - \frac{1}{n_{tot}} \sum_{n=1}^{n_{tot}} \ln(\sigma_n) - \frac{1}{m} = 0$$

Solving for the Weibull modulus we have, m=13.3. From the ASTM standard designation C 1239 we have the unbiasing factor of 0.7 for five specimens.

Multiplying the estimated Weibull modulus by the unbiasing factor gives us an unbiased estimate of the Weibull modulus.

$m=(13.3)(0.7)=9.3$

Next, equation 6.63 is used to determine the characteristic strength.

$$\sigma_\theta = \left[\left(\sum_{n=1}^{n_{tot}} \sigma_n^m\right)\frac{1}{n_{tot}}\right]^{\frac{1}{m}}$$

$\sigma_\theta=3.24$ GPa

The composite mean stress at the initiation of the secondary modulus at 600°C is 300 MPa. The average stress in the fibers is determined by using the rule of mixtures.

$$\sigma_f = \frac{\sigma_c}{V_f} = \frac{300}{0.259} = 1160 \text{ MPa} = 1.16 \text{ GPa}$$

The probability of failure for the fibers at $\sigma_f=1.16$ GPa is determined by using the two-parameter Weibull cumulative distribution function, equation 6.59.

$$P_f = 1 - e^{-\left(\frac{\sigma}{\sigma_\theta}\right)^m}$$

$$P_f = 1 - e^{-\left(\frac{1.16}{3.24}\right)^{9.3}}$$

$P_f = 7.9\text{x}10^{-5}$

D.1.4 Ultimate Tensile Strength of SiC/RBSN

The first example for determining the ultimate strength of the SiC/RBSN composite uses the rule of mixtures, equation 6.65. The mean treated fiber ultimate strength is σ_{fu}=3.33 GPa.

$\sigma_{cu}=V_f\sigma_{fu}=(0.259)(3.33x10^3)=862$ MPa

The following example uses Curtin's theory (1993) which uses the mean fiber ultimate strength, σ_{fu}=3.33 GPa, and the fiber Weibull modulus, m=8.6. The fiber gage length is, L_f=25 mm.

$$\sigma_{cu} = V_f\left(\frac{2}{m+2}\right)^{\frac{1}{m+1}}\left(\frac{m+1}{m+2}\right)\left[\frac{\sigma_{fu}^m \tau L_f}{R\ln(2)}\right]^{\frac{1}{m+1}}$$

$$\sigma_{cu} = (0.259)\left(\frac{2}{8.6+2}\right)^{\frac{1}{8.6+1}}\left(\frac{8.6+1}{8.6+2}\right)\left[\frac{(3.33x10^9)^{8.6}(7.1x10^6)(25x10^{-3})}{(70x10^{-6})\ln(2)}\right]^{\frac{1}{8.6+1}}$$

$\sigma_{cu}=663x10^6$ Pa=663 MPa

The next example uses theory based on a "dry" fiber bundle, equation 6.67. The composite gage length which is assumed to be the fiber bundle gage length, L_c, is 38 mm and the fiber gage length, L_f is 25 mm.

$$\sigma_{cub} = V_f\sigma_{fu}\left(\frac{L_f}{L_c}\right)^{\frac{1}{m}} e^{-\frac{1}{m}}$$

$$\sigma_{cub} = (0.259)(3.33x10^3)\left(\frac{25}{38}\right)^{\frac{1}{8.6}} e^{-\frac{1}{8.6}}$$

σ_{cub}=735 MPa

The example for the modified fiber bundle failure analysis of Evans (1989) is presented next. First, the scale parameter, σ_o, is determined using equation 6.70.

$$\sigma_o = \frac{\sigma_{fu}}{\Gamma\left(1+\frac{1}{m}\right)}(2\pi RL_f)^{\frac{1}{m}}$$

$$\sigma_o = \frac{3.33}{\Gamma\left(1+\frac{1}{8.6}\right)}\left[2\pi\left(70x10^{-6}\right)\left(25x10^{-3}\right)\right]^{\frac{1}{8.6}}$$

$$\sigma_o = \frac{3.33x10^3}{0.945}\left[2\pi\left(70x10^{-6}\right)\left(25x10^{-3}\right)\right]^{\frac{1}{8.6}}$$

σ_o=934 MPa$\cdot$ m$^{\frac{2}{8.6}}$

The next step is to determine the fiber bundle strength, σ_{fub}, from equation 6.69 by numerical iteration. The area normalizing factor, A_o, is 1.0 m^2.

$$\left(\frac{R\sigma_{fub}}{\tau x}\right)^{m+1} = \frac{A_o}{2\pi RL_c}\left(\frac{R\sigma_o}{\tau x}\right)^m\left[1-\left(1-\frac{\tau x}{R\sigma_{fub}}\right)^m\right]^{-1}$$

$$\left[\frac{(70x10^{-6})\sigma_{fub}}{(7.1x10^6)(0.002)}\right]^{8.6+1} = \frac{1.0}{2\pi(70x10^{-6})(0.038)}\left[\frac{(70x10^{-6})(934)}{(7.1)(0.002)}\right]^{8.6}\left\{1-\left[1-\frac{(7.1)(0.002)}{(70x10^{-6})\sigma_{fub}}\right]^{8.6}\right\}^{-1}$$

The number of iterations is set to 20 and the initial estimate for σ_{fub} is set to 1. The result is

σ_{fub}=2.69x10^9 Pa=2.69 GPa

Lastly, the ultimate strength of the SiC/RBSN composite is calculated using equation 6.68.

$$\sigma_{cubm} = V_f \sigma_{fub} e^{-\frac{1-\left(1-\frac{\tau x}{R\sigma_{fub}}\right)^{m+1}}{(m+1)\left[1-\left(1-\frac{\tau x}{R\sigma_{fub}}\right)^{m}\right]}}$$

$$\sigma_{cubm} = (0.259)(2.71x10^{9}) e^{-\frac{1-\left[1-\frac{(7.1x10^{6})(0.002)}{(70x10^{-6})(2.71x10^{9})}\right]^{8.9+1}}{(8.9+1)\left[1-\left(1-\frac{(7.1x10^{6})(0.002)}{(70x10^{-6})(2.71x10^{9})}\right)^{8.9}\right]}}$$

σ_{cubm}=630x10^6 Pa=630 MPa

Cao's and Thouless' (1990) theory is presented next. The variable Σ is defined by equation 6.73 as

$$\Sigma = \left[\frac{A_o \sigma_o^m \tau (m+1)}{2\pi R^2}\right]^{\frac{1}{m+1}}$$

$$\Sigma = \left[\frac{(1.0)(975x10^{6})^{8.9}(7.1x10^{6})(8.9+1)}{2\pi(70x10^{-6})^{2}}\right]^{\frac{1}{8.9+1}} = 4.29x10^{9} \text{ Pa}$$

The theoretical ultimate strength of the SiC/RBSN composite is

$$\sigma_{cu} = V_f \Sigma \left(\frac{\Sigma R}{m(m+1)\tau L_c}\right)^{\frac{1}{m}} e^{-\frac{1}{m}}$$

$$\sigma_{cu} = (0.259)(4.29x10^{9})\left[\frac{(4.29x10^{9})(70x10^{-6})}{(8.9)(8.9+1)(7.1x10^{6})(0.038)}\right]^{\frac{1}{8.9}} e^{-\frac{1}{8.9}} = 608x10^{6} \text{ Pa}$$

σ_{cu}=608 MPa

D.2 Enhanced SiC/SiC Composite System

This section covers the enhanced SiC/SiC composite system. Numerical examples are presented which calculate the Young's modulus. The ultimate strength analysis is the same as the one used for the SiC/RBSN. As a result, no examples are provided for the ultimate strength calculations.

The first example is an analysis using the model with straight fibers. The longitudinal modulus is determined using the rule of mixtures as shown with the SiC/RBSN composite. The room temperature constituent properties are

$E_{fT}=E_{fL}=190$ GPa, fiber transverse and longitudinal moduli

$E_{mT}=E_{mL}=243$ GPa, matrix transverse and longitudinal moduli

The longitudinal modulus of the 60° ply by the rule of mixtures at room temperature is

$E_{cL}=228$ GPa

The transverse modulus of the 60° ply is determined using equation 6.18. A strong interfacial fiber/matrix bond is assumed. First, the variable η, is calculated.

$$\eta = \frac{\frac{E_{fT}}{E_{mT}} - 1}{\frac{E_{fT}}{E_{mT}} + \xi} = \frac{\frac{190}{243} - 1}{\frac{190}{243} + 2} = -0.0784$$

The transverse modulus is

$$E_{cT} = E_{mT}\left[\frac{1+\xi\eta V_f}{1-\eta V_f}\right] = (243)\left[\frac{1+(2)(-0.0784)(0.2875)}{1-(-0.0784)(0.2875)}\right] = 227 \text{ GPa}$$

The shear modulus of the 60° ply is calculated from the constituent properties. The Poisson's ratios of the fiber, ν_f, and the matrix, ν_m, are 0.2. The shear modulus is calculated for each of the constituent using equation 6.20 as follows

$$G_f = \frac{E_f}{2(1+\nu)} = \frac{190}{2(1+0.2)} = 79.2 \text{ GPa}$$

$G_m = 101$ GPa

The shear modulus of the 60° ply is calculated using equation 6.21. First, the variable η, is calculated as follows

$$\eta = \frac{\frac{G_f}{G_m}-1}{\frac{G_f}{G_m}+\xi} = \frac{\frac{79.2}{101}-1}{\frac{79.2}{101}+2} = -0.0777$$

The shear modulus of the 60° ply with a strong fiber/matrix interface is

$$G_{LT} = G_m\left[\frac{1+\xi\eta V_f}{1-\eta V_f}\right] = (101)\left[\frac{1+(2)(-0.0777)(0.2875)}{1-(-0.0777)(0.2875)}\right] = 94 \text{ GPa}$$

The stiffness provided by the 60° ply in the longitudinal direction of the specimen is determined using equation 6.23.

$$E_x = \left[\frac{\cos^4\theta}{E_L}+\frac{\sin^4\theta}{E_T}+\frac{1}{4}\left(\frac{1}{G_{LT}}-\frac{2\nu_{LT}}{E_L}\right)\sin^2 2\theta\right]^{-1}$$

$$E_x = \left\{\frac{\cos^4 60°}{228}+\frac{\sin^4 60°}{227}+\frac{1}{4}\left[\frac{1}{94}-\frac{2(0.2)}{228}\right]\sin^2 2(60°)\right\}^{-1}$$

$E_x = 226$ GPa

The moduli of the -60° plies are the same as the 60° plies. The resulting modulus in the longitudinal direction of the specimen is the same also. That is,

$E_{x60°}=E_{x-60°}=226$ GPa

The longitudinal modulus of the 0° ply is

$E_{x0°}=198$ GPa

Equation 6.25 is used to calculate the resultant laminated composite stiffness.

$$E_{cL} = \frac{n_{0°}}{n_{tot}}E_{x0°} + \frac{n_{60°}}{n_{tot}}E_{x60°}$$

$$E_{cL} = \frac{1}{5}(198) + \frac{4}{5}(226) = 221 \text{ GPa}$$

The next example accounts for the fiber undulations in the enhanced SiC/SiC composite. The equations for determining the longitudinal modulus in the 0° ply are illustrated here. In addition, a strong fiber/matrix interface is assumed to exist. First, equation 6.26 is substituted into equation 6.29.

$$\phi_1 = \tan^{-1}\left[\frac{dZ(x_1)}{dx_1}\right] = \tan^{-1}\left[\frac{H\pi}{2L_1}\cos\left(\frac{\pi x_1}{L_1}\right)\right]$$

The variables used are

$E_L=198$ GPa

$E_T=197$ GPa

$G_{LT}=82$ GPa

$H=610\,\mu$m

$L_1=0.785$ mm

ν_{LT}=0.20

The properties are at room temperature. Substituting the variables into the equation above we get

$$\phi_1 = \tan^{-1}\left[\frac{(610\text{x}10^{-6})\pi}{2(785\text{x}10^{-6})}\cos\left(\frac{\pi x_1}{785\text{x}10^{-3}}\right)\right] = \tan^{-1}[1.22\cos(4.00x)]$$

Equation 6.30 is substituted into equation 6.34 which is substituted into equation 6.36 to determine the mean strain in the ply. Finally, the equation for the mean strain is substituted into equation 6.38 to determine the mean longitudinal modulus of the 0° ply. The resulting equation is

$$E_L = \left\{\frac{1}{2L_1}\int_0^{2L_1}\left[\frac{\cos^4\phi}{E_L}+\left(\frac{1}{G_{LT}}-\frac{2\nu_{LT}}{E_L}\right)\sin^2\phi\cos^2\phi+\frac{\sin^4\phi}{E_T}\right]dx\right\}^{-1}$$

$$E_L = \left\{\frac{1}{2(0.785)}\int_0^{2(0.785)}\left[\frac{\cos^4\phi}{198}+\left(\frac{1}{82}-\frac{2(0.20)}{198}\right)\sin^2\phi\cos^2\phi+\frac{\sin^4\phi}{197}\right]dx\right\}^{-1}$$

$$E_L = \left\{\frac{1}{1.57}\int_0^{1.57}\left[\frac{\cos^4\phi}{198}+(10.15\text{x}10^{-3})\sin^2\phi\cos^2\phi+\frac{\sin^4\phi}{197}\right]dx\right\}^{-1}$$

Solving the above equation numerically, we get

E_L = 198 GPa

REPORT DOCUMENTATION PAGE

Form Approved
OMB No. 0704-0188

1. AGENCY USE ONLY (*Leave blank*)	2. REPORT DATE	3. REPORT TYPE AND DATES COVERED
	April 1998	Final Contractor Report

4. TITLE AND SUBTITLE

High Temperature Mechanical Characterization of Ceramic Matrix Composites

5. FUNDING NUMBERS

WU–523–21–13–00
NCC3–367

6. AUTHOR(S)

John Z. Gyekenyesi

7. PERFORMING ORGANIZATION NAME(S) AND ADDRESS(ES)

Cleveland State University
1983 E. 24th Street
Cleveland, Ohio 44115–2403

8. PERFORMING ORGANIZATION REPORT NUMBER

E–11147

9. SPONSORING/MONITORING AGENCY NAME(S) AND ADDRESS(ES)

National Aeronautics and Space Administration
Lewis Research Center
Cleveland, Ohio 44135–3191

10. SPONSORING/MONITORING AGENCY REPORT NUMBER

NASA CR—1998-206611

11. SUPPLEMENTARY NOTES

Project Manager, R. Bhatt, Materials Division, NASA Lewis Research Center, organization code 5130, (216) 433–5513.

12a. DISTRIBUTION/AVAILABILITY STATEMENT

Unclassified - Unlimited
Subject Category: 39 Distribution: Nonstandard

This publication is available from the NASA Center for AeroSpace Information, (301) 621–0390.

12b. DISTRIBUTION CODE

13. ABSTRACT (***Maximum 200 words***)

A high temperature mechanical characterization laboratory has been assembled at NASA Lewis Research Center. One contribution of this work is to test ceramic matrix composite specimens in tension in environmental extremes. Two high temperature tensile testing systems were assembled. The systems were assembled based on the performance and experience of other laboratories and meeting projected service conditions for the materials in question. The systems use frames with an electric actuator and a center screw. A PC based data acquisition and analysis system is used to collect and analyze the data. Mechanical extensometers are used to measure specimen strain. Thermocouples, placed near the specimen, are used to measure the specimen gage section temperature. The system for testing in air has a resistance element furnace with molybdenum disilicide elements and pneumatic grips with water cooling attached to hydraulic alignment devices. The system for testing in an inert gas has a graphite resistance element furnace in a chamber with rigidly mounted, water cooled, hydraulically actuated grips. Unidirectional SiC fiber reinforced reaction bonded Si_3N_4 and triaxially woven, two dimensional, SiC fiber reinforced enhanced SiC composites were tested in unidirectional tension. Theories for predicting the Young's modulus, modulus near the ultimate strength, first matrix cracking stress, and ultimate strength were applied and evaluated for suitability in predicting the mechanical behavior of SiC/RBSN and enhanced SiC/SiC composites. The SiC/RBSN composite exhibited pseudo tough behavior (increased area under the stress/strain curve) from 22° to 1500°C. The rule of mixtures provides a good estimate of the Young's modulus of the SiC/RBSN composite using the constituent properties from room temperature to 1440°C for short term static tensile tests in air or nitrogen. The rule of mixtures significantly overestimates the secondary modulus near the ultimate strength. The ACK theory provides the best approximation of the first matrix cracking stress when residual stresses are ignored. The theory of Cao and Thouless, based on Weibull statistics, gave the best prediction for the composite ultimate strength. The enhanced SiC/SiC composite exhibited nonlinear stress/strain behavior from 24° to 1370°C in air with increased ultimate strain when compared to monolithic SiC. The theory of Yang and Chou with the assumption of a frictional fiber/matrix interface provided the best estimate of the Young's modulus. The theory of Cao and Thouless gave the best estimate for the ultimate strength.

14. SUBJECT TERMS	15. NUMBER OF PAGES
CMCs; Ceramic composite; Tensile testing; High temperatures; SiC/RBSN; SiC/SiC	287
	16. PRICE CODE A13

17. SECURITY CLASSIFICATION OF REPORT	18. SECURITY CLASSIFICATION OF THIS PAGE	19. SECURITY CLASSIFICATION OF ABSTRACT	20. LIMITATION OF ABSTRACT
Unclassified	Unclassified	Unclassified	